Springer Theses
Recognizing Outstanding Ph.D. Research

Yuting Yang

Evapotranspiration Over Heterogeneous Vegetated Surfaces

Models and Applications

Springer

Springer Theses

Recognizing Outstanding Ph.D. Research

Aims and Scope

The series "Springer Theses" brings together a selection of the very best Ph.D. theses from around the world and across the physical sciences. Nominated and endorsed by two recognized specialists, each published volume has been selected for its scientific excellence and the high impact of its contents for the pertinent field of research. For greater accessibility to non-specialists, the published versions include an extended introduction, as well as a foreword by the student's supervisor explaining the special relevance of the work for the field. As a whole, the series will provide a valuable resource both for newcomers to the research fields described, and for other scientists seeking detailed background information on special questions. Finally, it provides an accredited documentation of the valuable contributions made by today's younger generation of scientists.

Theses are accepted into the series by invited nomination only and must fulfill all of the following criteria

- They must be written in good English.
- The topic should fall within the confines of Chemistry, Physics, Earth Sciences, Engineering and related interdisciplinary fields such as Materials, Nanoscience, Chemical Engineering, Complex Systems and Biophysics.
- The work reported in the thesis must represent a significant scientific advance.
- If the thesis includes previously published material, permission to reproduce this must be gained from the respective copyright holder.
- They must have been examined and passed during the 12 months prior to nomination.
- Each thesis should include a foreword by the supervisor outlining the significance of its content.
- The theses should have a clearly defined structure including an introduction accessible to scientists not expert in that particular field.

More information about this series at http://www.springer.com/series/8790

Yuting Yang

Evapotranspiration Over Heterogeneous Vegetated Surfaces

Models and Applications

Doctoral Thesis accepted by
Tsinghua University, Beijing, China

Springer

Author
Dr. Yuting Yang
CSIRO Land and Water
Canberra, ACT
Australia

Supervisor
Assoc. Prof. Songhao Shang
Tsinghua University
Beijing
China

ISSN 2190-5053 ISSN 2190-5061 (electronic)
Springer Theses
ISBN 978-3-662-46172-3 ISBN 978-3-662-46173-0 (eBook)
DOI 10.1007/978-3-662-46173-0

Library of Congress Control Number: 2015930005

Springer Heidelberg New York Dordrecht London

Printed on acid-free paper

Springer-Verlag GmbH Berlin Heidelberg is part of Springer Science+Business Media (www.springer.com)

Parts of this dissertation have been published in the following journal articles:

1. Yuting Yang, Di Long, Songhao Shang, 2013. Remote estimation of terrestrial evapotranspiration without using meteorological data. *Geophysical Research Letters*, 40, 3026–3030.
2. Hanyu Lu, Tingxi Liu, Yuting Yang, Dandan Yao, 2014. A hybrid dual-source model of estimating evapotranspiration over different ecosystems and implications for satellite-based approaches. *Remote Sensing*, 6, 8359–8386.
3. Yuting Yang, Songhao Shang, 2013. A hybrid dual source scheme and trapezoid framework based evapotranspiration model (HTEM) using satellite images: algorithm and model test. *Journal of Geophysical Research: Atmosphere,* 118, 2284–2300.
4. Yuting Yang, Huade Guan, John Hutson, Hailong Wang, CaeciliaEwenz, Songhao Shang and Craig Simmons, 2013. Examination and parameterization of the root water uptake model from stem water potential and sap flow measurements. *Hydrological Processes*, 27(20), 2857–2863.
5. Yuting Yang, Songhao shang and Lei Jiang, 2012. Remote Sensing temporal and spatial patterns of evapotranspiration and the responses to water management in a large irrigation district of North China. *Agricultural and Forest Meteorology*, 164, 112–122.
6. Yuting Yang, Songhao Shang and Huade Guan, 2012. Development of a soil-plant-atmosphere continuum model (HDS-SPAC) based on hybrid dual-source approach and its verification in wheat land. *Science China Series E: Technological Sciences*. 55(10), 2671–2685.
7. Yuting Yang, Songhao Shang, 2012. Comparison of three dual-source evapotranspiration models in partitioning potential evaporation and potential transpiration. *Transactions of the CSAE*, 28(24), 85–91 (In Chinese with English abstract).

To my father, Fujiang Yang, my mother, Xiaoling Yang and my wife, Jiayi Li

Supervisor's Foreword

The thesis of Mr. Yuting Yang breaks new ground in the modeling of evapotranspiration over heterogeneous vegetated surfaces at both field and regional scales. At the field scale, a hybrid dual source evapotranspiration model is proposed to estimate actual evaporation and transpiration processes, and verified with field observations over different land covers (Chap. 3). Then a soil-plant-atmosphere continuum model (HDS-SPAC) is proposed and tested in a farmland ecosystem and a natural forest, which couples the hybrid dual source scheme for evapotranspiration and soil water and heat transfer models (Chap. 4). At the regional scale, a hybrid dual source scheme and trapezoid framework-based evapotranspiration model (HTEM) using remote sensing data is proposed, and validated with ground observations in China and US (Chap. 5). Then HTEM fed with Moderate Resolution Imaging Spectroradiometer (MODIS) data is applied in Hetao Irrigation District in North China to examine the spatial and temporal patterns of evapotranspiration in the region, and to analyze the impacts of water-saving on evapotranspiration of crops and natural vegetation (Chap. 7). Besides, a novel evapotranspiration model based solely on remote sensing data is proposed to estimate evapotranspiration by exploiting the linkage between water and carbon cycles, which is especially applicable to areas with less ground observations (Chap. 6). These works have been published in Journal of Geophysical Research (2013), Geophysical Research Letters (2013), and Agricultural and Forest Meteorology (2012), etc.

Overall, the thesis contains novel contributions to evapotranspiration modeling and applications. This thesis highlights the applicability of the hybrid dual source evapotranspiration model in modeling evapotranspiration and partitioning evaporation and transpiration at different spatial scales, and the possibility of estimating regional evapotranspiration without meteorological data. The quality of the thesis is a proof to Mr. Yang's high modeling ability and also deep understanding of the evapotranspiration and related processes.

Qinghuayuan, Beijing, November 2014 Assoc. Prof. Songhao Shang

Abstract

Land surface evapotranspiration (ET) is a key component of the water and energy balance over terrestrial ecosystems, quantification of which has long been an important topic in hydrological, meteorological, agricultural, and ecological studies. The primary objective of this dissertation is to estimate land surface evapotranspiration (ET), with special attention paid to the heterogeneous vegetated surfaces. Different algorithms with varying temporal and spatial resolutions are developed to estimate ET using different data inputs. Besides, a novel approach to estimate ET from remote sensing by exploiting the linkage between water and carbon cycles is proposed. Finally, the potential of using remote sensing ET model in the real management of water resources in a large irrigation district is discussed.

First, this dissertation provides a detailed comparison among three dual source ET models in estimating potential ET and partitioning potential evaporation and potential transpiration under different hypothetical vegetation distribution conditions. Then, a hybrid dual source ET model (H-D model) is proposed to estimate actual ET processes, and verified with field observations over four different ecosystems. The performances of the H-D model are further compared with those from three other ET models. Results indicate that the H-D model is capable of estimating ET over a wide range of vegetated surfaces and could provide better evaporation (E) and transpiration (T) partition results.

By coupling the hybrid dual source scheme with a soil water and heat simulation model, a soil-plant-atmosphere continuum model (HDS-SPAC) is proposed and tested in a farmland ecosystem and a natural forest, respectively. For model application in the natural forest, a simple field experiment is designed to examine and parameterize the root water uptake models. Moreover, the traditional root water uptake model has been improved based on field data.

In order to capture ET information over larger geographic extents, a hybrid dual source scheme and trapezoid framework-based ET model (HTEM) using remote sensing images is proposed. Data from three validation sites located respectively in Iowa and Arizona of USA and Weishan irrigation district of China are used to test the model. Results show that the HTEM could provide good estimates of ET over

different vegetation coverage conditions, with the root mean square errors ranging from 30 to 50 W m^{-2}. Besides, it is found that HTEM is able to give accurate E and T partitioning. Furthermore, HTEM fed with Moderate Resolution Imaging Spectroradiometer (MODIS) data is applied in Hetao Irrigation District from 2000 to 2010 to examine the spatial and temporal patterns of ET in the region. Results indicate that during the study period, a reduction in river water diversion for irrigation has not reduced the agricultural land ET, suggesting no significant impact on agricultural production. But ET over the non-irrigated grassland is found to be the largest contribution of water-saving.

To further explore new method of ET estimation over vegetated surfaces, a novel approach based solely on remote sensing data is proposed to estimate ET by exploiting the linkage between water and carbon cycles. The method is validated with eddy covariance measurements from 20 sites within the Ameriflux network and compared with MODIS ET product. Results show the new method could provide accurate and better ET estimates than MODIS ET. This suggests that routine estimation of ET from satellite remote sensing without using fine-resolution meteorological field is possible and can be very useful for studying the coupled water and carbon cycles.

Keywords Land surface evapotranspiration · Vegetation distribution characteristic · Remote sensing · Hybrid dual source scheme · Carbon-water relations

Acknowledgments

I have been receiving assistances from many people and agencies during my 5-year study toward the Ph.D. degree. Without their various kinds of help and guidance, this Ph.D. dissertation would not have been possible.

First of all, I would like to extend my gratitude to my academic advisor, Professor Songhao Shang, who provided my opportunity to come to Tsinghua University and guidance, support, and encouragement in my research during years at Tsinghua. He is always offering constructive and timely suggestions to my work, and giving me ample space and freedom to conduct my own research. Being a student of Prof. Shang would be one of the luckiness in my lifetime.

I would also like to thank Dr. Huade Guan, Dr. John Hutson, Dr. Craig Simmons and Dr. Caecilia Ewenz, who have provided me with insightful supervision during my visiting study at Flinders University. Special gratitude goes to Dr. Huade Guan, who has been such a generous and supportive mentor of mine. The inspirations from him and discussions with him have led to Chaps. 2 and 3. Moreover, Dr. Guan also involved in experimental study on root water uptake in Chap. 4. Meanwhile, I thank the Chinese Scholarship Council for supporting my visiting at Flinders University.

I am also deeply grateful for all other professors in my committee and in the hydrology research institute. Special thanks go to Prof. Dawen Yang and Dr. Huimin Lei, who provided flux data of the Weishan site (Chap. 5) and numerous useful suggestions on my research.

My special gratitude for my parents, Fujiang Yang and Xiaoling Yang, and wife, Jiayi Li. Thank you for your love, support, and patience at all time.

Acknowledgements are extended to my folks in the institute for their suggestions, questions, and help, and most importantly, for just being there with me during all those years.

This dissertation study was supported by the National Science Foundation (51279077, 50939004 and 50879041) and the National Key Technology R&D Program (2011BAD25B05-3).

Contents

Figures

Tables

Chapter 1
Introduction

1.1 Research Background and Significance

Water servers as a fundamental component for almost all living creatures and plays a critical role in building a sustainable natural and social environment. However, with the increase of world population and degradation in water quality, there has been a significant decline in the availability of safe water resource across the globe. Studies have shown that nearly 1/3 of the world population lives in the area with per capital water resource lower than the minimum standard and there are more than 240 million people living in places with high water scarcity (e.g., Oki and Kanae 2006). In addition, intensified climate change and human activities have brought further threatens to limited water resources, making water crisis in water limited regions even worse. World Meteorology Organization pointed out in 1996 that water scarcity is the largest issue for global major cities. By the year of 2050, more than 2/3 of world population will be living in cities, in which 46 % of them will be facing serious water shortage problem. To that end, promoting sustainable water management and improving water use efficiency have become one of the most critical challenges that our society are facing.

Different from other natural resources, water is unique in its flowing nature. Thus, evaluation of water resources should focus more on its flowing characteristic rather than only on the amount of water storage. Water in the atmosphere reaches land surface via precipitation, in which part of them become runoff and flow into river bodies (e.g., river and lake) and another part return into the atmosphere through evapotranspiration (ET). All these processes constitute the terrestrial hydrological cycle. Among different processes within the terrestrial hydrological cycle, land surface ET plays an important role in determining the global water balance and linking the global water and energy cycles. On one hand, it moves a vast amount of water vapour upwards into the atmosphere to support land surface precipitation. One the other hand, it controls land-atmosphere feedbacks via modulating the surface energy budget (Rosen 1999). From a water balance's perspective, land surface

Y. Yang, *Evapotranspiration Over Heterogeneous Vegetated Surfaces*,
Springer Theses, DOI 10.1007/978-3-662-46173-0_1

ET is the second largest water flux (after precipitation) within the terrestrial hydrological cycle, which accounts for about 65 % of land surface rainfall. This ratio can be as high as more than 90 % in arid regions (Bonan 2002). In the northern part of China, agricultural water use accounts for about 70 % of total water consumption in the area, with more than 90 % of them consumed via ET (Liu et al. 2002). This highlights the water resource crisis in the area, where owns 65 % agricultural land but only 20 % water resources of the national totals (Deng et al. 2006).

Land surface ET consists of two main components, i.e., evaporation and transpiration. Evaporation (E) accounts for the movement of water to the air from sources such as the soil, canopy interception, and water bodies. Transpiration accounts for the movement of water within a plant and the subsequent loss of water as vapour through stomata in its leaves. Due to its importance in determining the water and energy budgets over the land surface, the study of ET has long been an active research topic in areas such as hydrology, ecology, agriculture and meteorology, which has led to the development of many ET models or algorithms. However, mechanisms that determine ET processes vary greatly over different surface conditions. Evaporation can be considered as a pure physical process whereas transpiration is more regarded as a biological or plant physiological process (Scott et al. 2006). These two processes are relatively independent but can be strongly coupled in certain circumstances, which brings further difficulties in accurately quantifying ET over vegetated surfaces, especially for non-uniform vegetated surfaces. Nevertheless, in most ecosystems, vegetation covers land surface non-uniformly, such as in forests, shrublands and savannas. Even for agricultural ecosystem where the spatial distribution of vegetation is relatively uniform, its vegetation cover still shows an obvious temporal variability. Moreover, the distributions of water and energy in the natural ecosystems are also spatially and temporally heterogeneous. All these heterogeneities have imposed a big challenge for successful quantifications of ET in most cases.

This dissertation will focus on ET estimation over vegetated surfaces, particularly over partial and non-uniform vegetated surface, with the aim of gaining a greater understanding ET processes under different vegetation cover conditions and therefore to improve ET models. The developed models will be applied to estimating ET in both natural and agricultural ecosystems. The outputs of this study will potentially provide, on one hand, theory basis for natural ecosystem protection and restoration, and technique supports for the design of water-saving irrigation and sustainable water resources management in arid environments.

1.2 Current Research Status

1.2.1 Land Surface Evapotranspiration Models

Accurate quantification of ET and its components can be achieved by using a combination of in situ measurements, such as the eddy covariance systems, Bowen-ratio systems, weighing lysimeter, sap-flow meters, and isotope sampling (Baldocchi

2003; Yang et al. 2013; Zhang et al. 2008). However, such field-based observations are often costly and can only provide measurements of ET or E and T at the point scale. As a result, mathematical modelling in combination with more or less meteorological and/or remote sensing data becomes a powerful tool to quantify ET over larger areas and longer periods. Comprehensive reviews of ET quantification can be found in Wang and Dickinson (2012), for example. Here, we will first categorize these ET models into two groups (i.e., ground measurement-based models and remote sensing-based model) and then briefly go through them in terms of their advantages and disadvantages.

1.2.1.1 Ground Measurement-Based ET Models

Estimation of ET can be dated back to the year of 1802 when Dolton proposed his first evaporation formula. Afterwards, with the development of ET theories and advancement of observation skills, hundreds of model for estimating land surface ET have been proposed by researchers. In summary, these models can be classified into four types: empirical model, water balance model, micrometeorological model and soil-vegetation-atmosphere transfer (SVAT) model, among which, micrometeorological model and SVAT model have been used most often (Table 1.1).

For vegetated surfaces, differences in various micrometeorological models are characterized by their different parameterizations of vegetation in the models. Vegetation distributions and canopy structures vary among ecosystems, resulting in different sources of sensible and latent heat fluxes, which requires different treatments in ET models. With respect to different canopy types, there are currently three types of ET models which are all based on Prandtl's mixing-length theory, including single source model, dual source model and multi-source model.

Table 1.1 Summary of ground measurement-based ET models

Type	Model/method	References
Empirical model	Evaporation pan	Snyder (1992)
	Temperature-based empirical method	Lei et al. (1988)
	Radiation-based empirical method	Lei et al. (1988)
	Dalton aerodynamic equation	Dalton (1802)
	Hargreaves equation	Hargreaves and Allen (2003)
Micrometeorological model	Energy balance model (Bowen-ratio method, Priestley-Taylor equation)	Bowen (1926), Priestley and Taylor (1972)
	Turbulent diffusion method	Yu et al. (2006)
	Combined method (Penman model, Penman-Monteith model, Complementary method)	Bouchet (1963), Monteith (1965), Penman (1948)
SVAT model	SVAT model	Kang et al. (1994)

(1) Single source model

Single source model has only one source of sensible and latent heat fluxes, which considers the land surface as a uniform layer of the combination of soil and vegetation components. Penman model and Penman-Monteith (P-M) model are typical single source models (Penman 1948; Monteith 1965). Penman model assumes a saturated surface, which has been widely used to estimate potential evaporation. Monteith introduced the concept of canopy resistance into the Penman model and proposed the P-M model for calculating actual ET over non-saturated surfaces. The P-M model has a solid physical basis, which explicitly explains the mechanism of ET processes and has been used extensively over various surface conditions with different vegetation cover. In addition, the P-M model has been recommended by Food and Agriculture Organization of United Nation as the standard method for quantifying ET in agricultural land (Allen et al. 1998).

Single source model has a simple model structure and few easily-determined parameters, which guarantee the model to be readily applied. However, single source model treats the land surface as a uniform layer, which only accounts for energy and mass exchanges between the bulk soil-vegetation surface and the atmosphere. As a result, single source model is only suitable for certain canopy type, i.e., single layer closed canopy. In addition, single source model cannot distinguish between evaporation from soil and transpiration from canopy.

(2) Dual source model

Considering contributions of energy fluxes from different components (soil vs. vegetation), dual source ET models have been proposed to more precisely depict water and heat transfers from sparse or heterogeneous canopies. "Dual source" indicates fluxes from vegetation canopy and bare soil, respectively. Based on different ways of energy partitioning and various resistance systems, dual source models can be further categorized into three types, i.e., the layer model, the patch model and the hybrid model.

Layer model: Layer model is also known as the coupled model in which each source of water and heat flux is superimposed and coupled, such as the Shuttleworth-Wallace dual source model (the S-W model) (Shuttleworth and Wallace 1985). It considers the land surface as two different but interacted layers (i.e., the vegetation layer and the soil layer). Solar radiation firstly comes onto the vegetation layer and then penetrates through the canopy onto soil surface following a certain rule (e.g., the Beer's law), and soil evaporation and canopy transpiration are calculated from the P-M model, respectively. In such a model, energy fluxes sourced from soil will be firstly transferred onto the canopy height and interact with those from canopy and then exchange with the above atmosphere.

The S-W model has been extensively used for estimating ET over a wide range of vegetated surfaces. Ortega-Farias et al. (2010) successfully applied the S-W model to estimate ET in a drip-irrigated vineyard in Chili. Zhang et al. (2008) also reported a good performance of the S-W model in a vineyard in the Northwest China. Hu et al. (2009) used the S-W model to estimate ET at four grassland sites and found an error range of 8–15 %.

Patch model: For patchy vegetated surfaces, the interaction among patches can often be ignored, particularly when distance between vegetation patches is large. In a patch model, each patch receives the same radiation loading (i.e., full radiation) and acts independently of the other (advection effect excepted). The total flux of sensible or latent heat per unit area of soil is considered as a mean of the component fluxes weighted by their relative area (e.g., fractional vegetation cover, F_c). For each patch, ET is calculated from the P-M formulation.

Patch model has a relative simple model structure and low computing requirement. Therefore, it has been widely used in large-scale land surface modelling and coupled with regional climate models. One representative if the N95 model developed by Norman et al. (1995), which was later implemented with remote sensing data to map ET at regional scale. In addition, ISBA (Noilhan and Planton 1989) and CLASS (Verseghy 1991) are also typical patch models.

Hybrid model: Previous studies have pointed out that the later model performs better over uniformly vegetated surfaces with higher vegetation cover, whereas the patch model is more suitable for more clumped vegetation. In another word, both two-layer and two-patch models are limited somehow within a certain range of vegetated surfaces. However, in natural environment, vegetation distribution usually exhibits large spatial (spatial gradient) and temporal (seasonal change) variations, which deviates greatly from the ideal vegetation cover conditions required by either the layer or the patch model. Therefore, use of either model to estimate ET over larger area with different characteristics of vegetation distribution may result in considerable errors. As shown in Fig. 1.1, the ideal vegetation distribution for the layer model and the patch model is located in two ends: uniform and high vegetation cover and patchy and low vegetation cover. One challenge is that is there any ways to combine the two models to better describe the transition between the two extreme ends?

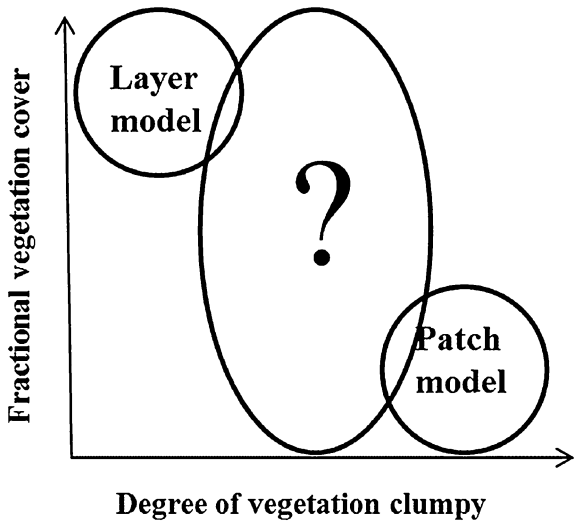

Fig. 1.1 The scope of application of the layer and patch models

To address this challenge, Guan and Wilson (2009) proposed a hybrid dual-source model (the TVET model) to estimate potential evaporation (PE) and potential transpiration (PT) by combining the later with the patch approaches. The TVET model adopts the layer approach to allocate available energy between components and to estimate aerodynamic resistance, but uses the patch approach to calculate PE and PT. As a result, both the evaporation from both under- and inter-canopy soil surfaces are considered and distinguished. Guan and Wilson (2009) demonstrated that the simple combination of the layer and patch approaches could provide better PE and PT estimates over a wide range of vegetated surfaces. A detail description of the TVET model can be found in Guan and Wilson (2009).
(3) Multi-source model
For surfaces with multiple vegetation types, neither the single source nor dual source model can truly capture energy flux from the surface due to different canopy resistances and structures among different vegetation types. To estimate ET over such surface, based on the layer model, Dolman (1993) distinguished the vegetation layer into upper-canopy and understory layers and estimated energy fluxes from each layer respectively. In addition, Williams et al. (1996) separated the single canopy into different layers at various heights, and the total flux from the entire canopy was calculated as the sum of those from each layer. Strictly speaking, this model should also be considered as multi-source model, as vegetation layer at different heights receive different radiation loading and have different canopy resistances. Similar models include the WAVES model (Zhang et al. 1996), the SVAT-CN model (Harly and Tenhunen 1991) and the HIRVAC model (Goldberg and Bernhofer 2001).

1.2.1.2 Remote Sensing-Based ET Models

Satellite remote sensing has provided an unprecedented opportunity for capturing ET across a variety of spatial and temporal scales that are not attainable by conventional techniques (e.g., Carlson 2007). In general, the remote sensing-based ET models can be grouped into three types, i.e., empirical model, energy balance model and vegetation index model.
(1) Empirical model
Empirical or semi-empirical models are often accomplished by employing empirical relationships and making use of data mainly derived from remote sensing observations with minimum ground-based measurement (Li et al. 2009). The main theory of the empirical method was firstly proposed by Jackson et al. (1997), in which the daily ET was directly related with the difference between instantaneous surface temperature and air temperature measured near midday at about 13:30 to 14:00 local time. Seguin and Itier (1983) further investigated the relationship between thermal images and land surface ET, and applied the model of Jackson et al. (1997) to large spatial scales. However, one key assumption of these models is that the constant Bowen ratio over a day, which is somehow deviates from the reality. Triangle model and trapezoid model (e.g., Jiang and Islam 1999) are another two

typical empirical models that are developed from Jackson et al. (1997). Both models require determination of two extreme boundaries, i.e., the hot edge on which ET equals zeros and the cold edge on which ET occurs at its potential rate. The actual ET lies within the range of the two extreme conditions and is determined via a certain interpolation method. Long et al. (2012) derived a theoretical solution for the two extreme boundaries which provides the triangle and trapezoid models with a sounder physical basis.

(2) Energy balance model

The energy balance remote sensing ET model estimates other energy components explicitly and considers latent heat (ET) as the residual within the surface energy balance equation. Based on different parameterizations of vegetation in the model, energy balance model can be further classified into single source model and dual source model. The SEBAL (Bastiaanssen et al. 1998) and SEBS (Su 2002) model are typical single source energy balance models. SEBAL circumvents the difficulties in estimating true values for aerodynamic temperature (T_{aero}) and air temperature (T_a) at reference height by assuming that the temperature difference (dT) between T_{aero} and T_a is linearly correlated with land surface temperature (LST). The relationship between dT and LST is determined by using two "anchor" points where a value for sensible heat can be reliably estimated based on a prior knowledge of the fluxes over dry land (hot pixel) and wet land (cold pixel). As a result, successful application of SEBAL also requires an area that is large enough to encompass both extreme hot and extreme cold conditions. However, the land cover may become more non-uniform with the increase of study extent and very likely the required linear assumption in SEBAL is no longer valid. Moreover, visual selection of hot and cold pixels in SEBAL is usually associated with great subjectivity, resulting in further uncertainties in the model estimates. Different from SEBAL, SEBS does not need manual selection of extreme pixels. Instead, it assumes that the extreme dry and wet conditions theoretically existed within each pixel. Nevertheless, this assumption makes the SEBS model very sensitive to meteorological inputs and thus more suitable for areas with relatively uniform meteorological fields.

Compared with one-source models which simulate bulk ET from the land surface by primarily using remotely sensed land surface temperature (LST) and vegetation index (VI) (e.g., Bastiaanssen et al. 1998; Carlson 2007; Long and Singh 2012; Su 2002), the two-source modes have the physics of depicting and simulating E and T separately over larger areas (e.g., Long and Singh 2012; Mu et al. 2011; Norman et al. 1995; Yang and Shang 2013), which could be more helpful in understanding hydrological and biological processes of the terrestrial biosphere. However, one fundamental difficulty in two source remote sensing ET models is that two-source approaches require knowledge of surface temperatures of soil and vegetation canopy, and this information is often unattainable directly from satellite images because remotely sensed LST is a composite temperature of heterogeneous surfaces. As a result, various approaches were developed to decompose remotely sensed LST into temperature components and consequently separately quantify E and T (e.g., Kustas et al. 2005). In the classic Two-source Energy Balance model (TSEB, Norman et al. 1995; Kustas and Norman 1997), the Priestley-Taylor (P-T)

parameterization is adopted to obtain a first estimate of T and canopy temperature (Priestley and Taylor 1972), and then to calculate E and T in an iterative manner. A similar idea was adopted by Kustas and Norman (1997) and Anderson et al. (2005) and others. In addition, van der Keur et al. (2001) implemented remote sensing data into a dual source SVAT model (i.e., DAISY) and developed remote sensing-based DAISY model. Moreover, based on trapezoid scheme, Long and Singh (2012) proposed a dual source trapezoid ET model, which has been successfully applied in an agricultural region in central Iowa, USA.

(3) Vegetation index model

Vegetation index model estimates ET from the P-M equation, in which the surface resistance is expressed as a function of remotely sensed vegetation index. Cleugh et al. (2007) claimed that traditional energy balance models do not considered the controlling effect of vegetation on ET. Besides, they found that using the P-M model coupled with a simple canopy resistance model (a function of vegetation index) can provide better ET estimates than energy balance model. Based on this, Cleugh et al. (2007) produced monthly ET maps over Australia at a 1 km spatial resolution. Leuning et al. (2008) improved the canopy resistance model and tested the model at 15 flux sites in North America and Australia. Mu et al. (2007, 2011) further improved the model of Cleugh et al. (2007) and produced a global ET product based on MODIS data. This ET product has been accepted as the standard ET product by MODIS community.

1.2.2 Current Issues

Although there have been great progress in ET studies, there are still many issues that requires further investigation, particularly for ET mechanism and quantification over non-uniformly vegetation surfaces. Here, we list four types of issues that are commonly existed and are going to be reached in this dissertation.

(1) The applicability of different ET models

Even though numerous ET models have been developed during past decades, consensus on model applicability has not been reached yet. Transfer of mass and energy between the land and the atmosphere is an extremely complex non-linear problem, and no model is able to explicitly describe every detail within that process. Rather, models aim to reasonably simplify the entire process and to capture the most important process that controls ET. For different environmental setting with various vegetation and soil moisture conditions, the way of simplification in different ET models can be very different, which results in different model applicability over different environmental conditions. For example, the P-M model is only applicable over fully and uniformly vegetated surfaces, and for sparse vegetation, layer model works better over uniformly vegetated surfaces whereas patch model is more suitable for patchy vegetated surfaces (Lhomme and Chehbouni 1999).

In addition, more efforts have been made for quantifying ET in agricultural ecosystems during previous studies, while quantification of ET in natural

ecosystems is relatively under-attendant. However, taking China as an example, agricultural lands occupy only 19 % of the national area, whereas forests and grasslands account for 24 and 31 % of the total land, respectively (Wang et al. 2001). Therefore, more attention should be paid to ET model applicability in natural ecosystems in further studies.

(2) Sub-processes of land surface evapotranspiration and their interactions

As stated above, the process of evapotranspiration consists of many sub-processes that describe the exchange of vapour and energy between the land and the atmosphere. To gain a deeper insight into ET process and to further improve the current ET models, it is necessary to better understand those sub-processes in terms of their mechanisms and interactions. For example, how soil water is extracted by plant root and then moved upwards to leaf surfaces for transpiration? At which depth in the soil evaporation actually occurs? What the effect of evaporation water loss on plant root water uptake from the surrounding soil? How much sensible heat from soil surfaces will be used by plant transpiration? How much intercepted rain water will be directly absorbed by leaves and to what extent plant transpiration will be prevented by those intercepted water? To answer these questions is an urgently needs in further ET studies.

One possible way to look at these issues is by Soil-Plant-Atmosphere Continuum (SPAC) modelling, which considers mass and water transfers through the entire SPAC system and the interactions among different sub-processes (Cowan 1965; Philip 1966). The outcome of SPAC modelling is not merely some final estimates of ET or primary production, but also includes almost every variable that plays a role in the entire process. This would greatly enhance our understanding of each sub-process. However, they ability of a SPAC model to represent the reality depends largely on the model complexity. Nevertheless, the more complex the model is, the more inputs it may requires, which would limit the model applicability. There is always a trade-off between data requirement, model complexities and uncertainties, as well as purposes of studies and applications.

(3) Improvement on remote sensing ET models and their application in real water management

Although there have been more than 40 years of progress in remote sensing ET models, there is still room for further model improvement. A particular focus should be made to two source remote sensing ET models, as they have been proved to outperform the one source models over a wide range of surface conditions.

Besides the improvement of remote sensing ET model itself, a re-look is needed at remote sensing ET model applications. In previous studies, remote sensing ET models are more served as a pure research toll; however, they have rarely been applied in real water management (Yang et al. 2012). Compared with traditional ground-based ET models, remote sensing-based ET model has its irreplaceable advantage in producing ET maps over large areas, which is the key to understand the hydrological cycle and manage water resource (e.g., monitor water consumption) at large spatial scales (e.g., basin scale).

(4) Exploration of new theories of ET estimation
Up to date, development of ET models still relies on the three basic theories that can be dated back to 19th century, i.e., the Dolton's evaporation theory, Monin-Obukhov similarity theory and energy balance theory. There is an urgent need for developing new theories that could potentially advance our current understanding of ET processes. However, this is also the most challenging issue in ET studies. Nevertheless, there have been numerous attempts on this issue, such as the thermodynamic entropy theory (Bobylev et al. 2001), machine learning approach (Yang et al. 2006; Sudheer et al. 2002) and ecosystem optimality theory (Lei et al. 2008).

1.3 Research Outline

This dissertation work looks at land surface ET estimation, with a special focus on partially vegetated ecosystems. Firstly, it will discuss the applicability of different ET models in estimating ET and its partitioning under various vegetation cover conditions. Based on this, a new dual source ET model that is applicable for different vegetation cover conditions will be developed. In addition, on one hand, the developed ET model will be coupled with a soil water/heat dynamic model to build a SPAC model; on the other hand, this model will be incorporated with remote sensing to estimate ET at regional scales. Moreover, a new theory of ET estimation by exploiting the linkage of the carbon and water cycles will be proposed. Finally, the developed remote sensing ET model will be applied to examine the spatial and temporal patterns of ET and its response to water management in a large irrigation district in North China (i.e., the Hetao Irrigation District). The outline of this dissertation is shown in Fig. 1.2 and the main content of each chapter is given below.

Chapter 2 compares three different two source ET models in estimating potential ET and its partitioning (i.e., potential evaporation and potential transpiration) over various vegetation cover conditions. A detailed evaluation is then made in terms of their advantages and disadvantages.

Chapter 3 develops a hybrid dual source ET model, which is able to simulate ET under different vegetation cover conditions. The developed model is tested and compared with three other commonly used ET models in four different ecosystems (i.e., forest, shrubland, grassland and cropland).

Chapter 4 built a new soil-plant-atmosphere continuum model (HDS-SPAC) by coupling the hybrid dual source ET model with a soil water/heat transfer model. The HDS-SPAC model is then tested at two sites, including one agricultural site and one forest site. For model application in forest site, a simple non-invasive filed experiment to determine and parameterize plant root water uptake model is designed.

Chapter 5 developed a new two source remote sensing ET model (i.e., HTEM) by coupling the hybrid dual source scheme with a theoretically determined vegetation index/land surface temperature trapezoidal space. Data from two agricultural regions in USA and China are used for model validation.

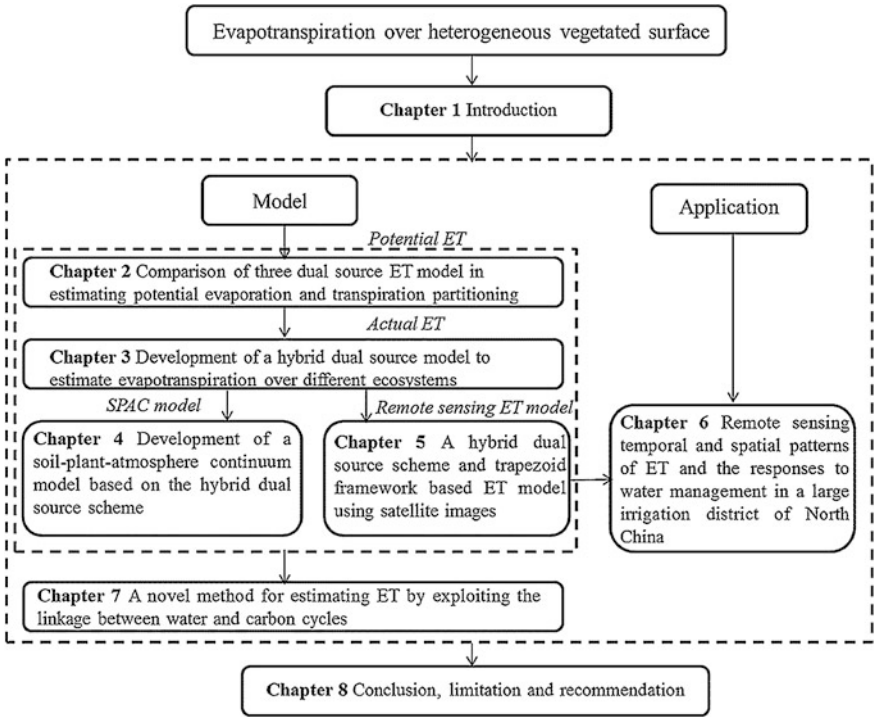

Fig. 1.2 Outline of the dissertation

Chapter 6 proposes a new theory for ET estimation over vegetated surfaces by exploiting the linkage between the carbon and water cycles.

Chapter 7 examines the spatial and temporal patterns of ET and its response to water management in a large irrigation district in North China (i.e., the Hetao Irrigation District) based on the HTEM model developed in Chap. 5.

References

Allen R, Pereira L, Raes D et al (1998) Crop evapotranspiration: guidelines for computing crop water requirements. Food and Agriculture Organization, Rome

Anderson MC, Norman JM, Kustas WP et al (2005) Effects of vegetation clumping on two-source model estimates of surface energy fluxes from an agricultural landscape during SMACEX. J Hydrometeorol 6:892–909

Baldocchi DD (2003) Assessing the eddy covariance technique for evaluating carbon dioxide exchange rates of ecosystems: past, present and future. Glob Change Biol 9:479–492

Bastiaanssen WGM, Menenti M, Feddes RA et al (1998) A remote sensing surface energy balance algorithm for land (SEBAL)—1. Formulation. J Hydrol 213:198–212

Bonan GB (2002) Ecological climatology: concepts and applications. Cambridge University Press, New York

Bouchet RJ (1963) Evapotranspiration reele et potentielle, signification climatique. IAHS, Gentbrugge, Belgium
Bowen IS (1926) The ratio of heat losses by conduction and by evaporation from any water surface. Phys Rev 14:743–787
Bobylev AV, Grzhibovskis R, Heintz A (2001) Entropy inequalities for evaporation/condensation problem in rarefied gas dynamics. J Stat Phys 102:1151–1176
Carlson T (2007) An overview of the "triangle method" for estimating surface evapotranspiration and soil moisture from satellite imagery. Sensors 7:1612–1629
Cleugh HA, Leuning R, Mu Q et al (2007) Regional evaporation estimates from flux tower and MODIS satellite data. Remote Sens Environ 106:285–304
Cowan IR (1965) Transport of water in the soil-plant-atmosphere system. J Appl Ecol 2:221–239
Dalton J (1802) Experimental essays on the constitution of mixed gas; on the force of steam or vapor from water and other liquids in different temperatures, both in a torricellian vacuum and in air; on evaporation and on the expansion of gases by heat. Mem Manchester Lit Phil Soc 5:535–602
Deng XP, Shan L, Zhang H et al (2006) Improving agricultural water use efficiency in arid and semiarid areas of China. Agric Water Manag 80:23–40
Dolman AJ (1993) A multiple-source land surface energy balance model for use in general circulation models. Agric For Meteorol 65:21–45
Goldberg V, Bernhofer Ch (2001) Quantifying the coupling degree between land surface and the atmosphere boundary layer with the coupled vegetation-atmosphere model HIRVAC. Ann Geophys 19:581–587
Guan H, Wilson JL (2009) A hybrid dual-source model for potential evaporation and transpiration partitioning. J Hydrol 377:405–416
Hargreaves G, Allen R (2003) History and evaluation of Hargreaves evapotranspiration equation. J Irrig Drain Eng 129:53–63
Harly PC, Tenhunen JD (1991) Modelling crop photosynthesis—from biochemistry to canopy. In: Boote KJ, Loomis RS (eds) CSSA special publication no. 19. American Society of Agronomy and Crop Science of American, Madison
Hu Z, Yu G, Zhou Y et al (2009) Partitioning of evapotranspiration and its controls in four grassland ecosystems: application of a two-source model. Agric For Meteorol 149:1410–1420
Jackson RD, Reginato RJ, Idso SB (1997) Wheat canopy temperature: a practical tool for evaluating water requirements. Water Resour Res 13:651–656
Jiang L, Islam S (1999) A methodology for estimation of surface evapotranspiration over large areas using remote sensing observations. Geophys Res Lett 26:2773–2776
Kang S, Liu X, Xiong Y (1994) Theory of water transport in soil-plant-atmosphere continuum and its application. China Waterpower Press, Beijing (in Chinese)
Kustas WP, Norman JM (1997) A two-source approach for estimating turbulent fluxes using multiple angle thermal infrared observations. Water Resour Res 33:1495–1508
Kustas WP, Hatfield JL, Prueger JH (2005) The soil moisture-atmosphere coupling experiment (SMACEX): background, hydrometeorological conditions, and preliminary findings. J Hydrometeorol 6:791–804
Lei Z, Yang S, Xie S (1988) Soil water dynamics. Tsinghua Press, Beijing (in Chinese)
Lei H, Yang D, Schymanski S et al (2008) Modeling the crop transpiration using an optimality-based approach. Sci China Ser E: Technol Sci 51:60–75
Leuning R, Zhang YQ, Rajaud A et al (2008) A simple surface conductance model to estimate regional evaporation using MODIS leaf area index and the Penman-Monteith equation. Water Resour Res 44:W10419
Lhomme JP, Chehbouni A (1999) Comments on dual-source vegetation-atmosphere transfer models. Agric For Meteorol 1999:269–273
Liu CM, Zhang X, Zhang Y (2002) Determination of daily evaporation and evapotranspiration of winter and maize by large-scale weighting lysimeter and micro-lysimeter. Agric For Meteorol 111:109–120

Li Z, Tang R, Wan Z et al (2009) A review of current methodologies for regional evapotranspiration estimation from remotely sensed data. Sensors 9:3801–3853
Long D, Singh VP (2012) A two-source trapezoid model for evapotranspiration (TTME) from satellite imagery. Remote Sens Environ 121:370–388
Long D, Singh VP, Scanlon BR (2012) Deriving theoretical boundaries to address scale dependencies of triangle models for evapotranspiration estimation. J Geophys Res 117:D05113
Monteith JL (1965) Evaporation and environment. Symp Soc Exp Biol 19:205–234
Mu Q, Heinsch FA, Zhao M et al (2007) Development of a global evapotranspiration algorithm based on MODIS and global meteorology data. Remote Sens Environ 111:519–536
Mu Q, Zhao M, Running SW (2011) Improvements to a MODIS global terrestrial evapotranspiration algorithm. Remote Sens Environ 115:1781–1800
Noilhan J, Planton S (1989) A simple parameterization of land surface processes for meteorological models. Mon Weather Rev 117:536–549
Norman JM, Kustas WP, Humes KS (1995) Source approach for estimating soil and vegetation energy fluxes in observations of directional radiometric surface temperature. Agric For Meteorol 77:263–293
Oki T, Kanae S (2006) Global hydrological cycles and world water resources. Science 313: 1068–1072
Ortega-Farias S, Poblete-Echeverría C, Brisson N (2010) Parameterization of a two-layer model for estimating vineyard evapotranspiration using meteorological measurements. Agric For Meteorol 150:276–286
Penman HL (1948) Natural evaporation from open water, bare soil and grass. Proc R Soc A 193:120–145
Philip JR (1966) Plant water relations: some physical aspects. Ann Rev Plant Physiol 17:245–268
Priestley CHB, Taylor RJ (1972) On the assessment of surface heat flux and evaporation using large-scale parameters. Mon Weather Rev 100:81–92
Rosen RD (1999) The global energy cycle. In: Browning KA, Gurney RJ (eds) Global energy and water cycles. Cambridge University Press, Cambridge
Scott RL, Huxman TE, Cable WL et al (2006) Partitioning of evapotranspiration and its relation to carbon dioxide exchange in a Chihuahuan Desert shrubland. Hydrol Process 20:3227–3243
Seguin B, Itier B (1983) Using midday surface temperature to estimate daily evaporation from satellite thermal IR data. Int J Remote Sens 4:371–383
Shuttleworth WJ, Wallace JS (1985) Evaporation from sparse crops-an energy combination theory. Q J R Meteorol Soc 111:839–855
Snyder R (1992) Equation for evaporation pan to evapotranspiration conversions. J Irrig Drain Eng 118:977–980
Su Z (2002) The surface energy balance system (SEBS) for estimation of turbulent heat fluxes. Hydrol Earth Syst Sci 6:85–99
Sudheer KP, Gosain AK, Mohana D et al (2002) Modeling evaporation using an artificial neural network algorithm. Hydrol Process 16:3189–3202
van der Keur P, Hansen S, Schelde K et al (2001) Modification of DAISY SVAT model for potential use of remotely sensed data. Agric For Meteorol 106:215–231
Verseghy DL (1991) Class—a Canadian land surface scheme for GCMS. I. Soil model. Int J Climatol 11:111–133
Wang K, Dickinson RE (2012) A review of global terrestrial evapotranspiration: Observation, modeling, climatology, and climatic variability. Rev Geophy 50:RG2005
Wang S, Liu J, Zhang Z et al (2001) Analysis on spatial-temporal features of land use in China. Acta Geogr Sinica 56:631–639 (in Chinese)
Williams M, Rastetter EB, Fernandes DN et al (1996) Modelling the soil-plant-atmosphere continuum in a Quercus-Acer stand at Harvard Forest: the regulation of stomatal conductance by light, nitrogen and soil/plant hydraulic properties. Plant Cell Environ 19:911–927
Yang Y, Shang S (2013) A hybrid dual-source scheme and trapezoid framework-based evapotranspiration model (HTEM) using satellite images: algorithm and model test. J Geophys Res Atmos 118:2284–2300

Yang F, White MA, Michaelis AR et al (2006) Prediction of continental-scale evapotranspiration by combining MODIS and AmeriFlux data through support vector machine. IEEE Trans Geosci Remote Sens 44:3452–3461

Yang Y, Shang S, Jiang L (2012) Remote sensing temporal and spatial patterns of evapotranspiration and the responses to water management in a large irrigation district of North China. Agric For Meteorol 164:112–122

Yang Y, Guan H, Hutson JL et al (2013) Examination and parameterization of the root water uptake model from stem water potential and sap flow measurements. Hydrol Process 27: 2857–2863

Yu G, Sun X, Niu D et al (2006) Principles of flux measurement in terrestrial ecosystems. High Education Press, Beijing (in Chinese)

Zhang L, Dawes WR, Hatton TJ (1996) Modelling hydrologic processes using a biophysically based model—application of WAVES to FIFE and HAPEX-MOBILHY. J Hydrol 185: 147–169

Zhang B, Kang S, Li F et al (2008) Comparison of three evapotranspiration models to Bowen ratio-energy balance method for a vineyard in an arid desert region of northwest China. Agric For Meteorol 148:1629–1640

Chapter 2
Comparison of Dual-Source Evapotranspiration Models in Estimating Potential Evaporation and Transpiration

2.1 Introduction

Potential evapotranspiration (PET) is defined as the amount of ET that could occur if a sufficient water source were available, the value of which is a function of atmospheric conditions and surface vegetation distribution characteristics. However, traditional empirical PET models, such as the Hargreaves model and Priestley-Taylor model, only account for the effect of atmospheric demand on PET, whereas the impact of vegetation on PET is simply ignored. On the other hand, physical-based PET models, such as the Penman-Monteith model (refer to as the P-M model hereafter), take vegetation effect on PET into consideration. Nevertheless, the P-M model treats the land surface as a uniform layer, where the vegetation covers the land surface fully and uniformly as a "big leaf". This simplification of vegetation treatment makes the P-M model unable to distinguish evaporation from soil (E) and transpiration from canopy (T), and therefore may not be appropriate for use in partially vegetated areas.

Considering contributions of energy fluxes from different components (soil vs. vegetation), dual-source ET models have been proposed to more precisely depict water and heat transfers from sparse or heterogeneous canopies. In particular, Shuttleworth and Wallace (1985) developed a two layer ET model, in which each source of water and heat flux is superimposed and coupled. This model is also referred to as the coupled model. In contrast, Lhomme et al. (1994) suggested that for surface with low vegetation cover or patchy vegetation, the interaction between components is generally very weak so that fluxes from each source interact independently with each other and directly with the above atmosphere. This type model is known as the patch model or uncoupled model. By combining the layer model and the patch model, Guan and Wilson (2009) proposed a hybrid dual source, which claims to be applicable for a range of vegetated surface.

Besides a general better performance of ET estimation, dual source models are also capable of distinguishing different processes of E and T. To that end, dual

Y. Yang, *Evapotranspiration Over Heterogeneous Vegetated Surfaces*,
Springer Theses, DOI 10.1007/978-3-662-46173-0_2

source models contains a greater application potential for ET estimation and partitioning, in comparison to empirical ET models and single source ET models (e.g., P-M model). However, consensus on the applicability of different dual source ET models has not been achieved yet. The objective of this chapter is to compare the performance of the three above-mentioned dual source models in estimating PET and the partitioning between PE and PT. The comprehensive comparison could provide important implications for developing model for actual ET estimation at various spatial scales (see Chaps. 3–5).

2.2 Evapotranspiration Models

2.2.1 Penman-Monteith Model

The description of the Penman-Monteith (P-M) model is given in Eq. (2.1), and the model structure is shown in Fig. 2.1a.

$$\lambda \mathrm{ET} = \frac{\Delta(R_\mathrm{n} - G) + \rho C_\mathrm{p} D / r_a}{\Delta + \gamma[1 + (r_c / r_a)]} \tag{2.1}$$

where λ is the latent heat of vaporization; R_n and G are net radiation and soil heat flux, respectively (W/m^2); Δ is the slope of saturation vapor pressure—temperature curve (kPa/K), ρ is the air density (kg/m^3), C_p is the specific heat of air at constant pressure (J/(kg K)), D is the vapor pressure deficit (kPa), γ is the psychrometric constant (kPa/K), r_a is aerodynamic resistance (s/m), and r_c is bulk surface resistance (s/m).

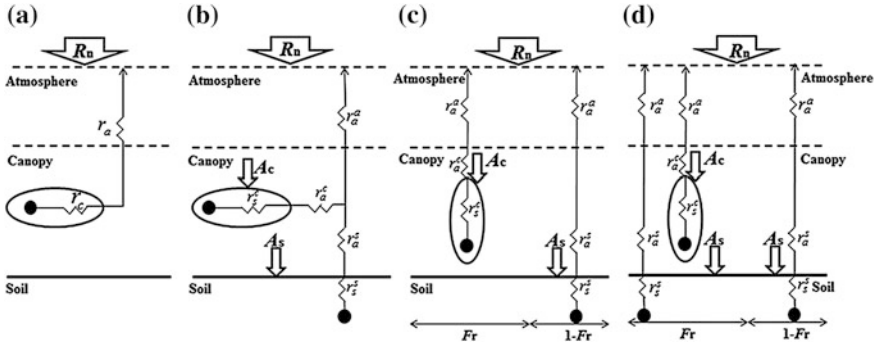

Fig. 2.1 Structure of the Penman-Monteith model (**a**); Shuttleworth-Wallace model (**b**); Two-Patch model (**c**); and TVET model (**d**). The nomenclature used is given in Sect. 2.2 (Yu et al. 2014)

The aerodynamic resistance determines the transfer of heat and water vapor from evaporation surface into the air above the canopy, which is calculated from Allen et al. (1998),

$$r_a = \frac{\ln(\frac{z_m - d}{z_{om}} + \varphi_M)\ln(\frac{z_h - d}{z_{oh}} + \varphi_H)}{k^2 u(z_m)} \tag{2.2}$$

where k is von Karman's constant (=0.41), d is zero plane displacement height (m), z_m and z_h are height of wind measurement and humidity measurement, respectively (m). $u(z_m)$ is wind speed at height z_m (m/s), z_{om} is the roughness length governing momentum transfer, and z_{oh} is the roughness length governing heat and vapor transfer. Both roughness lengths (z_{om}, z_{oh}) and zero plane displacement height (d) are defined as functions of vegetation height (h), given in Campbell and Norman (1998). φ_M and φ_H represent atmospheric diabatic correction factors for momentum and heat (or vapor) respectively and can be found in Brutsaert (1982).

The bulk surface resistance is estimated from Jarvis (1976),

$$r_c = \frac{1}{2LAI}\frac{r_{ST\_min}}{f_1 f_2 f_3 f_4} \tag{2.3}$$

where r_{ST_min} is the minimum stomatal resistance (s/m). f_1, f_2 and f_3 are factors accounting for the influence of shortwave radiation, air vapor deficit, and air temperature on stomatal resistance, respectively, and are estimated following Noilhan and Planton (1989). Parameter f_4 accounts for the influence of root zone soil moisture on stomatal resistance, which is calculated from

$$f_4(\theta) = \begin{cases} 0 & \theta \le \theta_W \\ \frac{\theta - \theta_W}{\theta_F - \theta_W} & \theta_W < \theta < \theta_F \\ 1 & \theta_F \le \theta \end{cases} \tag{2.4}$$

where θ is the soil water content within the root-zone (cm^3/cm^3), θ_F and θ_W are the soil water content at the field capacity and wilting point, respectively.

2.2.2 Shuttleworth-Wallace Model

The Shuttleworth-Wallace (S-W) model is a typical two-layer model, which is also the basis of other multi-layer models. The model structure is shown in Fig. 2.1b. In the S-W model, ET is calculated from,

$$\lambda ET_a = \lambda E + \lambda T = C_s PM_s + C_c PM_c \tag{2.5}$$

where λE is the latent heat from soil and λT is the latent heat from canopy (W/m^2). Subscript s and c represent soil and canopy component, respectively. The expressions of PM and C are given by

$$PM_s = \frac{\Delta A + \left[\rho C_{\mathrm{p}} \mathrm{D} - \Delta r_a^s (A - A_s)\right]/(r_a^a + r_a^s)}{\Delta + \gamma\left[1 + (r_s^s/(r_a^a + r_a^s))\right]} \tag{2.6}$$

$$PM_c = \frac{\Delta A + \left[\rho C_{\mathrm{p}} \mathrm{D} - \Delta r_a^c A_s)\right]/(r_a^a + r_a^c)}{\Delta + \gamma\left[1 + r_s^c/(r_a^a + r_a^c)\right]} \tag{2.7}$$

$$C_c = 1/(1 + R_c R_a / R_s (R_c + R_a)) \tag{2.8}$$

$$C_s = 1/(1 + R_s R_a / R_c (R_s + R_a)) \tag{2.9}$$

$$R_a = (\Delta + \gamma) r_a^a \tag{2.10}$$

$$R_s = (\Delta + \gamma) r_a^s + \gamma r_s^s \tag{2.11}$$

$$R_c = (\Delta + \gamma) r_a^c + \gamma r_s^c \tag{2.12}$$

where r_a^a is the aerodynamic resistance between mean canopy surface and the reference height (s/m); r_a^s is the aerodynamic resistance between soil surface and mean canopy surface (s/m); r_a^c is the aerodynamic resistance between mean leaf surface and mean canopy surface (s/m); r_s^c is the canopy surface resistance, and r_s^s is the soil surface resistance (s/m). A and A_s are the total available energy and the available energy for the soil component (W/m^2), respectively, which can be estimated from

$$A = R_n - G \tag{2.13}$$

$$A_s = R_n \exp(-k_c LAI) - G \tag{2.14}$$

where k_c is the extinction coefficient of radiation attenuation, and is set to be 0.7 for deciduous broadleaf forests, 0.5 for evergreen needle-leaf forests, and 0.4 for herbs (Lhomme and Chehbouni 1999; Monsi and Saeki 1953).

The aerodynamic resistance r_a^a and r_a^s in the S-W model were assumed to change linearly between those for the surface with full vegetation cover (assumed equal to LAI = 4) and for bare soil, weighted by leaf area index (Shuttleworth and Wallace 1985),
when 0 < LAI < 4

$$r_a^a = \frac{1}{4} LAI \times r_a^a(\alpha) + \frac{1}{4}(4 - LAI) \times r_a^a(0) \tag{2.15}$$

$$r_a^s = \frac{1}{4} LAI \times r_a^s(\alpha) + \frac{1}{4}(4 - LAI) \times r_a^s(0) \tag{2.16}$$

when LAI ≥ 4

$$r_a^a = r_a^a(\alpha) \tag{2.17}$$

$$r_a^s = r_a^s(\alpha) \tag{2.18}$$

where α and 0 in the bracket indicate full vegetation cover and bare soil, respectively.

Above the fully developed canopy, where the wind speed profile is logarithmic, the aerodynamic resistance $r_a^a(\alpha)$ is calculated using Eq. (2.2). For aerodynamic resistance within the canopy, $r_a^s(\alpha)$ is obtained by performing an integration of eddy diffusion coefficient (K) over the height from 0 to $d + Z_{\text{om}}$, i.e.,

$$r_a^s(\alpha) = \int_0^{d+z_{om}} \frac{dz}{K(z)} = \frac{\ln \frac{z-d}{z_{om}} + \varphi_{\text{M}}}{k^2 u(z)} \frac{h}{n(h-d)} \{\exp\, n - \exp[n(1 - \frac{d + z_{\text{m}}}{h})]\} \tag{2.19}$$

where n is the extinction coefficient of the eddy diffusion, which is estimated by linear interpolation between the value for $h < 1$ m (=2.5) and $h > 10$ m (=4.25); u(z) is the wind speed at height z. The eddy diffusion coefficient K(z) is determined by

$$K(z) = \frac{k^2(h-d)u(z)}{[\ln(z-d)/z_{om}]} \exp[-n(1 - z/h)] \tag{2.20}$$

For surface without canopy, $r_a^a(0)$ and $r_a^s(0)$ are estimated from the following equations without the consideration of the zero plane displacement height,

$$r_a^s(0) = \frac{(\ln \frac{h}{z_{om}'} + \varphi_{\text{M}})(\ln \frac{h}{z_{oh}'} + \varphi_{\text{H}})}{k^2 u(h)} \tag{2.21}$$

$$r_a^a(0) = \frac{(\ln \frac{z_m}{z_{om}'} + \varphi_{\text{M}})(\ln \frac{z_h}{z_{oh}'} + \varphi_{\text{H}})}{k^2 u(z_m)} - r_a^s(0) \tag{2.22}$$

where z_{om}' and z_{oh}' are the roughness length of bare surface governing momentum transfer and heat and vapor transfer (=0.01 m), respectively; $u(h)$ is the wind speed at canopy height h

$$u(h) = \frac{\ln[(h-d)z_{om}]}{[\ln(z_m - d)/z_{om}]} u(z_{\text{m}})] \tag{2.23}$$

The intra-canopy aerodynamic resistance r_a^c is calculated from Choudhury and Monteith (1988),

Table 2.1 Different vegetation cover conditions considered in this study (Yang and Shang 2012)

Cases	Description
A (full vegetation)	Assuming a full vegetation cover with F_r = 100 %, surface leaf area index (LAI)[a] varies between 0.5 and 5, vegetation height of 5 m and minimum canopy resistance (r_{sc_min})[b] of 170 s m^{-1}
B (partial, uniform vegetation)	Assuming a leaf area index for simple plant (L_c)[c] of 2, F_r varies from 10 to 100 %. Other vegetation parameters are the same as case A
C (partial, non-uniform vegetation)	Assuming a constant surface leaf area index, the degree of vegetation non-uniformity is reflected through varying vegetation cover (LAI = $L_c \times F_r$). The lower the F_c is, the higher the vegetation non-uniformity is. Other vegetation parameters are the same as case A

[a]LAI of 0.5–5 represents LAI values over most fully vegetated surfaces
[b]r_{ST_min} = 170 s m^{-1} represents an average r_{ST_min} of typical ecosystems [Grassland, r_{ST_min} = 130 s m^{-1} ; forest, r_{ST_min} = 180 s m^{-1} ; shrubland, r_{ST_min} = 210 s m^{-1} (Korner 1994)]
[c]Single plant leaf area index (L_c) ranges typically from 0.5 to 5 for most species. In this study, a midway of 2 was chosen

$$r_a^c = \frac{n}{0.02}\sqrt{\frac{l_w}{u(h)}\frac{1}{1-e^{-n/2}}} \tag{2.24}$$

where l_w is the characteristic length of leaf width (m) (Table 2.1).

The canopy surface resistance in the S-W model (r_s^c) is similar with the bulk surface resistance in P-M model (r_c). Thus, r_s^c can be computed from Eqs. (2.3) and (2.4). The soil surface resistance is computed using an empirical equation given by Lin and Sun (1983),

$$r_s^s = 3.5(\theta_s/\theta_1)^{2.3} + 33.5 \tag{2.25}$$

where θ_1 is the soil water content within the surface soil layer.

2.2.3 Two-Patch Model

In the two-patch (T-P) model (Fig. 2.1c), both soil and vegetation components are assumed to receive full radiation loading, and the total flux of latent heat per unit area is calculated as the mean of fluxes from each component (canopy or soil) weighted by their relative areas (Lhomme and Chehbouni 1999),

$$\lambda \mathrm{ET_a} = Fr \times \lambda T + (1 - Fr) \times \lambda E \tag{2.26}$$

$$\lambda T = \frac{\Delta A + \rho C_p D/(r_a^a + r_a^c)}{\Delta + \gamma[1 + r_s^c/(r_a^a + r_a^c)]} \tag{2.27}$$

$$\lambda E = \frac{\Delta A + \rho C_p D/(r_a^a + r_a^s)}{\Delta + \gamma[1 + r_s^s/(r_a^a + r_a^s)]} \tag{2.28}$$

where Fr is the fractional vegetation coverage. The value of Fr can be either determined by in situ measurements or estimated from remote sensing images (Table 2.1), in which Fr is calculated from Mu et al. (2011),

$$Fr = (\mathrm{EVI} - \mathrm{EVI}_{\min})/(\mathrm{EVI}_{\max} - \mathrm{EVI}_{\min}) \tag{2.29}$$

where EVI is the enhanced vegetation index (Huete et al. 2002); $\mathrm{EVI}_{\max}$ and $\mathrm{EVI}_{\min}$ are the maximum and minimum EVI values, respectively (Mu et al. 2007).

Aerodynamic resistances in the T-P model are similar with those in the S-W model. However, when calculating λE and λT, the T-P model assumes that transpiration occurs from a closed canopy surface while evaporation happens over bare soil. As a result, aerodynamic resistances r_a^a and r_a^c in Eq. (2.27) are estimated by Eqs. (2.2) and (2.23), while those in Eq. (2.28) are computed from Eqs. (2.21) and (2.22), respectively.

Lhomme and Chehbouni (1999) suggested that for patchy or clumped vegetation, it is better to use the clumped leaf area index (L_c), which is defined as the LAI per unit vegetated area ($L_c = \mathrm{LAI}/F_r$). Therefore, the bulk canopy surface resistance r_s^c is estimated from

$$r_s^c = \frac{1}{2L_c} \frac{r_{ST\_\min}}{f_1 f_2 f_3 f_4} \tag{2.30}$$

where r_{ST_min}, f_1, f_2, f_3, and f_4 keep the same meanings as those in P-M and S-W model.

Soil surface resistance of the T-P model is calculated from Eq. (2.25).

2.2.4 TVET Model

By coupling the layer and patch models, Guan and Wilson (2009) developed a hybrid dual source model for estimating potential evaporation (PE) and potential transpiration (PT) partitioning (i.e., the TVET model). The TVET model adopts the layer approach to allocate available energy between canopy and soil (Eq. 2.14) and to calculate aerodynamic resistances, and uses the patch approach to partition energy into latent heat (E or T), sensible heat (H), and ground heat flux (G). The model structure is given in Fig. 2.1d, and the equations is given below,

$$\lambda PE = \frac{\Delta A_s + (1 - F_r)\frac{\rho_a C_p D}{r_a^a + r_a^s}}{\Delta + \gamma} \tag{2.31}$$

$$\lambda PT = \frac{\Delta A_c + F_r \frac{\rho_a C_p D}{r_a^a + r_a^c}}{\Delta + \gamma(1 + \frac{r_s^c}{r_a^a + r_a^c})} \tag{2.32}$$

where A_s and A_c are available energy for soil and canopy, which can be estimated from Eqs. (2.16) and (2.17), respectively.

The TVET model estimates aerodynamic resistances following the same way as the S-W model, and calculates surface resistances as that of the T-P model.

2.3 Comparison Setups

Single source model treats the land surface as uniform layer so that it cannot distinguish evaporation from transpiration. In addition, studies have shown that single source model does not suitable for ET estimation over partially vegetated surfaces, on which dual source model performs generally better. In this section, the three dual source ET models will be compared and evaluated in estimating potential ET and its partitioning over surfaces with different hypothesized vegetation cover conditions (Table 2.1).

When evaporating surface is not water-limited, the soil surface resistance is considered to be negligible (Shuttleworth and Wallace 1985) and the canopy surface resistance equals to the minimum canopy resistance. The meteorological data is taken from the Linhe Station in the Inner Mongolia during the main growing season of 2006 (April–October). The site is characterized with a dry and cold climate, with a mean annual temperature of 6.8 °C and mean annual precipitation of 139 mm.

2.4 Results and Discussion

2.4.1 Surfaces with Full Vegetation Cover (Case A)

Previous studies have shown that the P-M model performs well in estimating potential evapotranspiration (PET) over fully vegetated surface (e.g., Allen et al. 1998). Thus, PET estimates from the P-M model are considered as reference to evaluate the performance of the other three dual source models. Results show that the T-P model performed exactly the same as the P-M model (Fig. 2.2). This is because that the T-P model shares the same formulation of the P-M model when F_c equals 1. TVET model also gives similar results as the P-M model, except for a slightly overestimation of PET by TVET in low LAI end (Fig. 2.2). In comparison, the S-W model seriously overestimated PET and the difference increases with the decrease of LAI (Fig. 2.3). Taking LAI = 2 as an example, Fig. 2.3 compares PET

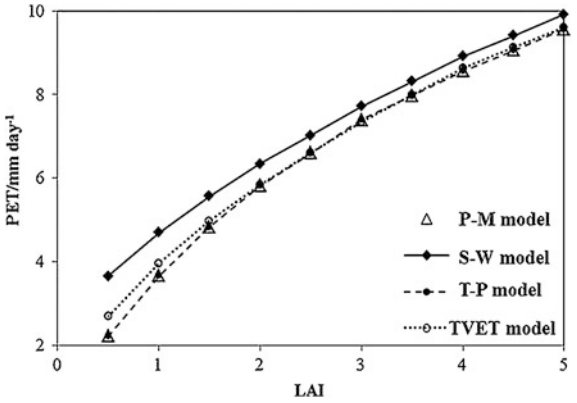

Fig. 2.2 Relationship between LAI and estimated PET by different model over fully vegetated surfaces (Yang and Shang 2012)

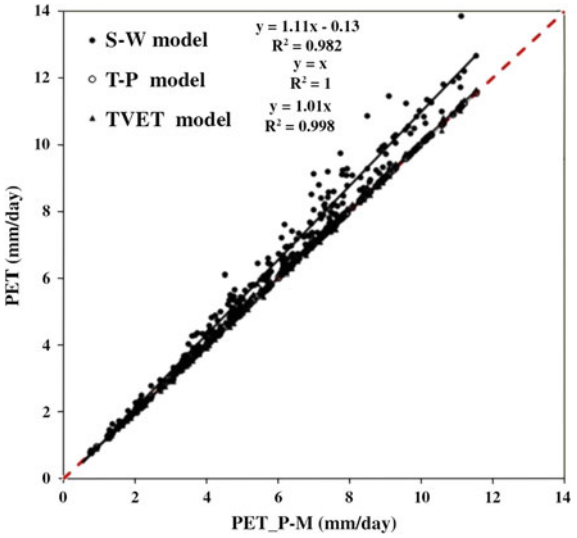

Fig. 2.3 Comparison between PET from P-M model and those from the three dual source models over fully vegetated surfaces with a fixed LAI = 2 (Yang and Shang 2012)

estimated from the P-M model with that from the three dual source models. It shows that PET from TVET agrees very well with that from P-M (R^2 = 0.998) whereas the difference between S-W PET and P-M PET appears to be relatively large (R^2 = 0.982).

Further analysis on the results of PE and PT partitioning shows that PT from the S-W model agrees well with that from the TVET model, whereas the S-W PE is consistently higher than the TVET PE. This phenomenon suggests the overestimation of PET by the S-W model is very likely due to its overestimation in potential evaporation (Fig. 2.4). Shuttleworth and Wallace (1985) reported that when soil surface resistance is large enough, E and T can be considered as two separate processes such that the S-W model can be simplified to be the P-M model. However, such extreme large soil surface resistance rarely occurs in realities,

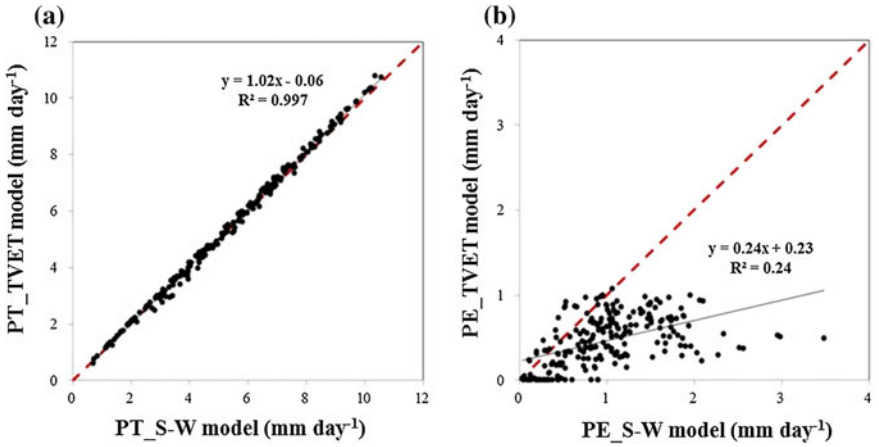

Fig. 2.4 Comparison of PT (**a**) and PE (**b**) estimated from the S-W and TVET model under full vegetation cover condition (LAI = 2) (Yang and Shang 2012)

particularly when the soil surface resistance is taken to be zero for potential ET estimation in this study. As a result, the S-W model appears to overestimate PE and therefore PET under low LAI condition. For the T-P model, soil evaporation is neglected under fully vegetated surfaces, which also obviously deviates from real conditions. Compared with the S-W and T-P model, the TVET model performed generally better in estimating PET and the partitioning of PE and PT under full vegetation cover conditions.

2.4.2 *Surfaces with Uniform and Partial Vegetation Cover (Case B)*

The relationship between F_c and PET estimated from the three dual source models is shown in Fig. 2.5. It shows that PET from the S-W model is obviously higher than that from the other two models, and the difference shows an increasing trend with the increase of F_r. Similar with Case A, the overestimation of PET by S-W model is due to its overestimation in PE (Fig. 2.6). The S-W model treats the soil surface equally over the whole area and does not distinguish soil evaporation under and between vegetation canopies, resulting in an increased error in PE estimates as F_r increased. Combining the fact that the overestimation of PET by S-W model increases with the decrease of LAI (higher PE/PET ratio) (Fig. 2.2), the results suggest that PE from the S-W model are more likely close to that from inter-canopy soil surfaces.

In contrast to the S-W model, the T-P model neglect evaporation from under-canopy surfaces, resulting in lower PE estimates as F_r increased (Fig. 2.6). In comparison, PE from the TVET model lies between that from the S-W model

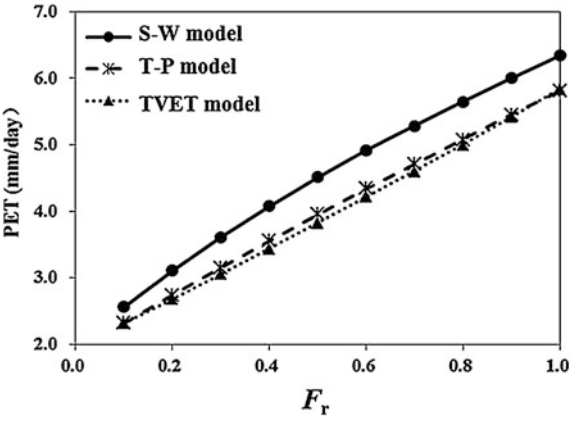

Fig. 2.5 Relationship between F_r and PET estimated from the three dual source models (Yang and Shang 2012)

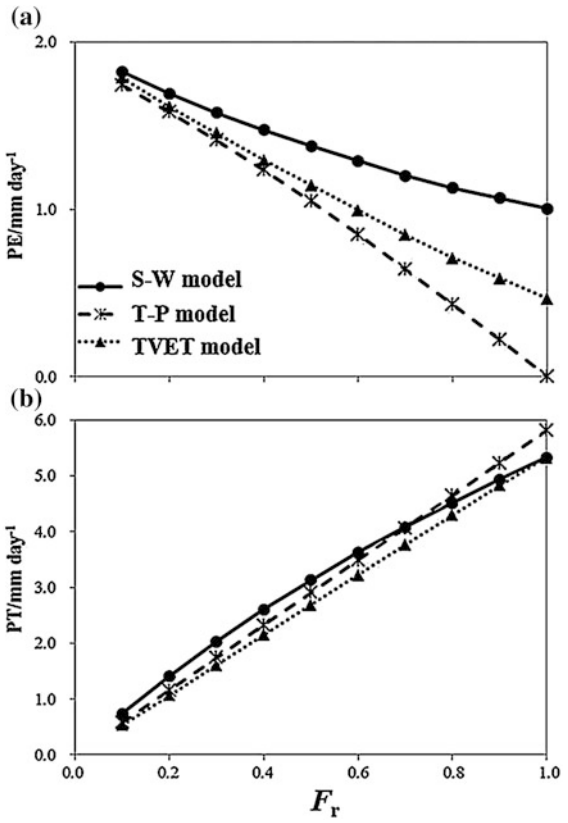

Fig. 2.6 Relationship between F_r and PE (**a**) and between F_r and PT (**b**) estimated from the three dual source models (Yang and Shang 2012)

(overestimated) and the T-P model (underestimated), implying that the results from the TVET model may be more reasonable.

2.4.3 Surfaces with Non-uniform and Partial Vegetation Cover (Case C)

When surface leaf area index (LAI) is fixed, the non-uniformity of vegetation distribution can be reflected by varying fractional vegetation cover (F_r). Our results show that S-W PT does not vary with the changes on F_r, demonstrating that the S-W model may not applicable over surfaces with partial and patch vegetation. In addition, PE from the S-W model does not decrease with the increase of F_r. On the contrary, it shows a slightly increasing trend as F_r increased. This is because the increase in Fc would lead to a lower surface albedo and therefore higher available energy for evapotranspiration (surface albedo is a function of F_r).

For the TVET model, its PT/PE increases/decreases with the increase of F_r, suggesting that the TVET model is able to capture surface characteristics over a wide range of vegetation cover conditions. For higher F_r (close to 100 %), results in Case A have already shown a good performance of the TVET model; for lower F_r (e.g., 20 %), the TVET PE is very close to that of the S-W model, whereas the TVET PT is significantly lower than that of the S-W model, indicating that the TEVT model may depict the reality better than the S-W model.

The relationship between F_r and PE/PT from the T-P model is very similar with that of the TVET model (Fig. 2.7). Lhomme and Chehbouni (1999) reported that the T-P model is more suitable for surfaces with low and patchy vegetation cover. Similar finding was also reported in Blyth and Harding (1995), who found a good performance of the T-P model over a surface with a ratio of vegetation height to patch size larger than 0.1. Our results in Fig. 2.7 show that the estimated PE from the T-P model agrees well with that from the TEVT model under low LAI conditions. However, when LAI is high, the T-P PE decreases towards zero with the increase of F_r. Similar with Casa B, this is because the T-P model does not account for soil evaporation from under-canopy surfaces, which results in an increased underestimation of PE as F_r increased by the T-P model. Moreover, for fixed F_r, PE from the T-P model does not vary with changes in LAI. This is due to the ignorance of radiation interception by vegetation canopy in the T-P model. On the other hand, it assumes that each component (or patch) receives the same radiation load (i.e., full radiation). In such a case, the amount of radiation received by soil surface is only determined by fractional vegetation cover but not related with leaf size and density (as reflected through LAI).

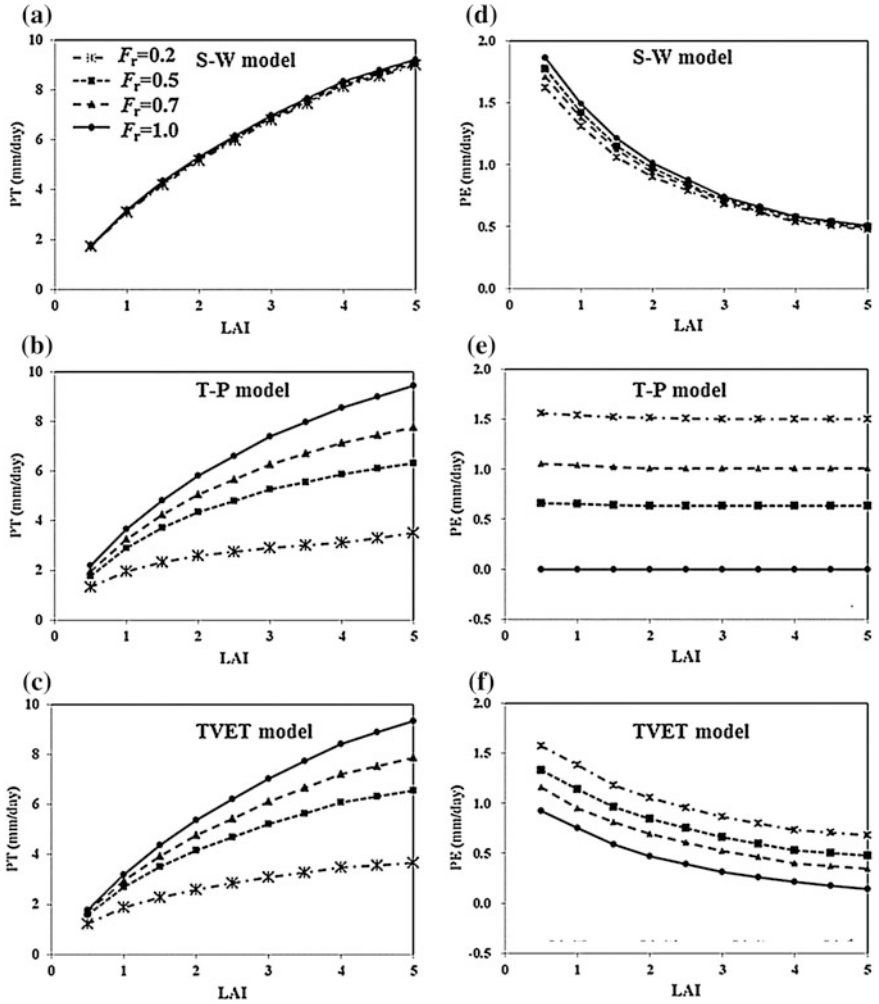

Fig. 2.7 Variations in PT and PE estimated from the three dual source models with those in LAI and F_r (Yang and Shang 2012)

2.5 Conclusion

Potential evapotranspiration depends greatly on local climate and vegetation distribution conditions, and is important in studying the cropland and basin hydrological circles. The chapter provides a detailed comparison of the performances among three dual-source evapotranspiration models, including the S-W model (layer approach), the T-P model (patch approach) and the TVET model (hybrid approach), in estimating and partitioning potential evaporation and potential

transpiration under different hypothetical vegetation distribution conditions. The S-W model ignores the difference of energy fluxes between under- and inter-canopy soil; while the T-P approach assumes a full radiation loading for both the canopy and inter-canopy soil and ignores the evaporation from under-canopy soil surfaces. The TVET model is a combination of the layer and patch models, and adopts the layer approach to partition available energy between canopy and soil and uses the patch approach to calculate energy fluxes. As a result, both under- and inter-canopy soil evaporation were estimated and distinguished in the TVET model. In simulation scenarios, the height of vegetation was assumed to be 5 m with canopy leaf area index of 2 and minimum stomatal resistance of 170 s/m. The bulk surface leaf area index (LAI) varied from 0.5 to 5, and fractional vegetation coverage (F_c) varied from 10 to 100 %. The vegetation clumpy patterns were quantified by fixing LAI while varying F_c. The climate data was obtained from the Linhe meteorological station located in an arid region in central Inner Mongolia of North China. The results indicated that both the patch and hybrid model performed reasonably well in estimating potential evapotranspiration under homogeneous vegetation distribution conditions. However, the S-W model tended to overestimate potential evapotranspiration, as it generally gave higher potential evaporation estimates. The overestimation in potential evapotranspiration by the S-W model was increased with the increase of F_r and the decrease of LAI. In contrast, the T-P model had a tendency to underestimate potential evaporation, especially with high F_c and low LAI. For heterogeneous vegetation distribution conditions, potential evapotranspiration estimated from the S-W model was generally higher than that given by the T-P and TVET model, particularly with low F_r. Potential evaporation (potential transpiration) from the S-W model increases (decreases) with the increase of LAI. However, both variables from the S-W model did not change with changes of F_r. In contrast, potential transpiration estimated from the T-P and TVET model was increased with the increase of both LAI and F_r. Potential evaporation from the T-P model was increased with the increase of F_r, but kept relative constant under various LAI conditions, while potential evaporation from the TVET model was increased with the decrease of both F_c and LAI. The above results suggest that the S-W model may give reasonable potential transpiration estimates over homogeneous vegetated surfaces, while the T-P model is more suitable for surfaces with lower fractional and clumped vegetation cover. By contrast, the TVET model performs better than both the S-W model and the T-P model, which can be used to estimate potential evaporation and potential transpiration partitioning for a wide range of surfaces with different vegetation distribution patterns.

References

Allen RG, Pereira LS, Raes D et al (1998) Crop evapotranspiration: guidelines for computing crop water requirements. Rome

Blyth EM, Harding RJ (1995) Application of aggregation models to surface heat flux from the Sahelian tiger bush. Agric For Meteorol 72:213–235

Brutsaert W (1982) Evaporation into the atmosphere: theory, history and applications. D. Reidel Publishing Company, Dordrecht

Campbell GS, Norman JM (1998) An introduction to environmental biophysics. Springer, New York

Choudhury BJ, Monteith JL (1988) A four-layer model for the heatbudget of homogeneous land surfaces. Q J R Meteorol Soc 114:373–398

Guan H, Wilson JL (2009) A hybrid dual-source model for potential evaporation and transpiration partitioning. J Hydrol 377:405–416

Huete A, Didan K, Miura T et al (2002) Overview of the radiometric and biophysical performance of the MODIS vegetation indices. Remote Sens Environ 83:195–213

Jarvis PG (1976) Interpretation of variations in leaf water potential and stomatal conductance found in canopies in field. Philos Trans R Soc Lond B 273:593–610

Korner C (1994) Leaf diffusive conductances in the major vegetation types of the globe. In: Schulze ED, Caldwell MM (eds) Ecophysiology of photosynthesis. Springer, New York

Lhomme JP, Chehbouni A (1999) Comments on dual-source vegetation-atmosphere transfer models. Agric For Meteorol 1999:269–273

Lhomme J, Monteny B, Amadou M (1994) Estimating sensible heat flux from radiometric temperature over sparse millet. Agric For Meteorol 33:1495–1508

Lin JD, Sun SF (1983) A study of moisture and heat transport in soil and the effect of resistance to evaporation. J Hydraul Eng 14:1–8 (in Chinese)

Monsi M, Saeki T (1953) Uber den lichtfaktor in den pflanzengesellschaften und seine bedeutung fur die stoffproducktion. Jpn J Bot 14:22–52

Mu Q, Heinsch FA, Zhao M et al (2007) Development of a global evapotranspiration algorithm based on MODIS and global meteorology data. Remote Sens Environ 111:519–536

Mu Q, Zhao M, Running SW (2011) Improvements to a MODIS global terrestrial evapotranspiration algorithm. Remote Sens Environ 115:1781–1800

Noilhan J, Planton S (1989) A simple parameterization of land surface processes for meteorological models. Mon Weather Rev 117:536–549

Shuttleworth WJ, Wallace JS (1985) Evaporation from sparse crops-an energy combination theory. Q J R Meteorol Soc 111:839–855

Yang YT, Shang SH (2012) Comparison of dual-source evapotranspiration models in estimating potential evaporation and transpiration. Trans CSAE 28:85–91 (In Chinese)

Yu H, Liu T, Yang Y et al (2014) A hybrid dual-source model of estimating evapotranspiration over different ecosystems and implications for satellite-based approaches. Remote Sens 6:8359–8386

Chapter 3
A Hybrid Dual-Source Model of Estimating Evapotranspiration over Different Ecosystems

3.1 Introduction

In Chap. 2, we compared three dual source models in estimating potential ET and its partitioning under different vegetation cover conditions. The results show that the hybrid model (i.e., the TVET model) may be more suitable than the layer and patch model for a broad range of vegetated surfaces. However, the TVET model by Guan and Wilson (2009) was initially proposed to partition PE and PT for hydrologic modelling; it does not consider environmental stresses (e.g., soil moisture) on actual ET. Numerous studies have shown that soil moisture is the prominent controlling factor of actual ET processes in arid and semiarid regions; limited soil moisture is responsible largely for the recent decline in global land surface evapotranspiration (Jung et al. 2010; Seneviratne et al. 2010). The TVET model is not able to simulate actual E and T processes. Furthermore, soil moisture conditions could also affect applicability of ET models. Existing studies have indicated that the P-M model with variable canopy resistance can be directly applied to estimate ET over sparsely vegetated canopies under different soil moisture conditions (Ortega-Farias et al. 2004, 2010). Massman (1992) suggested that the layer and patch approaches can be interchangeably used under the extremely arid environment, as the surface resistance becomes a prominent factor of ET whereas the interactions between components are relatively small.

The objectives of this study were therefore to (1) develop a hybrid dual-source (H-D) model to estimate ET processes over four different ecosystems, including deciduous broadleaf forest, woody savannas, grassland, and cropland, by combining canopy and soil surface resistances with the original H-D model developed by Guan and Wilson (2009); (2) evaluate ET estimates from the developed H-D model with eddy covariance measurements and compare with those from three other ET

Y. Yang, *Evapotranspiration Over Heterogeneous Vegetated Surfaces*,
Springer Theses, DOI 10.1007/978-3-662-46173-0_3

models (the P-M model, the S-W model, and the two-patch (T-P) model). Because surface conditions (both the vegetation and soil moisture) are the primary factors that determine applicability of different ET models, it is of great value to compare different ET models under varying surface conditions.

3.2 Model Development

The H-D model is a mixture of the layer approach and the patch approach (Fig. 2.1d). It adopts the layer approach to allocate available energy between canopy and soil (Eqs. 2.13 and 2.14), and to calculate aerodynamic resistances, and uses the patch approach to partition energy into latent heat (E or T), sensible heat (H), and ground heat flux (G). The energy balance equations are,

$$A_c = Fr \times (\lambda T + H_c) \tag{3.1}$$

$$A_s = (1 - Fr) \times (\lambda E + H_s) \tag{3.2}$$

For each component, fluxes of sensible and latent heat are calculated following the classical Ohm's law type formulations. To account for environmental stresses on ET, the canopy and soil surface resistances were incorporated into the original hybrid dual-source potential ET model of Guan and Wilson (2009),

$$H_c = \rho C_p \frac{(t_v - t_{zh})}{r_a^c + r_a^a} \tag{3.3}$$

$$H_s = \rho C_p \frac{(t_s - t_{zh})}{r_a^s + r_a^a} \tag{3.4}$$

$$\lambda T = \frac{\rho C_p}{\gamma} \frac{e_v - e_{zh}}{r_a^c + r_a^a + r_s^c} \tag{3.5}$$

$$\lambda E = \frac{\rho C_p}{\gamma} \frac{e_s - e_{zh}}{r_a^s + r_a^a + r_s^s} \tag{3.6}$$

where t and e are the air temperature and humidity, respectively. Subscript v represents the bulk leaf stomata and zh is the reference height where temperature and humidity are measured.

Assuming that vapor within the leaf stomata is always saturated under t_v, Eq. (3.5) can be rewritten as

$$\lambda T = \frac{\rho C_p}{\gamma} \frac{e_{sat}(t_v) - e_{zh}}{r_a^c + r_a^a + r_s^c} \tag{3.7}$$

The term e_s in Eq. (3.6) represents the equilibrium vapor pressure within the surface layer of soil, and can be calculated by the thermal equilibrium equation (Edlefson and Anderson 1943). As a result, Eq. (3.6) is rewritten as

$$\lambda E = \frac{\rho C_p}{\gamma} \frac{h_u e_{sat}(t_s) - e_{zh}}{r_a^s + r_a^a + r_s^s} \tag{3.8}$$

where parameter h_u is the relative humidity within the surface soil, and is estimated based on the assumption that water in the liquid and vapor phases are in local thermodynamic equilibrium (Edlefson and Anderson 1943)

$$h_u = \exp\left(\frac{g h_s}{R t_s}\right) \tag{3.9}$$

where R is the gas constant for water vapor (=461.5 J/(Kg K)); g is the gravitational acceleration (=9.8 m/s^2); h_s and t_s are the water potential (m) and temperature (K) of the surface soil, respectively.

The Penman linear relationship (Penman 1948) is employed to convert saturated vapor pressure at the reference height to that on the surface

$$e_{sat}(t_v) = e_{sat}(t_{zh}) + \Delta(t_v - t_{zh}) \tag{3.10}$$

$$e_{sat}(t_s) = e_{sat}(t_{zh}) + \Delta(t_s - t_{zh}) \tag{3.11}$$

Substituting Eqs. (3.1), (3.3), (3.7) and (3.10), and convert fluxes into the total surface area, the canopy transpiration is calculated as

$$\lambda T = \frac{\Delta A_c + Fr \frac{\rho C_p [e_{sat}(t_{zh}) - e_{zh}]}{r_a^a + r_a^c}}{\Delta + \gamma\left(1 + \frac{r_s^c}{r_a^a + r_a^c}\right)} \tag{3.12}$$

Similarly, substituting Eqs. (3.2), (3.4), (3.8) and (3.11), one can get the expression for estimating soil evaporation,

$$\lambda E = \frac{h_u \Delta A_s + (1 - Fr) \frac{\rho C_p [h_u e_{sat}(t_{zh}) - e_{zh}]}{r_a^a + r_a^s}}{\Delta h_u + \gamma\left(1 + \frac{r_s^s}{r_a^a + r_a^s}\right)} \tag{3.13}$$

Aerodynamic resistances (r_a^a, r_a^c and r_a^s) and soil surface resistance of the H-D model are calculated using the same equations as those of the S-W model. However, since the H-D model was originally proposed to estimate latent heat flux from non-uniform vegetation, the clumped leaf area index is used in the H-D model to upscale stomatal resistance into bulk canopy surface resistance (r_s^c), as given in Eq. (2.30).

3.3 Data and Model Evaluation Criteria

3.3.1 Study Site and Data

Four sites within the AmeriFlux network were used in this study to validate the model performance, including one deciduous broadleaf forest site (Morgan Monroe State Forest, US_MMS) (Oliphant et al. 2011), one woody savannas site (Flagstaff Managed Forest, US_Fmf) (Sullivan et al. 2008), one grassland site (Vaira Ranch, US_Var) (Ryu et al. 2008), and one cropland site (Bondville, US_Bo1) (Meyers and Hollinger 2004). For each site, continuous records of half-hourly meteorological and latent heat flux measurements from eddy covariance (EC) towers were obtained from the AmeriFlux Web site (http://ameriflux.ornl.gov/). Ancillary and biological data include soil moisture and temperature, leaf area index (LAI) and vegetation height (h) were also acquired. A summary of the sites including locations, climate conditions, vegetation types, vegetation and soil parameters as well as study periods is listed in Table 3.1 and soil moisture conditions during the study period for each site are shown in Fig. 3.1.

Moderate Resolution Imaging Spectroradiometer (MODIS) images were used to estimate the EVI and then to calculate Fr (Eq. 2.29) for each site due to the lack of in situ Fr observations. EVI was calculated following the method given by Huete et al. (2002) using MODIS surface reflectance dataset (MOD09GA) downloaded from the NASA Data Center (http://reverb.echo.nasa.gov/). The original MODIS images in the sinusoidal projection were re-projected into the UTM projection and resampled into 1 km spatial resolution. For days without measurements, the values of LAI, h and Fr were estimated by linearly interpolating those parameters between the two bounding observations.

It is worthwhile to mention that although EC measurements have been widely considered as the ground truth of energy and water exchanges between the land surface and the atmosphere, studies have shown that ET from EC system suffers from uncertainties to a certain degree, i.e., the energy balance closure of EC system generally lies between 80 and 95 % (Wilson et al. 2002). In addition, linear interpolation of vegetation parameters during days without in situ measurements would also result in uncertainties. In this study, the EC-observed ET at the four sites was obtained from the level-4 AmeriFlux dataset, in which rigorous quality control procedures were made to guaranty the accuracy of EC observations. Thus, ET from the EC system was regarded as ground truth of actual evapotranspiration to validate the four models in the following analysis.

Table 3.1 General information of sites and selected model parameters used in this study (Yu et al. 2014)

Sites	Location[a]	Climate[b]	Vegetation	Vegetation[c] and soil[d] parameters	Study period	References
US_MMS	W86.4131°	P = 1,094 mm	Deciduous	H = 27 m, LAI = 0.84–4.72, Fr = 0.67–0.73, r_{ST_min} = 180 s/m, l_w = 0.15 m, θ_F = 0.39, θ_W = 0.21	8 February 2003 to 13 November 2003	Oliphant et al. (2011)
	N39.3232°	T = 10.8 °C	Broad-leaf			
	a.s.l. 275 m		Forest			
US_Fmf	W111.7273°	P = 613 mm	Woody	h = 18 m, LAI = 1.5, Fr = 0.3, r_{ST_min} = 180 s/m, l_w = 0.02 m, θ_F = 0.41, θ_W = 0.086	1 February 2006 to 10 September 2006	Sullivan et al. (2008)
	N35.1426°	T = 11.4 °C	Savannas			
	a.s.l. 2160 m					
US_Var	W120.9507°	P = 565 mm	Grasslands	h = 0.2–0.55 m, LAI = 0.18–1.4, Fr = 1, r_{ST_min} = 130 s/m, l_w = 0.03 m, θ_F = 0.28, θ_W = 0.07	10 January 2006 to 27 May 2006	Ryu et al. (2008)
	N38.4067°	T = 16.9 °C				
	a.s.l. 129 m					
US_Bo1	W88.2904°	P = 756 mm	Croplands (maize)	h = 0.22–2.32 m, LAI = 0.18–4.38, Fr = 0.1–0.9, r_{ST_min} = 130 s/m, l_w = 0.03 m, θ_F = 0.33, θ_F = 0.1	24 May 2001 to 10 September 2001	Meyers and Hollinger (2004)
	N40.0062°	T = 11.4 °C				
	a.s.l. 219 m					

[a]Description of the location for sites include longitude (W/E), latitude (N/S) and elevation above sea level (a.s.l.)

[b]Description of climate condition for sites include annual average precipitation (P) and annual average air temperature (T). For US_MMS, P and T are averaged between 1971 and 2000; for US_Fmf, P and T are averaged between 2006 and 2010; for US_Var, P and T are averaged between 1946 and 2005; for US_Bo1, P is averaged between 1997 and 2006 and T is averaged between 1997 and 2007

[c]The value of Fr in the grassland site was assumed to be 100 % during the main growing season (we found that Eq. (2.29) is not applicable in grassland), which accords well with field survey, and the value of Fr for the forest and cropland sites were estimated from Eq. (2.29). For the woody savannas site, the estimated values of Fr from Eq. (2.29) were ranged from 0.26 to 0.29. However, according to the definition in the IGBP vegetation classification, the Fr of woody savannas should be between 0.3 and 0.6. As a result, a lower boundary of 0.3 was chosen for the woody savannas site

[d]In this study, θ_F was assumed to be the water content retained in the soil at −0.02 MPa of suction pressure, which is midway of most reported θ_F values (−0.01 to −0.033 MPa) (Haise et al. 1955). θ_W was related to the suction pressure at −1.5 MPa. The VG-M model (Mualem 1976; van Genuchten 1980) was adopted to describe the soil water retention curve, and the parameters of the VG-M model for each site were estimated from measured soil texture and bulk density using the method given by Schaap et al. (1998)

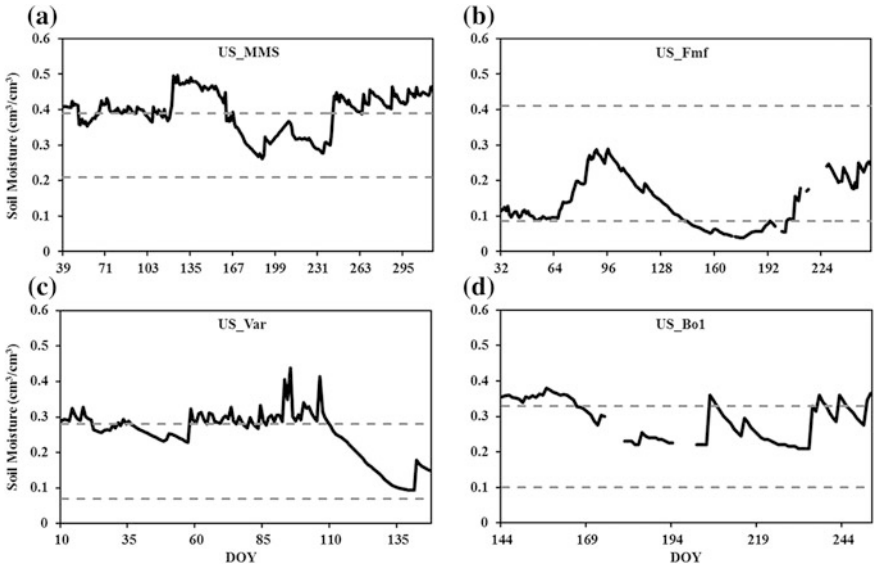

Fig. 3.1 Soil moisture time series at four sites examined in this study. **a** US_MMS; **b** US_Fmf; **c** US_Var; and **d** US_Bo1. The *upper dashed line* indicates field capacity and the *lower dashed line* indicates the wilting point (Yu et al. 2014)

3.3.2 Evaluation of Model Performance

Three statistic metrics recommend by Legates and McCabe (1999) were used to evaluate the model performance, including the mean absolute error (MAE), the modified coefficient of efficiency (E_1), and the modified index of agreement (d_1):

$$\mathrm{MAE} = N^{-1}\sum_{i=1}^{N}|O_i - S_i| \tag{3.14}$$

$$E_1 = 1.0 - \frac{\sum_{i=1}^{N}|O_i - S_i|}{\sum_{i=1}^{N}|O_i - \bar{O}|} \tag{3.15}$$

$$d_1 = 1.0 - \frac{\sum_{i=1}^{N}|O_i - S_i|}{\sum_{i=1}^{N}(|O_i - \bar{O}| + |S_i - \bar{O}|)} \tag{3.16}$$

where O_i is the observed value, S_i is the modeled value, and $\bar{o}$ is the mean observed value. For a perfect model, MAE should be 0, and both E_1 and d_1 should be 1. A model performs better if MAE is smaller and E_1 and d_1 are lager.

In addition, the regressions of model estimated and observed ET with zero interception were also used to evaluate the model performance, i.e.,

$$\lambda \text{ET\_estimated} = \alpha \lambda \text{ET\_observed} \tag{3.17}$$

where λET_model and λET_observed are model-estimated and observed ET, respectively, and a is the slope of regression. If a model performs well, the a value should be close to 1.

3.4 Results and Discussion

3.4.1 Model Validation

Performance of the H-D model in simulating ET at a 30-min interval was firstly validated with observations from the eddy covariance system (Fig. 3.2a–d). Overall, the estimated ET agreed reasonably well with the ground-based measurements at all sites, with all fitted lines close to the 1:1 line. The MAE ranged from 16.3 to 38.6 W/m^2 (Table 3.2), indicating good performance of the H-D model in all ecosystems being tested. The highest MAE occurred at the woody savannas site (Flagstaff Managed Forest, US_Fmf), with E_1 and d_1 for this site being 0.56 and 0.77, respectively. The lowest MAE appeared at the grassland site (Vaira Ranch, US_Var), with E_1 of 0.72 and d_1 of 0.87. For the deciduous broadleaf forest site (Morgan Monroe State Forest, US_MMS), the MAE was 37.6 W/m^2, E_1 0.72, and d_1 0.87. The cropland site (Bondville, US_Bo1) had the highest agreement between the estimated and observed ET, with d_1 of 0.89 and E_1 of 0.79.

ET has evident diurnal patterns as a result of combined physical (e.g., temperature and radiation diurnal variations) and biological (e.g., stomatal closure) factors. Generally, the H-D model successfully reproduced these diurnal patterns of ET at all sites (Fig. 3.3). However, at the US_MMS and US_Fmf sites, the H-D model slightly underestimated ET in the morning and overestimated ET in the afternoon (Fig. 3.3a, b). This discrepancy is likely due to a simple canopy interception algorithm for net radiation used in the model (see Eq. 2.14), which is not able to reflect the diurnal variation in the sunlight incident direction. In the H-D model, LAI was used to partition net radiation between soil and canopy (Eq. 2.14). However, the LAI value used here only corresponds to that when the sun was directly overhead. As the solar incident angle varies with time, the shadow area and therefore the "effective" LAI values can vary during the daytime. As a result, the use of Eq. (2.14) would result in improper radiation partitioning especially when vegetation is tall [the mean vegetation height in US_MMS and US_Fmf are 27 and 18 m, respectively (Table 3.1)] and the canopy structure is non-uniform. For the

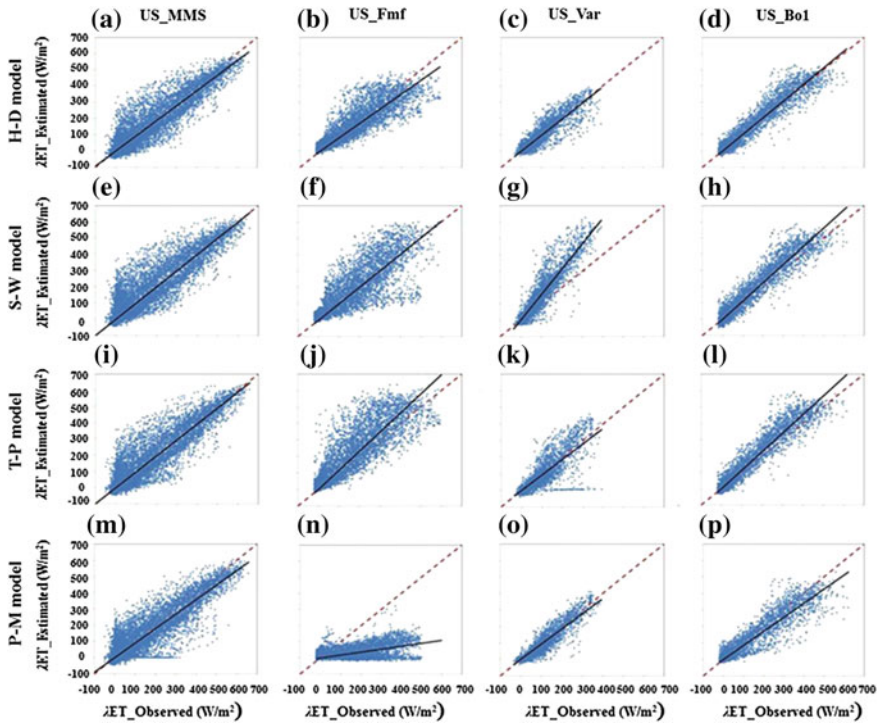

Fig. 3.2 Comparisons of actual evapotranspiration (W/m^2) estimates from four models to the eddy covariance measurements over a 30-min period in four different ecosystems. **a–d** The H-D model; **e–h** the S-W model; **i–l** the T-P model and **m–p** the P-M model (Yu et al. 2014)

remaining two sites, the H-D model slightly overestimated ET during the daytime (Fig. 3.3c, d). The overall good agreement between estimated and observed ET in different ecosystems indicates the potential of the H-D model to be applicable to a wide range of vegetated surfaces.

3.4.2 Comparison with Other Models

To further demonstrate the advantages of the H-D model, four models with distinct treatments on vegetation characterization were compared in Figs. 3.2 and 3.3 and Table 3.2. It is worthwhile to mention that the same set of parameters (as described in Table 3.1) was employed by the four models for each site; hence, disagreement among model performance is mainly caused by differences in model structures instead of different parameters. Interestingly, all statistics show that ET estimates from the H-D model show closer agreement with the measurements than those from three other models at all sites except for the P-M model at the US_Var site, where

Table 3.2 Statistic summary of the four models in estimating actual evapotranspiration over 30-min period at four sites

Sites	Models	$\bar{o}$ (W/m^2)	$\bar{s}$ (W/m^2)	MAE (W/m^2)	E_1	d_1	α
US_MMS	H-D	115.7	113.5	37.6	0.72	0.87	0.95
	S-W	115.7	134.7	48.4	0.62	0.81	0.99
	T-P	115.7	126.3	42.9	0.64	0.82	0.98
	P-M	115.7	119.2	45.7	0.63	0.82	0.90
US_Fmf	H-D	131.5	125.7	38.6	0.56	0.77	0.89
	S-W	131.5	142.2	51.4	0.41	0.71	0.99
	T-P	131.5	163.1	53.2	0.38	0.72	1.15
	P-M	131.5	37.4	99.5	−0.20	0.43	0.20
US_Var	H-D	53.6	50.9	16.3	0.72	0.87	0.98
	S-W	53.6	76.7	33.8	0.37	0.75	1.40
	T-P	53.6	44.7	24.4	0.58	0.81	0.92
	P-M	53.6	43.4	15.7	0.73	0.86	0.93
US_Bo1	H-D	117.5	123.6	30.0	0.79	0.89	1.02
	S-W	117.5	137.2	34.9	0.71	0.86	1.12
	T-P	117.5	137.4	34.8	0.74	0.87	1.13
	P-M	117.5	105.9	34.4	0.74	0.86	0.87

$\bar{s}$ is the mean estimated value (Yu et al. 2014)

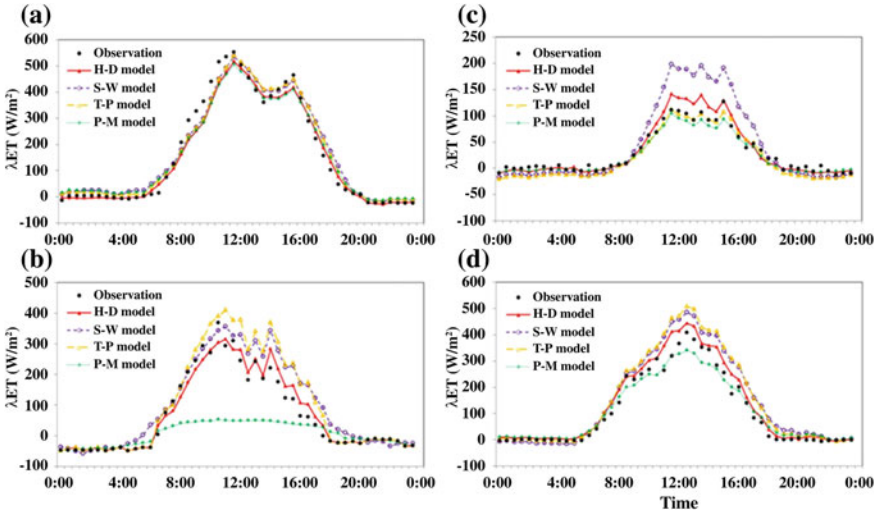

Fig. 3.3 Diurnal patterns of the estimated actual evapotranspiration from the four models and the measurements at **a** US_MMS; **b** US_Fmf; **c** US_Var; **d** US_Bo1. Each time series shown is the mean of three typical clear-sky days (Yu et al. 2014)

the value of E_1 of the P-M model was slightly higher than that of the H-D model (0.73 vs. 0.72) and the MAE of the P-M model was slightly lower than that of the H-D model (15.7 vs. 16.3 W/m^2) (Table 3.2). The S-W and T-P models had similar performance at the US_MMS, US_Fmf and US_Bo1 sites, but the S-W model significantly overestimated ET at the US_Var site (Fig. 3.2g). The P-M model showed the worst performance in estimating ET among the four models at the US_MMS and US_Fmf sites. However, it performed best at the US_Var site and better than the S-W model at the US_Bo1 site.

At the US_MMS site, the four models showed similar performance and corresponded well with measurements (Fig. 3.3a, e, i, m). The MAE ranged from 37.6 to 48.4 W/m^2 and the values of E_1 were all larger than 0.6 and d_1 were all larger than 0.8 (Table 3.2), indicating that all models appear to perform well at this site.

At the US_Fmf site, the P-M model severely underestimated ET_a with a slope of 0.20 and E_1 of −0.20, suggesting that the use of the P-M model to predict ET_a was even worse than using the mean value of the measurements (Fig. 3.2n and Table 3.2). This marked underestimation was mainly because of the low *F*r value at the site (around 0.3 during the study period), which failed to meet the assumption of "big leaf" in the P-M model. In addition, Stannard (1993) reported that the P-M model would underestimate ET when canopy surface resistance was much greater than soil surface resistance. During the study period, the average canopy surface resistance (r_s^c) was about 560 s/m, while the average soil surface resistance (r_s^s) was only 200 s/m at the US_Fmf site. Similar results can also be drawn from Fig. 3.3b, where the P-M model greatly underestimated ET during the daytime. The performance of the three dual-source models is much better than that of the P-M model (Figs. 3.2b, f, j, n and 3.3b and Table 3.2), which can be ascribed mostly to their ability to discriminate plant transpiration from soil evaporation. However, the T-P model overestimated ET by about 24 %, with E_1 of 0.38 and d_1 of 0.72, and the S-W model overestimated ET by 8 %, with E_1 of 0.41 and d_1 of 0.71 (Table 3.2). The low E_1 values of the T-P and S-W models suggest that both models do not seem to work at the woody savannas site.

For the grassland site (US_Var), where *F*r was high and the vegetation distribution was relatively uniform, the performance of the P-M model was largely improved compared with that at the US_Fmf site (Figs. 3.2c, g, k, o and 3.3c and Table 3.2). The statistics show that the P-M model performed even better than the three dual-source models at this site (Table 3.2). The S-W overestimated ET by about 43 % (the slope was 1.40), which is larger than results in published studies. Hu et al. (2009) reported that the S-W model generally overestimated ET by 8–15 % at four grassland sites of similar latitude as the US_Var site. The T-P model also provided acceptable results, with a MAE of 24.4 W/m^2, E_1 of 0.58, and d_1 of 0.81.

The cropland site (US_Bo1) showed the best correlations between estimates and observations (Table 3.2) for all four models. In the farmland ecosystem where the soil moisture remains at high levels (e.g., due to irrigation), the P-M model with various bulk surface resistances was found to be a good predictor for

evapotranspiration (Figs. 3.2p and 3.3d and Table 3.2). This phenomenon has also been reported by other studies (Ortega-Farias et al. 2004, 2010; Rana et al. 1997a, b). Figure 3.3d shows that the P-M model slightly underestimates ET during 10:00–14:00, with a MAE of 34.4 W/m^2, E_1 of 0.74, and d_1 of 0.86 for the study period (Table 3.2). Amongst the dual-source models being tested, the ET estimates from the S-W and T-P models have almost the same diurnal patterns (Fig. 3.3d) and similar statistic values (Table 3.2), suggesting that these two models can be interchangeably used to estimate ET at the cropland site.

3.4.3 *Evapotranspiration Components (E and T) and Its Vegetation Controls*

Differing descriptions of vegetation coverage characteristics are the largest difference among the four ET models. In order to trace the error of ET estimates and explore the underlying reasons, variations in daily LAI, *F*r, and estimated daily evaporation (E) and transpiration (T) from the three dual-source models at four sites are shown in Figs. 3.4, 3.5, 3.6 and 3.7. A summary of mean evaporation, mean transpiration, and the ratio of E/ET during study periods from each model is given in Table 3.3. Due to the inability to distinguish E and T, the P-M model was precluded from the following analysis.

At the US_MMS site where LAI varied markedly and soil moisture remains relatively constant at a high level (favorable water conditions, Fig. 3.1a) during the study period, variations in transpiration from the H-D model show an obvious positive relationship with those in LAI, whereas evaporation is negatively correlated with LAI (Fig. 3.4a, b). Similar relationships were also found for the S-W model (Fig. 3.4c, d). However, both E and T from the T-P model did not show obvious variation with changes in LAI. This is because LAI is not used in the T-P model, while *F*r is the only variable used to account for the vegetation controls on E and T partitioning. During the study period, *F*r remained nearly invariant. As a result, both E and T from the T-P model show dampened variations compared with those from the H-D and S-W models (Fig. 3.4e, f).

The ratio of E/ET was similar between the H-D and the S-W models (Table 3.3). However, the S-W model predicted higher values of both E and T compared with the H-D model. Given the fact that the H-D model accurately estimated the total ET while the S-W model overestimated it (Figs. 3.2a, e and 3.3a and Table 3.2), it is plausible that both E and T were overestimated in the S-W model. Similarly, the E/ET ratio from the T-P model was much higher than that from the H-D model, suggesting that the T-P model overestimated E and underestimated T at this site (Table 3.3).

At the US_Fmf site, both LAI and *F*r remained generally invariant during the simulation period. Variations in E and T were therefore controlled primarily by atmospheric and soil moisture conditions. It is observed that T from the three

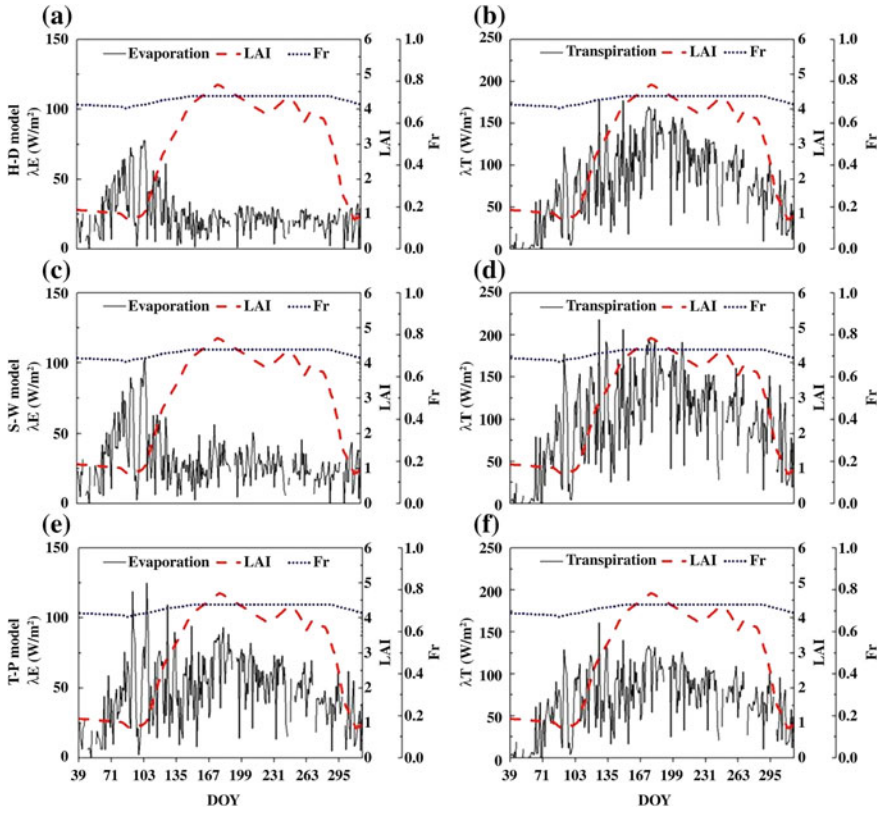

Fig. 3.4 Variations in daily leaf area index (*LAI*), fractional vegetation coverage (*Fr*), and estimated evaporation (λE) (*left panel*) (**a**, **c** and **e**) and transpiration (λT) (*right panel*) (**b**, **d** and **f**) from three dual-source ET models at the US_MMS site (Yu et al. 2014)

models showed similar trends that appear to increase before ~DOY 130 and then to decrease to a low level between ~DOY 140 and ~DOY 210. Afterwards, T started to increase again. This trend corresponds well with that of soil moisture shown in Fig. 3.2b, suggesting a strong moisture control on plant transpiration at this site. Although the surface vegetation condition was not the influential factor controlling seasonal variations in E and T, it does play a key role in partitioning ET into E and T. Because both the LAI and *Fr* were small at this site, E accounted for a larger proportion of total ET (Table 3.3). The ratio of E/ET_a was the highest from the H-D model (82.8 %) and lowest from the S-W model (77.8 %). For the T-P model, the E/ET ratio was 81.3 %. Combining the results listed in Tables 3.2 and 3.3, it was found that the S-W model overestimated T but the proposed H-D model underestimated T. In addition, both E and T were significantly overestimated by the T-P model.

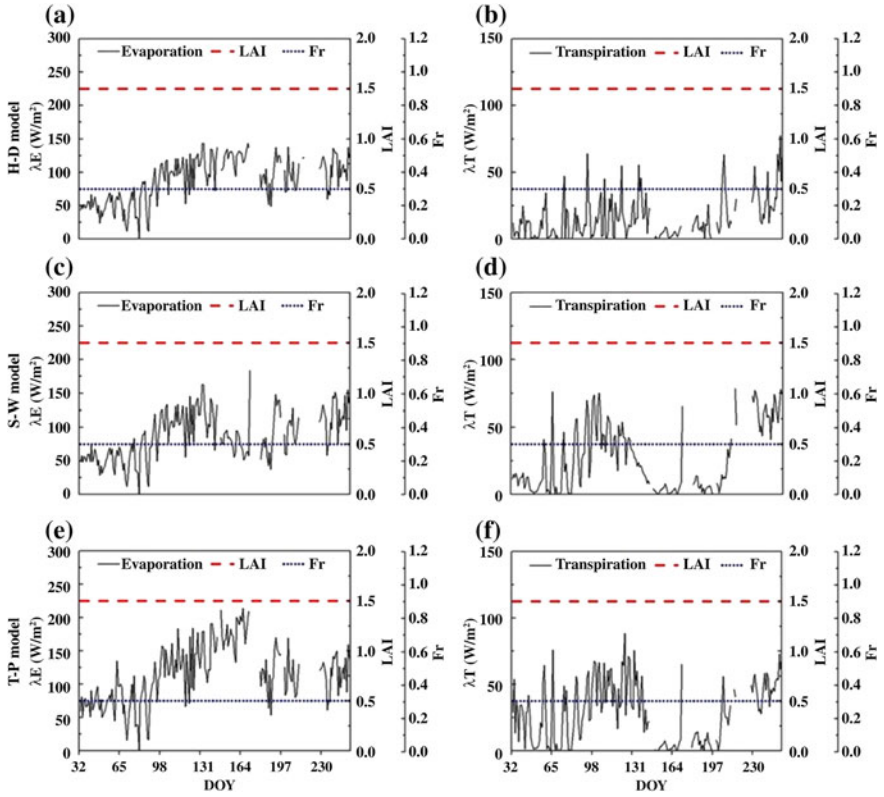

Fig. 3.5 Variations in daily leaf area index (*LAI*), fractional vegetation coverage (*Fr*), and estimated evaporation (λE) (*left panel*) (**a**, **c** and **e**) and transpiration (λT) (*right panel*) (**b**, **d** and **f**) from three dual-source ET models at the US_Fmf site (Yu et al. 2014)

At the US_Var site, LAI showed obvious seasonal variations while *F*r remained invariant. Evaporation from both the H-D and S-W models had similar values (Table 3.3) and remained relatively constant despite changes in LAI. This is possibly because that the actual evaporation process at this site was controlled mostly by the variability in meteorological and soil moisture conditions. During the study period, atmospheric demand was expected to increase with time, and soil moisture remained at a high level before ~DOY 100 but showed an abrupt decrease afterwards (Fig. 3.1c), which may somehow offset the increase in atmospheric demand and result in a relatively unchanged evaporation rate. Such an effect could also affect the process of transpiration. However, T from the S-W model exhibited a sharp increase after ~DOY 100 despite the reduction in soil moisture (Fig. 3.6d), resulting in a higher/lower T/E ratio in the S-W model (i.e., E/ET = 45 %). In contrast, T from the H-D model that shows a more gradual increase with LAI after ~DOY 100 seems to be more reasonable (Fig. 3.6b). The above phenomenon suggests that the S-W model may respond to changes in LAI/soil moisture more/

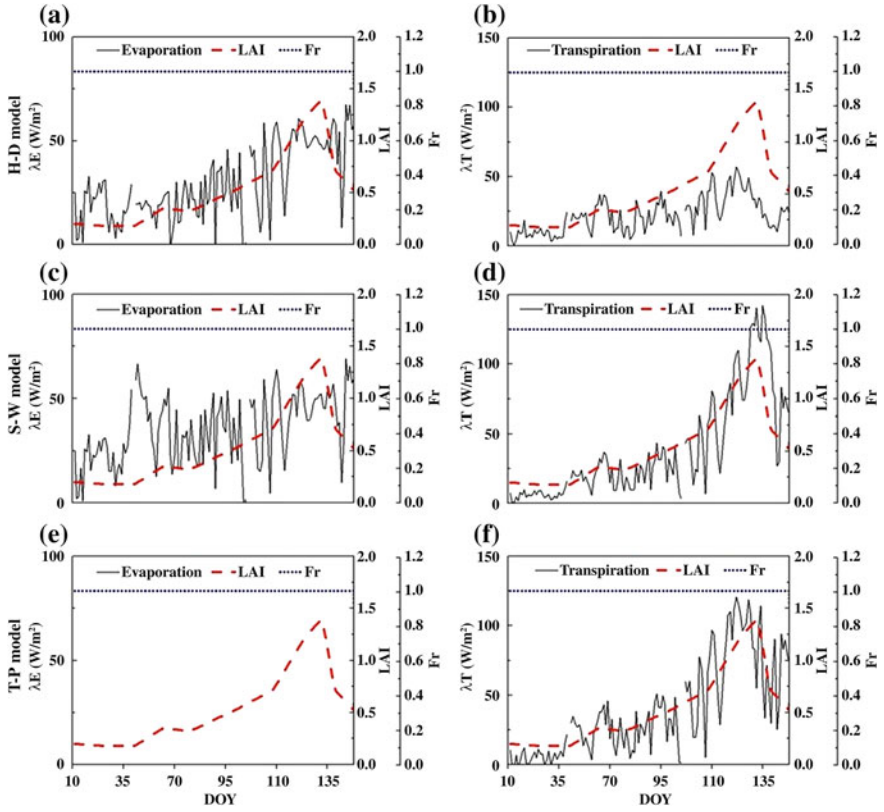

Fig. 3.6 Variations in daily leaf area index (*LAI*), fractional vegetation coverage (*Fr*), and estimated evaporation (λE) (*left panel*) (**a**, **c** and **e**) and transpiration (λT) (*right panel*) (**b**, **d** and **f**) from three dual-source ET models at the US_Var site (Yu et al. 2014)

less sensitively than the H-D model does. Considering that the H-D model estimated total ET more precisely while the S-W model considerably overestimated the total ET (Table 3.2), and both models predicted similar E (Table 3.3), it could be derived that the S-W model overestimated the T at this site. Studies also reported that the ratio of E/ET for the grassland with mean growing season LAI of 0.50 (close to 0.52 of the US_Var site) were between 56 and 60 % (Hu et al. 2009), which lends credibility to our findings at the US_Var site.

As for the T-P model, because the site was completely covered by vegetation, there was no evaporation occurred during the simulation period (Fig. 3.6e). It is interesting to note that the negligible E was well compensated by the overestimation of T due to higher canopy available energy, thereby resulting in comparable total ET_a estimates (Table 3.2). However, because of the obviously erroneous E and T partitioning, it is not recommended using the T-P model at the site.

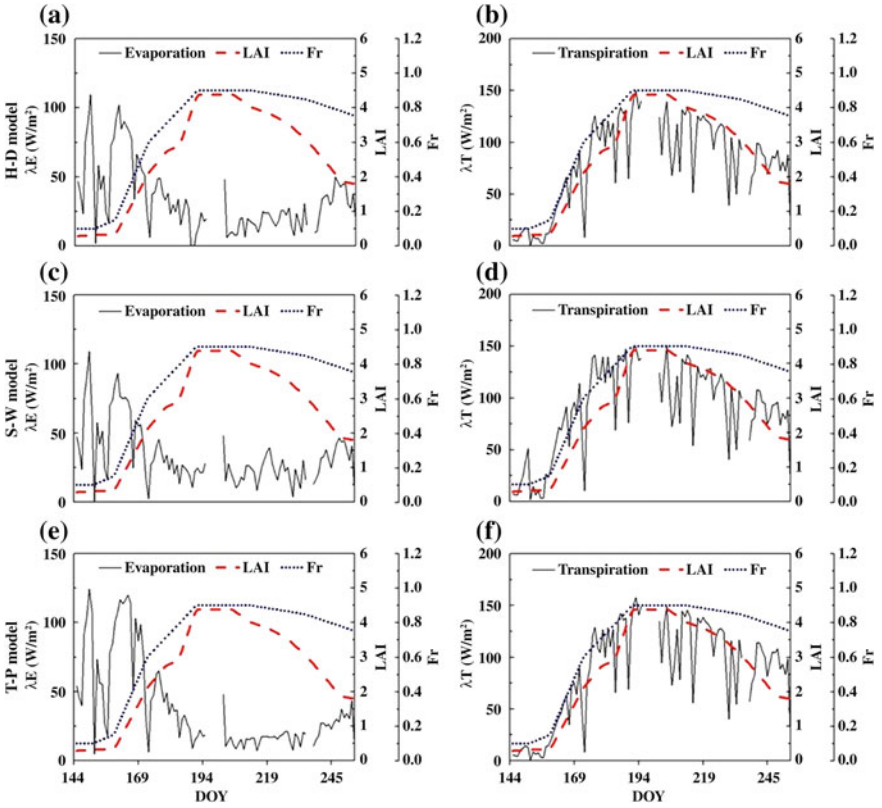

Fig. 3.7 Variations in daily leaf area index (*LAI*), fractional vegetation coverage (*Fr*), and estimated evaporation (λE) (*left panel*) (**a**, **c** and **e**) and transpiration (λT) (*right panel*) (**b**, **d** and **f**) from three-dual source ET models at the US_Bo1 site (Yu et al. 2014)

At the US_Bo1 site, soil moisture remained at a high level (Fig. 3.1d) and both LAI and *F*r changed synchronously during most of the simulation period (Fig. 3.7). As a result, both E and T estimated by all three models showed similar temporal patterns. The estimated transpiration was positively correlated with changes in LAI and *F*r, while the evaporation was negatively related with these two variables. In addition, the three models had similar E/ET ratios, with values ranging from 28.8 to 31.9 % (Table 3.3). However, the S-W and T-P models slightly overestimated T compared to the H-D model (Table 3.3). This overestimation of transpiration would likely be as a result of the overestimation in total ET by these two models (Table 3.2). Nevertheless, the overestimation of the S-W model happened mostly during the beginning and the end of the simulation period when LAI was generally low (Fig. 3.7b, d), whereas the overestimation of the T-P model mainly occurred in the end of the simulation period with low LAI but high *F*r values.

Similar results can also be found at three other sites that the S-W model tended to overestimate T when LAI was low, and therefore overestimated the total ET.

Table 3.3 Summary of mean evaporation (E, W/m^2), mean transpiration (T, W/m^2), and the ratio of E/ET (%) at four sites during study periods (Yu et al. 2014)

Model	US_MMS			US_Fmf			US_Var			US_Bo1		
	E	T	E/ET_a	E	T	E/ET_a	E	T	E/ET_a	E	T	E/ET_a
H-D	26.1	87.4	23.0	104.1	21.6	82.8	29.7	21.9	57.6	37.3	86.3	30.2
S-W	32.4	102.3	24.1	110.7	31.5	77.8	34.5	42.2	45.0	39.5	97.7	28.8
T-P	53.1	73.2	42.0	132.7	30.4	81.3	0	44.7	0	43.8	93.6	31.9

Conceptually, this is because the S-W model assumes fluxes from different components to be firstly fully coupled and then interact with the above atmosphere. However, when LAI is low, the interactions between fluxes from different components become less intense, which may contradict the assumption of the S-W model. This discrepancy would be even larger if *F*r is also small. Other similar studies also reported that the S-W model overestimated T under low LAI conditions (Brenner and Incoll 1997; Guan and Wilson 2009; Hu et al. 2009).

In contrast, the T-P model does not consider LAI. Instead, it uses *F*r to partition available energy and to rescale latent fluxes between components. As a result, the T-P model provided a relatively high transpiration rate under high *F*r conditions regardless of low LAI values. This phenomenon was not only found at the US_Bo1 site but also at the US_MMS and US_Var sites (Figs. 3.4 and 3.5).

3.4.4 Advantages of the Hybrid Dual-Source Model

Compared with the S-W and T-P models, the estimated E and T from the H-D model seem more reasonable. Not surprisingly, the H-D model performed best in estimating total ET (Table 3.2). The H-D model deviates from a layer model in distinguishing the difference in evaporation from inter-canopy soil and that from under-canopy soil, and restricting convective transfer contributions to transpiration only from vegetated fractions. The H-D model is also different from a patch model in that it allows E from under-canopy soil, and the effect of vegetation on both E and T is somehow considered. More importantly, both LAI and *F*r are adopted in the H-D model, while the S-W model only uses the LAI and the T-P model only uses the *F*r. It should be emphasized that LAI and *F*r are two variables representing different characteristics of surface vegetation distribution. LAI focuses on the vertical density and distribution of leaves, whereas *F*r explains more on the horizontal development of vegetation canopies. Therefore, both variables showed strong, but different controls on E and T processes (Figs. 3.4, 3.5, 3.6 and 3.7, see also Yang and Shang 2013). Although the value of both variables would change synchronously in some situations [i.e., in the farmland ecosystem, and thus resulted in similar E and T estimation among three dual-source models (Fig. 3.7)], they function differently in determining ET processes. Moreover, synchronized changes in LAI and *F*r rarely happen in natural ecosystems.

3.5 Conclusion

In this chapter, a hybrid dual source (H-D) model is developed and applied in four different ecosystems to estimate actual ET processes. Outputs of the H-D model were tested against eddy covariance measurements and compared with three other ET models. The results indicate that:

(1) The H-D model could generate accurate ET estimates in different ecosystems, with mean absolute errors ranging from 16.3 to 38.6 W/m^2, modified coefficient of efficiency ranging from 0.56 to 0.79, and modified index of agreement ranging from 0.48 to 0.87;
(2) The H-D model generally gives better ET estimates and E and T partitioning than the three other models (i.e., MAE = 33.8–51.4 W/m^2 for the S-W model, MAE = 24.4–53.2 W/m^2 for the T-P model and MAE = 15.7–99.5 W/m^2 for the P-M model), suggesting that the H-D model appear to be more suited for ET estimation over surfaces with different vegetation patterns;
(3) The P-M model significantly underestimates ET in the savannas ecosystem (i.e., MAE = 99.5 W/m^2), but generally performs well in other three ecosystems;
(4) The S-W model tends to overestimate plant transpiration when LAI is low, and the T-P model tends to overestimate plant transpiration under low LAI but high *Fr* conditions.

References

Brenner AJ, Incoll LD (1997) The effect of clumping and stomatal response on evaporation from sparsely vegetated shrublands. Agric For Meteorol 84:187–205

Edlefson N, Anderson A (1943) Thermodynamics of soil moisture. Hilgardia 15:31–298

Guan H, Wilson JL (2009) A hybrid dual-source model for potential evaporation and transpiration partitioning. J Hydrol 377:405–416

Haise HR, Haas HJ, Jensen LR (1955) Soil moisture studies of some great plains soils: II. Field capacity as related to 1/3-atmosphere percentage, and "minimum point" as related to 15- and 26-atmosphere percentages 1. Soil Sci Soc Am J 19:20–25

Hu Z, Yu G, Zhou Y et al (2009) Partitioning of evapotranspiration and its controls in four grassland ecosystems: application of a two-source model. Agric For Meteorol 149:1410–1420

Huete A, Didan K, Miura T et al (2002) Overview of the radiometric and biophysical performance of the MODIS vegetation indices. Remote Sens Environ 83:195–213

Jung M, Reichstein M, Ciais P et al (2010) Recent decline in the global land evapotranspiration trend due to limited moisture supply. Nature 467:951–954

Legates DR, McCabe GJ Jr (1999) Evaluating the use of "goodness-of-fit measures" in hydrologic and hydroclimatic model validation. Water Resour Res 35:233–241

Massman WJ (1992) A surface energy balance method for partitioning evapotranspiration data into plant and soil components for a surface with partial canopy cover. Water Resour Res 28:1723–1732

Meyers TP, Hollinger SE (2004) An assessment of storage terms in the surface energy balance of maize and soybean. Agric For Meteorol 125:105–115

Mualem Y (1976) A new model for predicting the hydraulic conductivity of unsaturated porous media. Water Resour Res 12:513–522

Oliphant AJ, Dragoni D, Deng B et al (2011) The role of sky conditions on gross primary production in a mixed deciduous forest. Agric For Meteorol 151:781–791

Ortega-Farias S, Olioso A, Antonioletti R et al (2004) Evaluation of the Penman-Monteith model for estimating soybean evapotranspiration. Irrig Sci 23:1–9

Ortega-Farias S, Poblete-Echeverría C, Brisson N (2010) Parameterization of a two-layer model for estimating vineyard evapotranspiration using meteorological measurements. Agric For Meteorol 150:276–286

Penman HL (1948) Natural evaporation from open water, bare soil and grass. Proc R Soc A 193:120–145

Rana G, Katerji N, Mastrorilli M et al (1997a) A model for predicting actual evapotranspiration under soil water stress in a mediterranean region. Theor Appl Climatol 56:45–55

Rana G, Katerji N, Mastrorilli M et al (1997b) Validation of a model of actual evapotranspiration for water stressed soybeans. Agric For Meteorol 86:215–224

Ryu Y, Baldocchi DD, Ma S et al (2008) Interannual variability of evapotranspiration and energy exchange over an annual grassland in California. J Geophys Res 113:D09104

Schaap MG, Leij FJ, van Genuchten MT (1998) Neural network analysis for hierarchical prediction of soil hydraulic properties. Soil Sci Soc Am J 62:847–855

Seneviratne SI, Corti T, Davin EL et al (2010) Investigating soil moisture–climate interactions in a changing climate: a review. Earth Sci Rev 99:125–161

Sullivan BW, Kolb TE, Hart SC et al (2008) Thinning reduces soil carbon dioxide but not methane flux from southwestern USA ponderosa pine forests. For Ecol Manage 255:4047–4055

Stannard DI (1993) Comparison of Penman-Monteith, Shuttleworth-Wallace, and modified Priestley-Taylor evapotranspiration models for wildland vegetation in semiarid rangeland. Water Resour Res 29:1379–1392

van Genuchten MT (1980) A closed-form equation for predicting the hydraulic conductivity of unsaturated soils. Soil Sci Soc Am J 44:892–898

Wilson K, Goldstein A, Falge E et al (2002) Energy balance closure at fluxnet sites. Agric For Meteorol 113:223–243

Yang Y, Shang S (2013) A hybrid dual-source scheme and trapezoid framework-based evapotranspiration model (HTEM) using satellite images: algorithm and model test. J Geophys Res Atmos 118:1–17

Yu H, Liu T, Yang Y et al (2014) A hybrid dual-source model of estimating evapotranspiration over different ecosystems and implications for satellite-based approaches. Remote Sens 6:8359–8386

Chapter 4
A Hybrid Dual-Source Scheme Based Soil-Plant-Atmosphere Continuum Model (HDS-SPAC) for Water and Heat Dynamics

4.1 Introduction

Soil-plant-atmosphere continuum (SPAC) models are effective tools to describe the basic processes of coupled mass and energy transfer, which are important for climatic, hydrologic, ecological and agricultural studies. During the past decade, various models have been developed to partition available energy at the soil-plant-atmosphere interface and to simulate mass or energy movement in the soil. Examples include those developed by Wilson et al. (2003), Lee and Mahrt (2004), Lei et al. (2008) and Krobel et al. (2010).

A common SPAC model usually includes two parts, the below-ground part (soil) and the above-ground part. The former mainly focuses on simulations of coupled water and heat transfer in the soil system, and the latter aims at the total energy partitioning between latent heat for evaporation and transpiration, sensible heat, and ground heat flux. However, due to the complexity of above-ground momentum, energy and water transfer, various surface schemes with different conceptualizations have been used in different SPAC models. As shown in previous chapters, for homogeneous surfaces with a dense vegetation cover, a single-source model [e.g., the widely used Penman-Monteith model (Monteith 1965)] may be suitable. However, for surfaces with a heterogeneous canopy cover, a multi-source scheme provides a more realistic representation of the turbulent and energy exchanges (Kustas and Norman 1999; Sánchez et al. 2008).

The primary objective of this chapter is to extend the H-D model to a hybrid dual-source SPAC model (HDS-SPAC) by including subsurface soil heat and water dynamics. By this way, it is possible to study the mechanisms and interactions among different sub-processes that constitute the entire land surface process. In addition, a special focus on plant root water uptake process will be made in this chapter by designing a simple non-invasive filed-based root water uptake experiment for examining and parameterizing root water uptake models. Furthermore,

Y. Yang, *Evapotranspiration Over Heterogeneous Vegetated Surfaces*,
Springer Theses, DOI 10.1007/978-3-662-46173-0_4

improvements will be made to current root water uptake models and the improved models will be incorporated into the HDS-SPAC model to simulate water and heat transfer in a natural forest ecosystem.

4.2 Model Development

The HDS-SPAC model includes five main modules. They are modules for energy budget, canopy interception, atmospheric turbulence, soil water and heat dynamics, and root water uptake. The energy budget module calculates the available solar radiation on the surface, and partitions it between components to estimate sensible heat, latent heat and ground heat fluxes. The canopy interception module determines the amount of water occasionally intercepted by the canopy during a rainfall event. The atmospheric turbulence module calculates aerodynamic and surface resistances for vapor, heat and momentum transfers. The soil dynamics module describes the coupled heat and water transport in the soil and related infiltration processes, and estimates deep percolation. The root water uptake module determines the spatiotemporal variations of water absorbed by plant roots under different soil moisture conditions and plant physiology status.

4.2.1 Surface Energy Budget

In HDS-SPAC, the net radiation on the surface is expressed by,

$$A' = R_n - A_{it} \tag{4.1}$$

where R_n is total net radiation of the surface (W/m^2), and A_{it} is the energy consumed for the evaporation of intercepted rainfall (W/m^2). As a result, A' is the total net radiation minus occasional intercepted-water evaporation loss (W/m^2). R_n in HDS-SPAC can be estimated by published empirical method based on various degree of data availability (Allen et al. 1998).

The surface is divided into two components in HDS-SPAC (Fig. 4.1), vegetation canopy and soil. Radiation at the surface is thus further allocated to these two components [A_s for soil and A_c for canopy (W/m^2)], using a layer approach based on Beer's law:

$$A_s = A' e^{-k_c \mathrm{LAI}} \tag{4.2}$$

$$A_c = A'(1 - e^{-k_c \mathrm{LAI}}) \tag{4.3}$$

where LAI is bulk surface leaf area index, which is the production of canopy leaf area index L_c (one-side leaf surface area above unit area of the canopy-covered

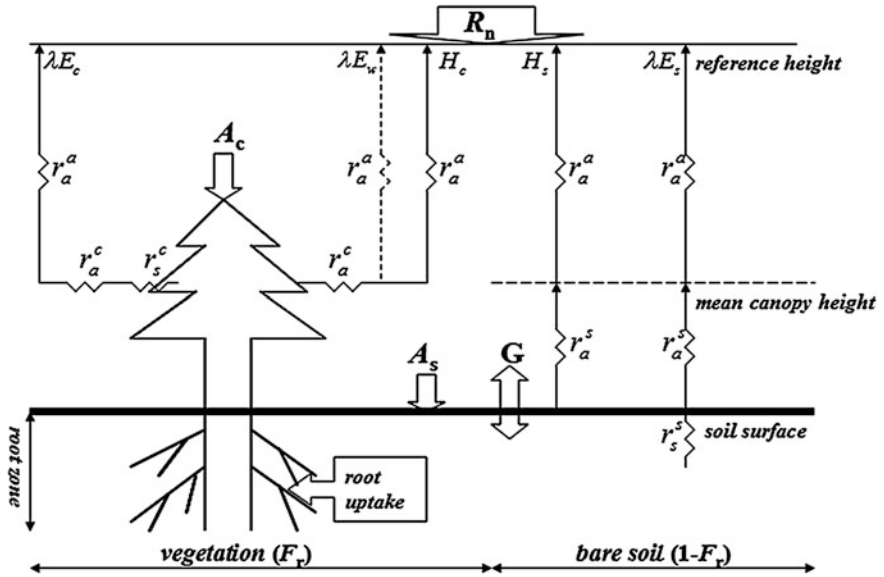

Fig. 4.1 Schematic diagram of energy partition processes and resistance network for HDS-SPAC [modified from Guan and Wilson (2009)]. The nomenclature used is given in Sect. 4.2

ground surface) and the fractional vegetation coverage Fr of the surface (LAI = L_c*Fr). k_c is the extinction coefficient for net radiation and is fixed at 0.4 following Guan and Wilson (2009).

The available energy for canopy (A_c) and inter-canopy soil (A_s) are further partitioned into latent heat, sensible heat and ground heat flux by patch approach. In the patch approach, each patch acts independently of the other and fluxes of each component represents an average value per unit area of the component under consideration (not the whole ground), which means that the average values per unit ground area should be weighted by the fractional coverage of each component.

$$A_c = Fr * (\lambda E_c + H_c) \tag{4.4}$$

$$A_s - G = (1 - Fr) * (\lambda E_s + H_s) \tag{4.5}$$

where λ is the latent heat of vaporization; A is the available energy per unit ground area (W/m^2); subscripts s and c stand for inter-canopy soil component and canopy component, respectively; G is ground heat flux (W/m^2); λE is the latent heat flux per unit component area (W/m^2); H is the sensible heat flux per unit component area (W/m^2).

In HDS-SPAC, evaporation from the soil and transpiration from the canopy can be separately derived similar to that of the Penman and Penman-Monteith equations). According to Lin and Sun (1983), the soil surface resistance is necessary in

estimating soil evaporation. As a result, evaporation and transpiration from the total surface area are

$$\lambda\langle E_c\rangle = \frac{\Delta A_c + Fr\frac{\rho_a C_p}{r_a^c + r_a^a}(e_{sat}(T_z) - e_z)}{\Delta + \gamma(1 + \frac{r_s^c}{r_a^c + r_a^a})} \tag{4.6}$$

$$\lambda\langle E_s\rangle = \frac{h_u\Delta(A_s - G) + (1 - Fr)\frac{\rho_a C_p}{r_a^s + r_a^a}(h_u e_{sat}(T_z) - e_z)}{\Delta h_u + \gamma(1 + \frac{r_s^s}{r_a^s + r_a^a})} \tag{4.7}$$

where a variable enclosed in < > represents the "total surface area" value; ρ_a is the air density (kg/m^3); C_p is the specific heat of moist air at constant pressure (J/ kg K); Δ is the slope of the saturated vapor pressure-temperature curve (Pa/K); γ is the psychrometric constant (≈66Pa/K); e_{sat} represents the saturated vapor pressure (Pa); e (Pa) and T (K) stand for actual vapor pressure and air temperature, respectively; subscript z refers to the level at the reference height (m); r_a^a is the aerodynamic resistance between mean canopy height and the reference height (s/m); r_a^s is the aerodynamic resistance between soil surface and mean canopy height (s/m); r_a^c is the aerodynamic resistance between mean leaf surface and mean canopy height (s/m); r_s^c is the bulk canopy stomatal resistance; r_s^s is the soil surface evaporation resistance (s/m). Parameter h_u in Eq. (4.7) is calculated based on the assumption that water in the liquid and vapor phases are in local thermodynamic equilibrium (Edlefson and Anderson 1943),

$$h_u = \exp(\frac{gh_s}{RT_s}) \tag{4.8}$$

where g is the acceleration of gravity (m/s^2); R is gas constant for water vapor (=461.5 J/ kg K); h_s (m) and T_s (K) are matric potential and temperature of surface soil, respectively.

4.2.2 Canopy Interception

During a rainfall event, a fraction of rainfall is intercepted by vegetation canopy. This amount of water evaporates back to the air at the potential rate from the wet fraction of the canopy, while the remaining part of canopy transpires. As a result, the available energy for canopy component is thus partitioned into three parts: sensible heat, latent heat for transpiration from dry canopy, and latent heat for evaporation from wet canopy.

According to Deardorff (1978), the wet fraction of the canopy is defined as

$$\delta = (W_r/W_{\max})^{2/3} \quad 0<\delta<1 \tag{4.9}$$

where $W_{\max}$ means the maximum capacity of interception (mm); W_r is the actual amount of water intercepted by foliage, which can be expressed as (Noilhan and Planton 1989),

$$\frac{\partial W_r}{\partial t} = P - P_g - E_w \tag{4.10}$$

where P is the rainfall intensity above the canopy (mm/s); P_g is the throughfall intensity (mm/s); E_w represents evaporation of the intercepted rainfall from the wet fraction (mm/s). In Eq. (4.9), $W_{\max}$ is given by Noilhan and Planton (1989),

$$W_{\max} = 2 \times 10^{-4}\sigma_f \mathrm{LAI} \tag{4.11}$$

where σ_f is a shielding factor, which is expressed as a function of LAI following Taconet et al. (1986),

$$\sigma_f = 1 - \exp(-0.4\mathrm{LAI}) \tag{4.12}$$

As discussed above, when it rains, transpiration only happens over the dry part of the canopy. Thus, Eq. (4.6) can be rewritten as

$$\lambda\langle E_c\rangle = \frac{(1-\delta)[\Delta A_c + Fr\frac{\rho_a C_p}{r_a^c+r_a^a}(e_{sat}(T_z) - e_z)]}{\Delta + \gamma(1+\frac{r_s^c}{r_a^c+r_a^a}) + \Delta\delta\frac{r_s^c}{r_a^c+r_a^a}} \tag{4.13}$$

and the evaporation of intercepted rainfall E_w is calculated from

$$\lambda\langle E_w\rangle = \frac{\delta[\Delta A_c + Fr\frac{\rho_a C_p}{r_a^c+r_a^a}(e_{sat}(T_z) - e_z)]}{\gamma + \Delta\delta + \Delta(1-\delta)(\frac{r_a^c+r_a^a}{r_a^c+r_a^a+r_s^c})} \tag{4.14}$$

4.2.3 Soil Water/Heat Dynamics

The method proposed by Philip and de Vries (1957), and modified by Milly (1982), is adopted for HDS-SPAC to simulate simultaneous heat and water movement in the saturated-unsaturated zone. In farmland ecosystems, because the soil water content is often artificially kept at a high level, it is reasonable to neglect water vapor movement in the soil (Milly 1984). Likewise, effect of thermally induced liquid water transport can also be neglected. In addition, Celia and Bouloutas (1990) reported that numerical solution based on the *h*-based form of Richards

equation generally yields large mass balance errors, while using a mixed form of Richards equation could commendably solve this problem. In HDS-SPAC, heat and water movement in the soil are described by

$$\frac{\partial \theta}{\partial t} = \frac{\partial}{\partial z}\left[K(h)\frac{\partial h}{\partial z}\right] - \frac{\partial K(h)}{\partial z} - S_w \tag{4.15}$$

$$C_T(\theta)\frac{\partial T}{\partial t} = \frac{\partial}{\partial z}\left[K_T(\theta)\frac{\partial T}{\partial z}\right] \tag{4.16}$$

where θ is the soil water content (m^3/m^3); t is time (s); $K(h)$ is the unsaturated hydraulic conductivity, which is a function of the soil matric potential h (m/s); S_w is the root water uptake (1/s) and is described in detail in Sect. 2.5; T is soil temperature in Kelvin (K); $C_T(\theta)$ is specific heat capacity (J/m^3 K) and $K_T(\theta)$ is soil thermal conductivity (W/m K). These two soil thermal properties are highly depended on soil water content. According to de Vries (1963) and Chung and Horton (1987), they can be calculated from

$$C_T(\theta) = 10^6 \times [1.925(1-\theta_s) + 4.184\theta] \tag{4.17}$$

$$K_T(\theta) = b_1 + b_2 + b_3\theta^{0.5} \tag{4.18}$$

where b_1, b_2, b_3 are three empirical coefficients depending on the soil type. The modified VG-M model (Mualem 1976; van Genuchten 1980) is adopted to describe soil hydraulic properties in the HDS-SPAC model.

4.2.4 Root Water Uptake

A macro-scope root water uptake model, which considers the root water uptake as a sink term in the root zone soil water continuity equation (averages water uptake over a large number of root), is adopted in the HDS-SPAC model to simulate water uptake by plant roots. The basic equation of a macro-scope root water uptake model is,

$$S = \alpha(h) * S_p \tag{4.19}$$

where S and S_p are the actual and potential root water uptake rates, respectively. α(h) is the water stress response function reducing actual root water uptake from the potential rate, which is a prescribed dimensionless function of root zone soil water potential h ($0 \le \alpha(h) \le 1$).

In the soil-plant-atmosphere continuum, if the change of water storage in the plant is assumed negligible (Tyree and Yang 1990), root water uptake rate equates plant transpiration rate. Then, Eq. (4.19) can be rewritten as:

$$\sum S = T = \alpha(h) * PT \tag{4.20}$$

or

$$\alpha(h) = T/PT \tag{4.21}$$

where T is actual transpiration, PT is potential transpiration. Feddes and Raats (2004) reviewed various forms of water stress functions α(h) that have been proposed over years. Among these functions, two of them have been commonly used, which were proposed respectively by Feddes et al. (1978) and van Genuchten (1987).

In Feddes model (Fig. 4.2a), the water stress function is defined linearly for three intervals of soil water potentials of h_1, h_2, h_3 and h_4. When soil is wetter than h_1 (anaerobiosis point), the plant roots are short of oxygen. Under this condition, the water uptake is assumed to be zero. When soil is dryer than h_4 (wilting point), water uptake is also assumed to be zero. Water uptake is assumed to be optimal when the soil water potential is between h_2 and h_3, while for soil water potential between h_1 and h_2 (or h_3 and h_4), water uptake increases (or decreases) linearly with h. h_{3h} and h_{3l} represent the value of h_3 when potential transpiration is high or low, respectively.

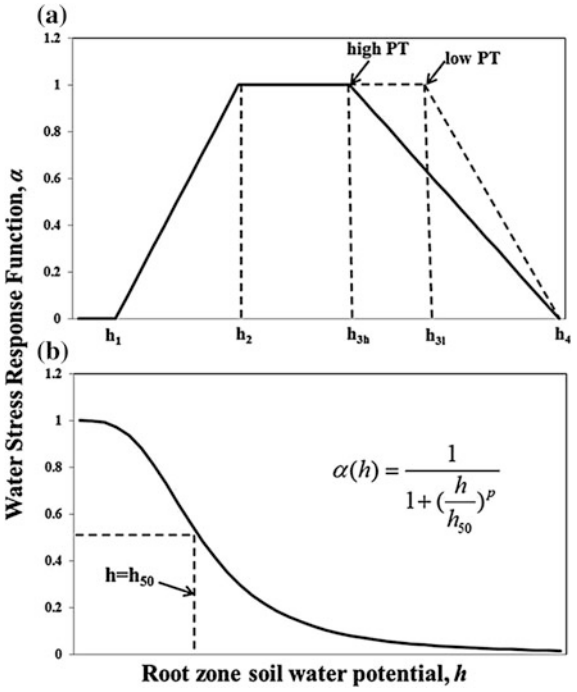

Fig. 4.2 Schematic of the root water uptake water stress response function, α(h), as used by **a** Feddes et al. (1978) and **b** van Genuchten (1987) (Yang et al. 2013)

In contrast, the function of van Genuchten is a smooth S-shape function to account for water stress (Fig. 4.2b). h_{50} represents the soil water potential at which the water extraction rate is reduced by 50 % from the potential rate,and p is an empirical coefficient. Different from Feddes model, the S-shape function does not consider the reduction in transpiration near saturation. However, this simplification is considered to be reasonable when saturated or near-saturated conditions occur for only a short period of time (van Genuchten 1987).

Once the water stress function is determined in the HDS-SPAC model, the rate of root water uptake at different root layers can be estimated from (Luo et al. 2000)

$$S = \frac{\alpha(h)RV(z)}{\int_0^{l_r} \alpha(h)RV(z)dz} \times T \tag{4.22}$$

where l_r is the depth of root zone (m) and RV is root density at different depth (m m^{-3}). According to Zhang (1999), we assume that the root density RV (root length of unit soil volume) of a certain plant is negatively exponential-distributed in the vertical direction,

$$\rho = 1 - e^{-cz} \tag{4.23}$$

$$RV = RL * c * e^{-cz} \tag{4.24}$$

where ρ is the proportion of root mass within 0–z soil depth to total root mass; c is a parameter reflecting plant growing phases (m^{-1}). When $cz = 1$, $\rho = 63$ %. Thus, the inverse of parameter c indicates the soil depth that contains 63 % of the total root mass. The relation between RL (the root length of unit area) and RV is

$$RL = \int_0^{\infty} RV\mathrm{d}z \tag{4.25}$$

4.2.5 Outline of Calculation Procedure and Numerical Solution

In the soil dynamic module, the coupled heat and water transport is numerically solved using a fully implicit finite difference method, with N nodes. Lee and Abriola (1999) reported that the accuracy of numerical solution is highly depended on time step as well as vertical discretization. They also summarized that coarse vertical discretization results in large overestimates and underestimates of near-surface soil moisture with overestimates predominating. Since the accurate estimates of near-surface soil moisture are important to correct estimation of soil evaporation and shallow-root transpiration, the finer vertical resolution is adopted in the present simulation (i.e., 0.01 m). The applied time step is 15 min, and numerical solution is

found to be stable in the case studies. To run the model, initial profiles of soil water content (or soil matrix potential) and temperature are required as well as two boundary conditions. For the lower boundary condition, the temperature is prescribed, and three options are available for the soil matric potential: (1) prescribed value (adopted in the current study); (2) specified flux value; (3) gravity flux (free drainage). The upper boundary condition is determined from the solution of soil evaporation and ground heat flux in Sects. 2.1 and 2.2. However, when the soil surface becomes saturated (e.g., after rainfall or irrigation), the upper boundary condition is automatically changed from prescribed flux to a known potential ($h = 0$). Root water uptake is a sink term of Richards equation, and its integral over the whole root zone was assumed to equal the plant transpiration rate. Because of non-linear interaction between water and heat transports and the implicit form of the boundary conditions, iterative calculations for moisture and temperature distributions are carried out at each time step until convergence on each node is obtained. During rainfall events, the canopy interception module is triggered and time step can be set shorter to guarantee the numerical stability for infiltration modeling, until all intercepted water has been evaporated. Moreover, as the time step of the model does not correspond to the time step of the measured weather data, the latter is interpolated using published methods between the recorded values (Cong 2003). For simplicity, plant characteristic parameters and root profiles are set unchanged within 1 day.

4.3 Model Application in Agricultural Ecosystem

4.3.1 Site and Data

The data to test the HDS-SPAC model were collected from a farmland ecosystem with the crop type of winter wheat. The farmland locates at 116° 40′ E and 39° 47′ in Yongledian Experiment Station, Beijing, with an average elevation of 12 m above sea-level. The mean annual temperature is 11.5 °C, and annual precipitation is about 570 mm with most occurring from June to August. Water table in this area is deeper than 5 m. The soil is sandy loam, with the bulk density of about 1.4 g/cm^3. Soil hydraulic parameters for the station were calibrated in former study (Shang et al. 2004) (Table 4.1).

Winter wheat (*Triticum aestivum* L.) is one of the main crops in this region. It grows in dry seasons from October to early June of the next year. During the soil frozen period from late November to next February, wheat grows very slowly or even stops for about 100 days. The growing period from greening (usually early March) to mature (late May) is the main concern in the following studies. The Feddes model is used to describe the root water uptake water stress function as suggested by previous studies (Luo et al. 2000).

In growing season of 1998–1999, experiments were carried out at 24 experiment plots (coded from A1 to F4). Daily meteorological data including air temperature, humidity, wind speed, atmospheric pressure, solar radiation and sunshine hours,

Table 4.1 Parameters used in the present study (Yang et al. 2013)

Parameter/variable	Symbol	Units	Value	Source
Fractional vegetation cover (A3 plot)	Fr	%	34.3–93.4	Measured
Fractional vegetation cover (E3 plot)	Fr	%	30.0–90.0	Measured
Leaf area index (A3 plot)	LAI	m^2/m^2	1.7–5.6	Measured
Leaf area index (E3 plot)	LAI	m^2/m^2	1.7–5.2	Measured
Characteristic length of leaf width	l_w	m	0.01	Cong (2003)
Maximum stomatal resistance	r_{max}	s/m	1,700	Cong (2003)
Minimum stomatal resistance	r_{min}	s/m	85	Cong (2003)
Plant growing phase parameter 120, 160, 180 and 230 days after sowing (12-Feb, 17-Mar, 13-Apr, and 2-June)	c	1/m	0.064, 0.057, 0.029, 0.025	Zhang (1999)
Saturated soil water content	θ_s	cm^3/cm^3	0.48	Measured
Residual soil water content	θ_r	cm^3/cm^3	0.01	Measured
Parameter in VG-M model	a_V	1/m	1.55	Shang et al. (2004)
	n_V		1.55	Shang et al. (2004)
Saturated hydraulic conductivity	K_s	m/s	0.42×10^{-5}	Shang et al. (2004)
Threshold values of soil matric potential	h_1	m	−0.3	Luo et al. (2000)
	h_2	m	−1	Site estimate
	h_3	m	−6	Luo et al. (2000)
	h_4	m	−15	Luo et al. (2000)
Empirical coefficients for Eq. (4.25)	b_1, b_2, b_3		0.243, 0.393, 1.534	Chung and Horton (1987)

as well as pan evaporation and rainfall were recorded by a weather station at the experimental site. A neutron probe was used to measure soil water content, and soil temperature was measured with thermistor. Crop canopy characteristics, such as crop height, leaf area index, vegetation cover, etc., were also measured. Detailed description of the experiment can be found in Shang et al. (2004).

In this study, we chose plots A3 and E3 as our target plots; they severally represent full irrigation of 230 mm and deficit irrigation of 60 mm. Since the maximum root depth of winter wheat is about 1 m, the upper 1 m soil layer is considered in the following analysis. Parameters used in the present study are summarized in Table 4.1.

4.3.2 Results and Discussion

Simulation was performed in the main growing period of winter wheat, from March 10th to May 30th in 1999. Vegetation coverage in these 3 months increased from 30 % at the beginning to about 93 % in the early May. Since the model is proposed to represent the effect of surface vegetation characteristics on quantifying evaporation and transpiration, this change in vegetation cover provides a perfect condition to test the HDS-SPAC performance.

4.3.2.1 Evaporation and Transpiration

Because rainfall was rare in this area during the simulation period (58.3 mm), total ET was strongly influenced by soil moisture regime as a result of irrigation scheduling. For A3 plot with full irrigation supply of 230 mm, soil moisture was always kept at a higher level, the total ET reached 261.9 mm. However, for E3 plot with the total irrigation amount of only 60 mm, the total ET is only 212.8 mm. The smaller ET for less irrigation application is mainly caused by higher stomatal resistance in response to water stress, which has also been reported in previous studies. Li et al. (2007) reported that soil moisture was the most important environmental factor controlling the dynamics of ET. Likewise, Miao et al. (2009) found that ET appeared to be more sensitive to soil moisture than biological factors (e.g., LAI, canopy conductance) in a dry year.

As shown in Fig. 4.3a, the simulation results are consistent with other modeling (Cong 2003; Shang et al. 2004) and experiment studies (Liu et al. 2002; Lei and Yang 2010) in the same region (North China Plain). Total ET increases almost linearly with the sum of irrigation and precipitation (I + P), with the coefficient of determination $R^2 = 0.891$.

However, when the total ET exceeds a critical value, further irrigation would not obviously increase total ET, and deep percolation will occur. Figure 4.3b shows the relationship between soil water use and the sum of irrigation and precipitation (I + P), which can also be expressed linearly ($R^2 = 0.988$). Soil water storage will be in balance if the I + P is about 260 mm. When I + P is larger than this critical value, water consumption by ET could be completely supported by irrigation and precipitation (e.g., plot A3 in the present test). Nevertheless, if the amount of I + P is small, crop can use a part of soil water in or below the root zone (e.g., plot E3 in the present test).

Figure 4.4 shows the daily evaporation and transpiration processes and Fig. 4.5 shows the relationship between vegetation characteristics and the ratio of daily evaporation to daily evapotranspiration (E/ET). With the increase of air temperature and sunlight hours, total daily evapotranspiration of both plots increase dramatically. However, this increase is mainly due to the increase of winter wheat transpiration, while the soil evaporation maintains at lower level with small fluctuations. At the greening stage with low vegetation cover, wheat transpiration and soil evaporation

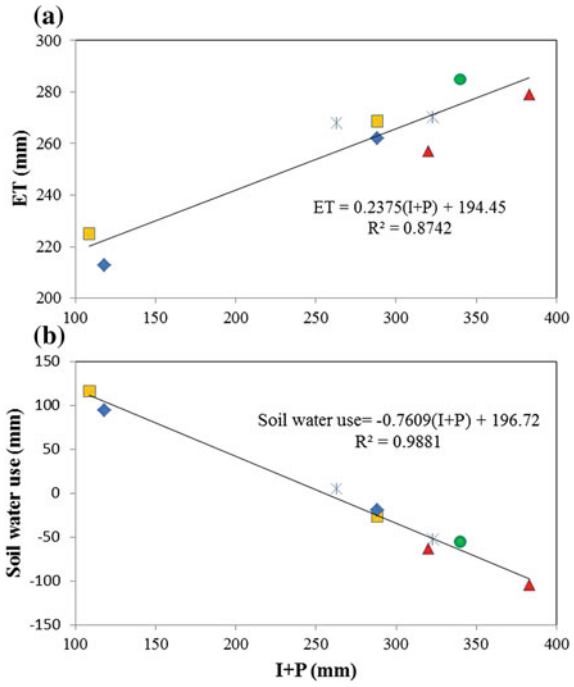

Fig. 4.3 Relationships between the sum of irrigation and precipitation ($I + P$) and ET (**a**) and soil water use (**b**). Different *symbols* represent different measurements or modeling results, (♦) the HDS-SPAC model, (■) the WheatSPAC model (Cong 2003), and (*) SMHT-SWT model (Shang et al. 2004) at Yongledian Station in Beijing, (●) weighing lysimeter measurement (Liu et al. 2002) at Luancheng Station in Heibei Province, and (▲) eddy covariance measurement (Lei and Yang 2010) at Weishan station in Shangdong Province (Yang et al. 2012)

contribute comparably to the total evapotranspiration. After that, vegetation cover increases quickly, which results in more canopy light interception and less evaporation from inter-canopy soil. In early May when vegetation coverage and leaf area index reached their maximum values, plant transpiration contributed to more than 90 % of the total ET in the study site. For A3 plot with full irrigation supply, the simulated ratio *E*/ET in the simulation period is 19.5 %. This is in consistence with lysimeter measurements in the North China Plain conducted by Liu et al. (2002), who found that the *E*/ET was near 20 % in main growing season of winter wheat under the ideal soil moisture condition. Although there was no direct measurement of E or T to test the accuracy of partitioning, the accordance with experimental studies in the same climate region would enhance our confidence in the performance of the model. However, the ratio E/ET for E3 plot is 18.1 %. While the continuous water deficit could exert a great influence on crop growth and hence result in a larger area of bare soil; the decrease in rate *E*/ET can possibly be explained by the rapidly increased soil surface resistance with decreased soil water content.

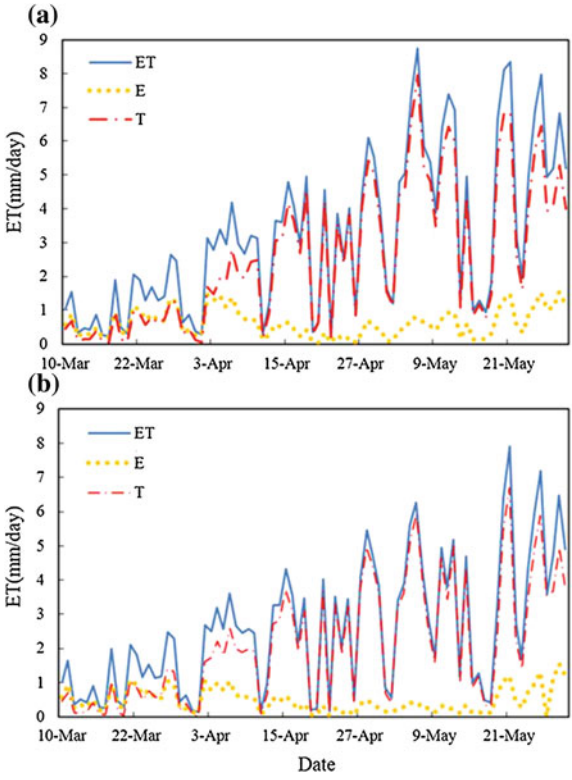

Fig. 4.4 Daily evaporation (*E*), transpiration (*T*) and evapotranspiration (*ET*) processes during simulation period for plots A3 (**a**) and E3 (**b**) (Yang et al. 2013)

Back to the introduction part where we pointed out that the hybrid dual source approach compromises the disadvantages of layer approach and patch approach, and thus allows HDS-SPAC to simulate heat and water transfer in an ecosystem with complicated and variegated surface characteristics (e.g., strong vegetation coverage change with time, or strong spatial gradient in vegetation density). From the radiation balance point of view, Eqs. (4.2) and (4.3) based on Beer's law allow evaporation from both inter-canopy soil and under-canopy soil. This is physically true, because radiation from different directions throughout the day is impossible to be intercepted by patchy canopy absolutely (Guan and Wilson 2009). Besides, Breshears and Ludwig (2009) found that inter-canopy substrate hardly receives full radiation loading even on surfaces with highly clumped vegetation. Although the amount of radiation received by inter-canopy soil may be different from that of under-canopy soil, the lump calculation is a good approximation, at least better than a normal patch approach where under-canopy evaporation is simply neglected.

Incorporating both bulk surface leaf area index LAI and fractional vegetation cover *Fr* allows the hybrid dual source approach to represent more vegetation characteristics than either the layer or the patch approach, while only LAI is

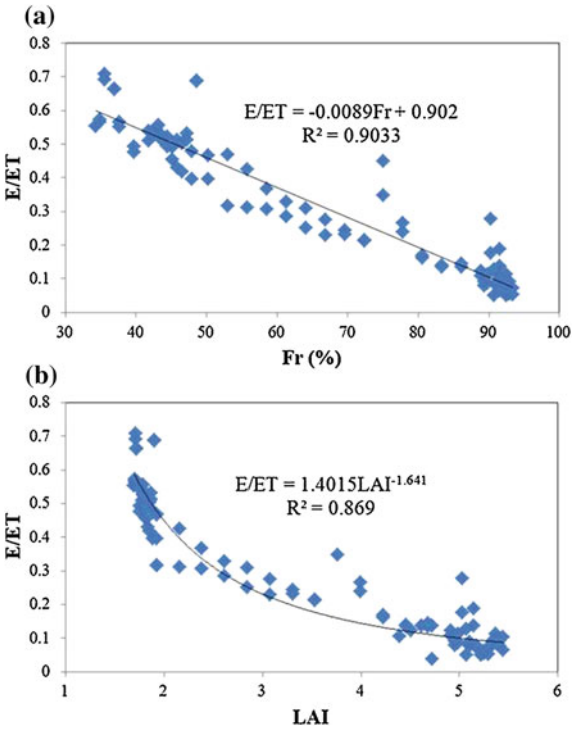

Fig. 4.5 Relationships between the ratio *E*/*ET* and two vegetation characteristics: **a** fractional vegetation cover (*Fr*), **b** bulk leaf area index (*LAI*), for both plots (Yang et al. 2013)

considered in the layer approach and only *Fr* in the patch approach. Both *Fr* and LAI are important factors in evaporation and transpiration partitioning, because both factors show strong correlation with *E*/ET but in different forms (Fig. 4.5). Although changes of *Fr* and LAI may be synchronized in some cases, it is not always the truth for all vegetated surfaces (e.g., highly clumpy vegetation). The combination of LAI and *Fr* could further reflect the clumpy degree of vegetation and is thus more adaptable to a surface with patchy vegetation patterns. Figure 4.6 compares PT and PE estimated from the hybrid approach with those from the layer approach for hypothetical vegetation covers [similar comparison can be found in Guan and Wilson (2009)]. The LAI is fixed at 1 and *Fr* varies from 0 to 1, which result in varying vegetation clumpy patterns. The results of the layer approach show that this approach gives similar PE and PT under different vegetation coverages. However, the hybrid approach estimates show that PT increases with *Fr* and PE decreases with *Fr*, which may capture the actual situation more appropriately than the layer approach. Mathematically, this is because *Fr* is included in the hybrid approach for routing vapor and heat fluxes. In the present test, the strong correlation between *Fr* and *E*/ET (Fig. 4.5a) could further support the conclusion that the hybrid approach can be applied to a wide range of surfaces with different vegetation coverages.

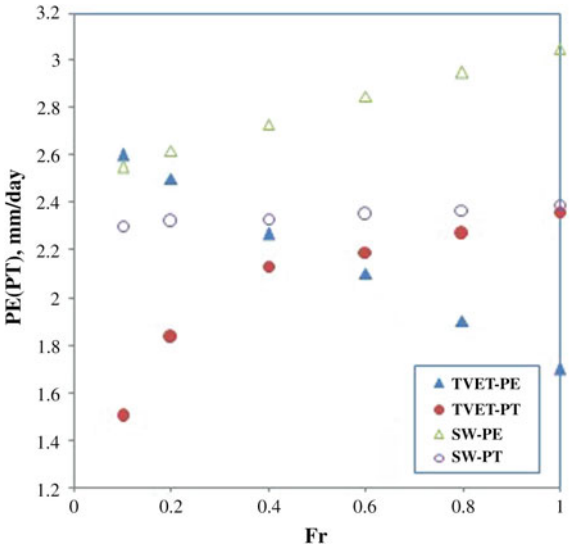

Fig. 4.6 Comparison of estimated *PE* and *PT* from the hybrid approach (*TVET*) and the layer approach (*SW*). [adopted from Guan and Wilson (2009) with permission]

4.3.2.2 Canopy Interception

The total rainfall interception during the simulation period is 7.57 mm for A3 plot and 7.03 mm for E3 plot, which account for 13 and 12.1 % of the total rainfall amount (58.3 mm), respectively. The maximum capacities of daily interception for winter wheat are 1.01 mm for A3 plot and 0.91 mm for E3 plot, which are in consistence with the field studies by Kang et al. (2005), who reported that the maximum value of winter wheat canopy interception was less than 1.0 mm. However, this value differs greatly in different studies, from 0.2 mm (Hough and Jones 1997) to more than 10 mm (Du et al. 2001). Kang et al. (2005) reported that canopy interception is affected by many factors, such as leaf area index, plant height, drop diameter, rainfall intensity and wind speed. Nevertheless, LAI and rainfall intensity are the only two controlling factors in the HDS-SPAC model. Since an increasing number of studies (Kang et al. 2005; Tolk et al. 1995) suggested that the canopy interception might be an important factor influencing field microclimate, a more realistic model is expected to better understand canopy interception and its influence on field microclimate.

4.3.2.3 Soil Water Content

Soil water balance in the upper 1 m soil layer was simulated, and these results will be compared with observed values in the following analysis.

As an example, Fig. 4.7 shows the simulated and observed soil water storages in 0–1 m soil layer for two different irrigation schedules. In general, agreements between measured and simulated soil water storage are good for both the full

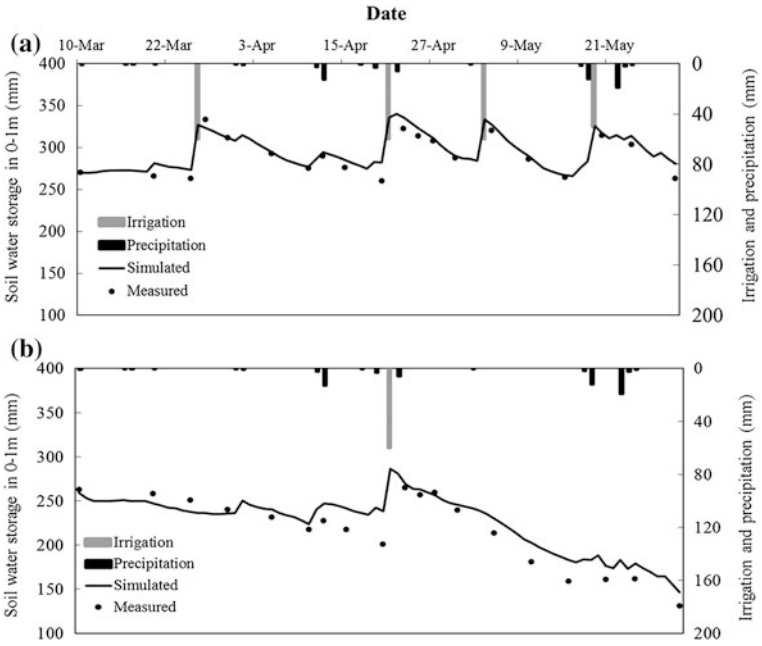

Fig. 4.7 Comparison between simulated and measured soil water storage in 0–1 m soil layer of A3 plot (**a**) and E3 plot (**b**) (Yang et al. 2013)

irrigation plot (A3) and the deficit irrigation plot (E3). Soil water content in the root zone follows dynamics of surface hydrological processes and development stages of crops. Although over half of simulated results are greater than measured values, the root-mean-square error (RMSE) for these two plots are 9.51 and 16.41 mm, which equal 3.4 and 7.5 % of the average water storage in 0–1 m soil layer, respectively. Comparisons between simulated and observed soil water content at different soil depths are also illustrated (Fig. 4.8). Soil moisture varies rapidly in upper soil layer but more gradually in lower layers. The simulated results showed an acceptable fit to the measured values for most soil layers except the topmost one. It may be caused by the impact of the air-soil interface on the neutron-probe reading. Besides, the topmost layer is the most vulnerable layer affected by human activities, which can result in considerable changes on soil physical characteristics. In addition, although the total amount of root water uptake is determined by transpiration, different root distributions pattern may still result in different shapes of soil water profile. Wells and Eissenstadt (2003) found that water uptake primarily occurs in young and unsuberized roots, and that the radial hydraulic conductivity of these young roots is 10–100 times higher than that of older roots, which is not considered in the present model. Moreover, the lower boundary condition of soil water dynamics is linearly interpolated between limited measurements with slight modifications. This simple treatment may also lead to some errors in numerical

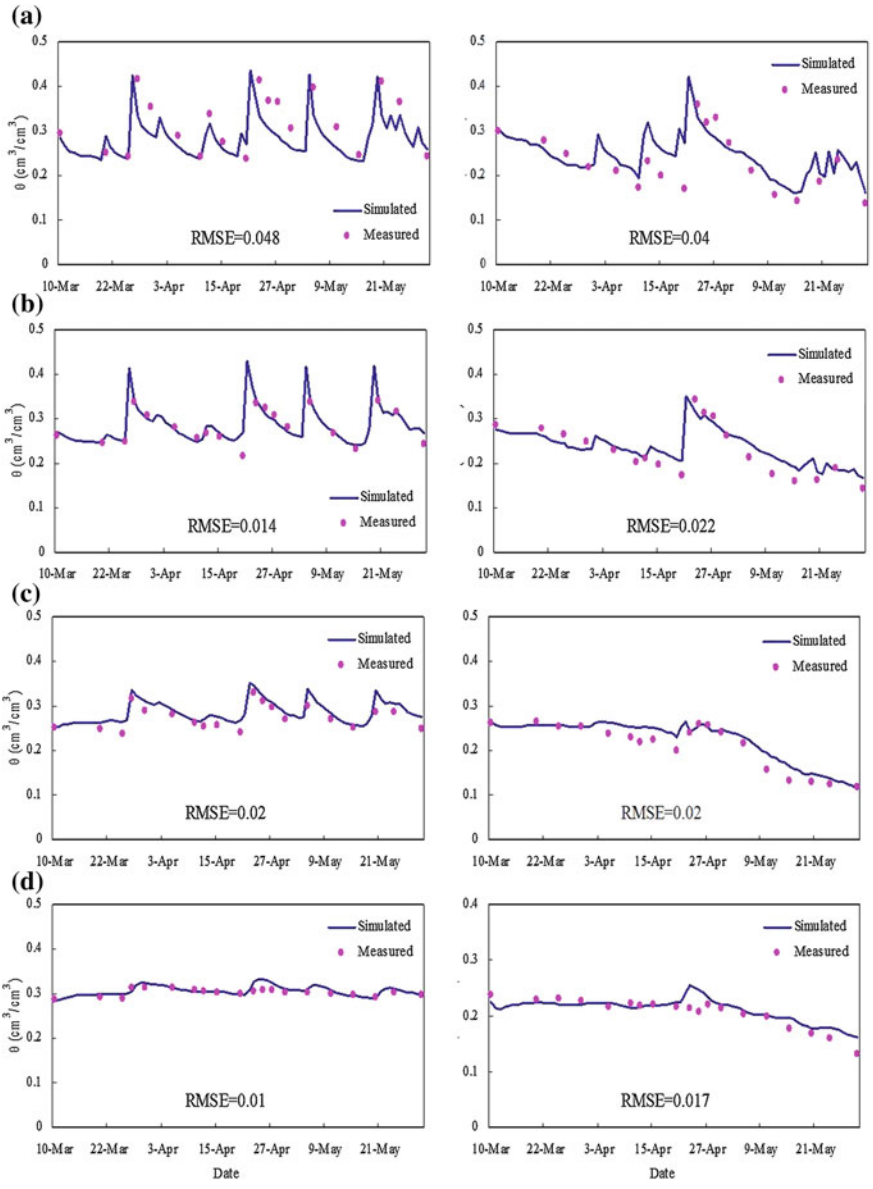

Fig. 4.8 Comparisons between simulated and measured soil water contents at 10 cm (**a**), 20 cm (**b**), 40 cm (**c**) and 80 cm (**d**) soil depth for full irrigation (A3, *left*) and deficit irrigation (E3, *right*). *RMSE* indicates the root-mean-square error (cm^3 cm^{-3}) (Yang et al. 2013)

solutions. All these factors should be among further efforts to improve the model. Nevertheless, the largest RMSE is 0.048 cm^3/cm^3, which indicates that the biggest discrepancy between simulated and observed soil water content is only 17.5 %.

Considering the uncertainty of neutron-probe measurement [±0.015 cm^3/cm^3 (Haverkamp et al. 1984)], the results of HDS-SPAC model are satisfactory.

4.3.2.4 Soil Temperature

Comparisons between simulated and observed soil temperature processes at different layers are shown in Fig. 4.9. In general, the simulated results agree well with the observed ones, and the largest RMSE are 1.56 and 1.45 °C for A3 and E3 plots, respectively. Considering the great variation of air temperature within a day and errors in temperature measurements, these disagreements are acceptable. Notably, the largest RMSE for both plots occurred in the top soil layer. Similar reasons for the discrepancy in modeling soil moisture at the top layer could possibly account for the difference found between measured and simulated soil temperatures, because the simulated water and heat transfer are highly coupled. In addition, all comparisons used the soil temperature at 8:00 in the morning, when surface temperature raised quickly. Thus, any small difference between the observation time (around 8:00 am) and the simulation time (8:00 am) will result in discrepancy between observed and simulated surface soil temperatures.

4.4 Model Application in Natural Forest Ecosystem

4.4.1 Site and Data

For model application in natural forest ecosystem, we selected a natural grove on the campus of Flinders University (138.572°E and 35.039°S). The site was on a south facing slope of 4 % (Fig. 4.10). It is characterized with a Mediterranean type climate, with a mean annual rainfall of 650 mm and mean annual temperature of 17.1 °C. The surface is covered by lawn with sparse trees. Data collected was conducted from 28th February to 18th May of 2011.

Drooping sheoak (*Allocasuarina verticillata*) was the main species in the site and is also an important native species in South Australia, which provides unique habitats for some valuable animals. Two trees (1.5 m apart) were chosen to conduct the experiment, their physiological characteristics are listed in Table 4.2.

Measurement of stem water potential: Thermocouple stem psychrometers (PSY, ICT International Pty Ltd., Australia) developed by Dixon and Tyree (1984), were used to measure stem water potential at a 15-min interval. The stem psychrometer is attached to the stem using a clamp to hold it in the position and is powered by either a 5 V battery or a 12 V solar panel. The measurement range of PSY is from −0.01 to −10 MPa, with an accuracy of ±0.01 MPa and a resolution of 0.002 MPa.

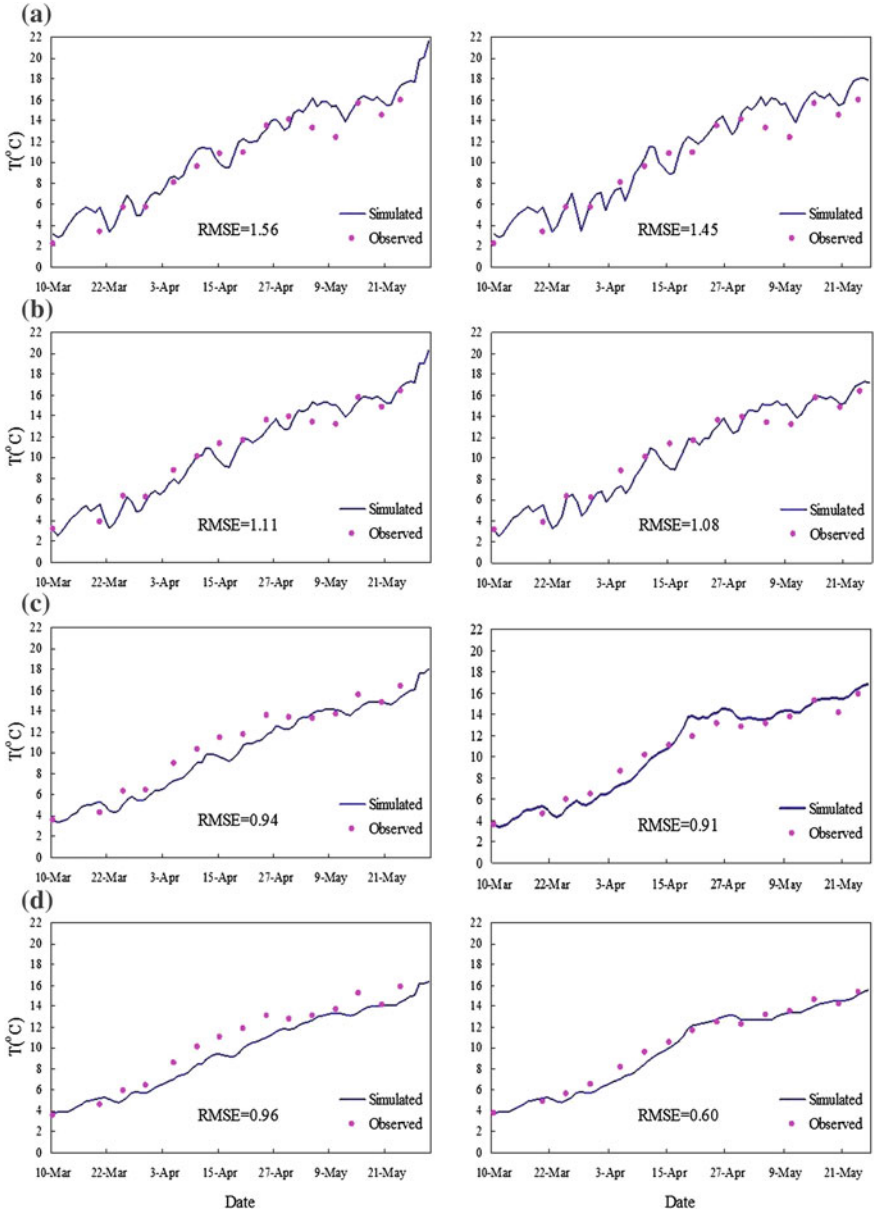

Fig. 4.9 Comparisons between simulated and measured soil temperature processes at 10 cm (**a**), 20 cm (**b**), 40 cm (**c**) and 60 cm (**d**) soil depth for full irrigation (A3, *left*) and deficit irrigation (E3, *right*). *RMSE* indicates root-mean-square error (°C) (Yang et al. 2013)

Fig. 4.10 Location of the study site and the experimental setup showing two trees are being monitored with stem psychrometers and sap flow meters (tree 1 on the *right*; tree 2 on the *left*) (Yang et al. 2013)

Table 4.2 Selected characteristics of both trees in the experiment

	Height (m)	Diameter at breast (m)	Canopy area (m^2)	LAI
Tree 1	6	0.15	21.7	1.3
Tree 2	6	0.13	14.5	1.1

Tree 1 is on the right, and tree 2 is on the left in Fig. 4.10 (Yang et al. 2013)

Measurement of sap flow: Heat-pulse sap flow sensors (SP, Tranzflo NZ Ltd., New Zealand) based on the compensation method proposed by Marshall (1958) were used to monitor sap flow at a 30-min interval. For each tree, two sets of sap flow probes were installed on the sunny and shade sides of the trunk, at a height of 0.7 m above ground. Each set comprises one heat pulse release probe (heater) and two temperature measurement probes (each one has 3 temperature sensors) situated 5 mm upstream and 10 mm downstream from the heater. The probe sets and data logger (Model CR1000, Campbell Scientific Inc., Utah, USA) were powered by one 12 V battery.

Following Green (2009), sapflows were corrected for the effects of wounds, sapwood area, radial variability, and sapwood water content, and were converted to transpiration based on the relationship between sapwood area and canopy projection area

$$T = \frac{V_s A_{sapwood}}{A_{canopy}} \tag{4.26}$$

where V_s is the sap velocity, A_{sapwood} and A_{canopy} are sapwood area and canopy projection area, respectively. The values in a 24-h period were summed to give a daily transpiration rate.

Other measurements: Micrometeorological data, including global radiation, air temperature, relative humidity, rainfall and wind speed, were measured with a standard automatic weather station located about 150 m from the experimental site. Leaf area index (LAI) was measured using a hemispherical photography method (Zhang et al. 2005), with a high-resolution digital camera and hemispherical (fisheye) lens to capture the canopy image (Table 4.2).

4.4.2 Determination of the Stress Function for Root Water Uptake

Because this is the first study on the root water uptake of drooping sheoak, there have been no previous suggestions on the type and parameters for the water stress function of drooping sheoak. To appropriately choose and parameterize a water stress function is of importance in modeling root water uptake (transpiration) and soil water flow, because in most cases, plants suffer a certain degree of water stress. Under such conditions, plant roots cannot uptake water from the surrounding soil at the potential rate defined by the atmospheric demand. The dependence of root water uptake on soil water availability is quantified by the water stress function for modeling purpose.

Unfortunately, water stress functions are generally very difficult to determine experimentally. Few studies have addressed this difficulty because of the following reasons. (1) The water stress function is a hydrological expression of the plant physiological characteristics. Very likely, it varies from species to species, and thus need to be determined separately (van Dam and Feddes 2000). (2) Simultaneous measurements of root zone soil water conditions and plant water uptake are required to examine the water stress function. However, measuring soil water condition representing the whole root zone is not an easy task. A common way is to use buried sensors, such as Time-Domain Reflectometry (TDR), which is difficult to capture water condition of the whole root zone. For instance, the root system of a mature apple tree, in an arbitrary 2D profile of 3 m^2, occupies an area of 1 m^2 (Gong et al. 2006), while measurements with TDR cover only 10 cm^2 (Knight et al. 1995). Due to spatial variability of soil water condition, using a limited number of measurements is difficult to represent the whole root zone condition, especially for plants with a complex root system. (3) Burying soil moisture sensors may disturb soil structures and damage plant roots, which will affect root water uptake performance. The above listed difficulties may explain why most reported root water uptake experiments (e.g., Fujimaki et al. 2008) are conducted in laboratory. In these experiments, plants are growing in a limited soil column, which may not represent the natural conditions, especially for large trees.

As a result, the water stress function is often calibrated with the root-zone hydrological model (e.g., Guan et al. 2006). The uncertainty from estimation of vegetation function (water stress function) and of soil hydraulic properties is mixed, which increases the possibility of non-unique solutions.

In this study, rather than based on calibration of root-zone hydrological model, we designed a simple non-invasive field-based experiment to determine and parameterize water stress function. Studies (Richie and Hinckley 1975; Hinckley et al. 1978) have shown that before sunrise, water potential along the soil-plant continuum is in equilibrium with each other. Similarly, Richter (1997) found that the predawn plant water potential equates the "wettest" soil water potential accessed by roots. Meanwhile, studies (Jarvis 1989; Lai and Katul 2000) show that the plant roots have ability to adjust their uptake performance. Water uptake reduced in the stressed part of the root zone will be partially compensated by an increased uptake from the wetter part. Therefore, it is reasonable to assume that the predawn stem water potential (SWP) is a good surrogate for the root zone soil water potential to be used for examining the water stress function for root water uptake.

By measuring and estimating the stem water potential, plant actual transpiration and potential transpiration, we are able to examine and parameterize the water stress function. The water stress functions are fitted with observed data based on the least square criteria, and the F-statistics is used to test the significance of the correlation coefficients (Myers 1990).

Potential and actual transpiration: Potential transpiration (PT) calculated from TVET, and actual transpiration (T) based on sap flow measurements, for the whole experimental period is shown in Fig. 4.11. Transpiration rates of both trees are similar. For most time, except for the raining days, they are far below the potential transpiration rates, suggesting that both trees are under water stress for root water-uptake process.

Stem water potential: Fig. 4.12 gives an example of SWP measurements. Each day, SWP reaches its maximum value around 6:00 am (local standard time). Similar phenomenon is reported by Ritchie and Hinckley (1975). After sunrise, SWP decreases quickly with an increase of transpiration rate, and comes to its minimal value at around 2:00 pm. Then, it goes up quickly until sunset. After sunset, SWP increases gradually until the water potential within soil-plant system becomes equilibrium. In the following analysis, daily predawn SWP is selected from the continuous output of stem psychrometers around 6:00 am every day, and daily root zone soil water

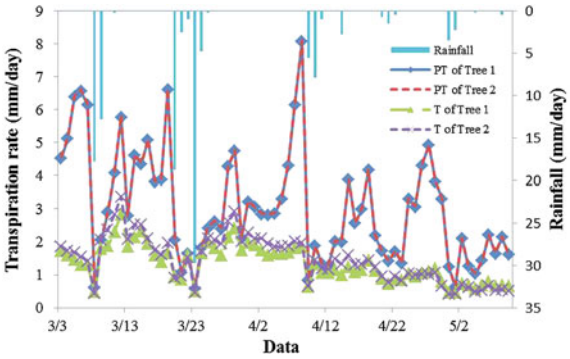

Fig. 4.11 Daily *PT*, actual transpiration (*T*) for both trees and precipitation during the experimental period (Yang et al. 2013)

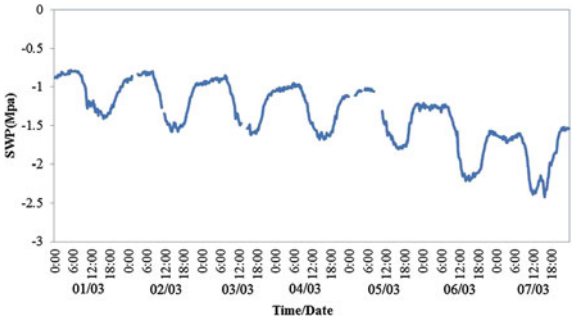

Fig. 4.12 Example of SWP measurements (tree 2, 1–7 March 2011) (Yang et al. 2013)

potential is calculated by averaging predawn SWP of a day and the next day to account for the slightly change in root zone soil water potential within 1 day.

For the whole week, there was not a rainfall event. The predawn SWP shows a decreased trend (Fig. 4.12), indicating that the root zone became drier and drier mainly due to evapotranspiration. This supports that the predawn SWP reflects the changes of root-zone soil water condition.

Figure 4.13 shows the changes of predawn SWP during the experimental period. Both trees show a good consistence, and stem water potential responses sensitively to the rainfall events. In the dry intervals between rainfall events, predawn SWP decreases primarily due to root zone water loss through evapotranspiration. This trend agrees well with the experimental and modeling studies of root zone soil water dynamics (e.g., Shang et al. 2004). In the following analysis, all data, except for those of rainy days, are used to examine and parameterize the water stress function (50 days in total). This is because a relative humidity of near 100 % occurs during rainy days, which precludes transpiration from the canopy (Granier 1987).

Parameterization of water stress function: Fig. 4.14 shows the relationship between predawn stem water potential and *T*/*PT* based on the field measurements. The data clouds of both trees are similar. Based on visual observation, they are different from the Feddes model piecewise linear shape, but more close to the S-shape model form. Thus the S-shape function is chosen for further analysis.

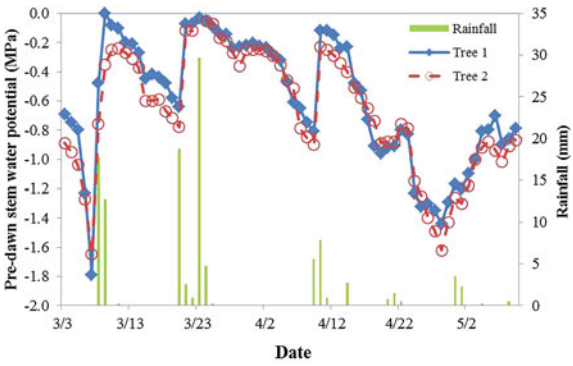

Fig. 4.13 Daily predawn SWP and precipitation for both trees during the experimental period (Yang et al. 2013)

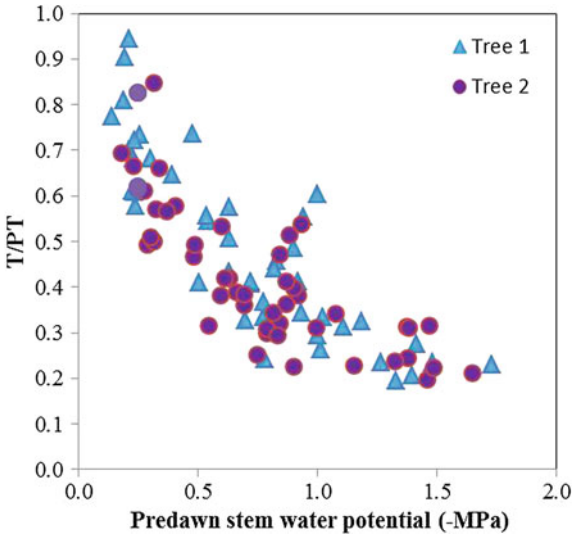

Fig. 4.14 Relationship between of root water uptake fraction (T/PT) against predawn SWP (Yang et al. 2013)

The S-shape model fits the observation data fairly well (Fig. 4.15), with a coefficient of determination (R^2) of 0.74 (n = 100, significance level < 0.01). Two parameters are −0.52 MPa for h_{50} and 1.04 for p, respectively. However, some data points (within the oval) greatly deviate from the fitted curve. This suggests that some factors, other than the soil water condition, also influence the root water-uptake. In a coupled soil-plant-atmosphere continuum model, these factors, such as vapor pressure deficit, solar radiation, and air temperature, are considered to calculate their stress effect (e.g., a Jarvis-type function). For a de-coupled model

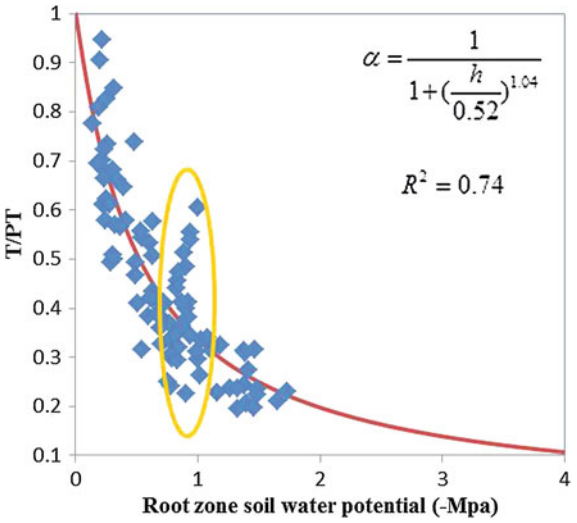

Fig. 4.15 Fitting result of the S-shape root water uptake function (Yang et al. 2013)

discussed in this paper, these factors are often not considered. Nevertheless, it is possible to lump these factors into the potential transpiration term, and incorporate it into the water stress function.

Similar idea can be found in Feddes et al. (1978) that plants in a day with a larger potential transpiration rate suffers a bigger water stress than in a day with a smaller potential transpiration rate, even if the soil water conditions are similar. This additional water stress is not due to a scant water supply, but a high atmospheric demand.

To examine the effect of potential transpiration on water stress function, the ratios of the measured water stress over the estimated water stress from the fitted curve against PT are plotted in Fig. 4.16. The points show a linear trend with an R^2 of 0.45 (n = 100, significance level < 0.01). This supports that the discrepancy between measurements and fitted curve in Fig. 4.15 is at least partially caused by different atmospheric demands.

In order to incorporate the effect of potential transpiration to the water stress function, it is assumed that the uptake water stress α is a function of both root-zone soil water potential and potential transpiration, i.e.,

$$\alpha(h, PT) = f(h) * g(PT) \tag{4.27}$$

where f is a S-shape function of root zone soil water potential, and g is a function of potential transpiration. Based on Fig. 4.16, where the ratio of $\alpha(h, PT)$ to $\alpha(h)$ is linearly correlated with PT, we assume that g is a linear function. Then the water stress function is expressed as,

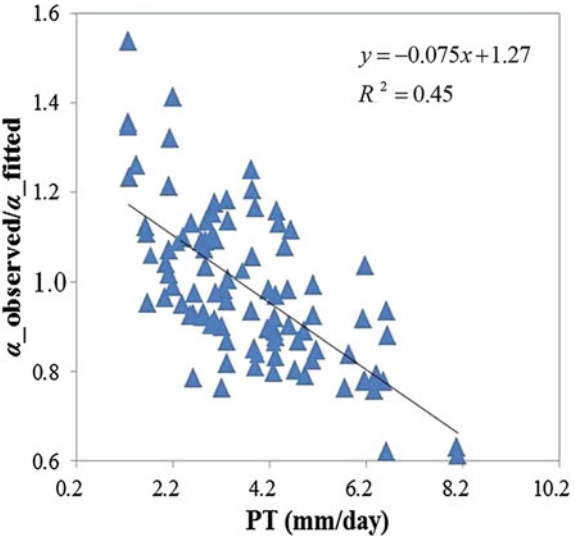

Fig. 4.16 Relationship between the ratio of observed water stress to that estimated with the fitted S-shape function and PT (Yang et al. 2013)

$$\alpha(h, PT) = \frac{1}{1 + (\frac{h}{h_{50}})^p} * (aPT + b) \tag{4.28}$$

where a and b are two parameters of the linear function. While the measured α value already includes the influences of both soil water condition and potential transpiration, it is difficult to parameterize $f(h)$ and $g(PT)$ separately using the observed α. Here, we use Matlab "surface fitting tool" to fit Eq. (4.28) with the data.

The fitting result of Eq. (4.28) is shown in Fig. 4.17, and four parameters are −0.49 MPa, 0.91, −0.084 (day/mm) and 1.25 for h_{50}, p, a and b, respectively. The coefficient of determination (R^2) of the fitted function is 0.85 (n = 100, significance level < 0.01), which means that the new water stress function with PT correction fits the data better than the sole S-Shape model. Besides, we find that the influence of potential transpiration on the water stress can be expressed as a linear function. This is in agreement with the potential transpiration dependent parameterization for the Feddes model in HYDRUS (Šimunek et al. 2005), in which two threshold soil water potentials (parameter h_3) are prescribed for two threshold potential transpiration rates. One is used for the high PT condition and the other applies for the low PT condition (Fig. 4.2a). A linear interpolation applies to estimate h_3 between the two threshold conditions. Our result indicates that the S-shape model used in HYDRUS can be improved to incorporate the PT effect. Including the PT effect in the water stress function is a compensation of the de-coupled approach, to include the micrometeorological effect on stomatal controls for transpiration.

As the result, the derived root water uptake model for the drooping sheoak is

$$T = \alpha(h, PT) * PT = \frac{1}{1 + (\frac{h}{0.49})^{0.91}} * (-0.084PT + 1.25) * PT \tag{4.29}$$

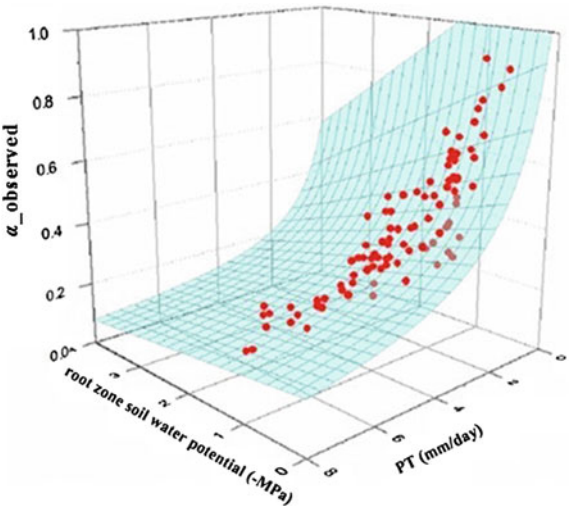

Fig. 4.17 Fitting result of water stress function with PT correction, based on Eq. (4.28) (Yang et al. 2013)

It should be noted that, because the data set is short (less than 3 months), the calibrated results have some uncertainties. Although the experimental period covers both a dry season (February–March) and a wet season (April–May), and measured predawn SWP covers the normal range of root zone soil water potential for most species (0 to −1.5 MPa) (e.g., Taylor and Ashcroft 1972), for the future work, it is always better to examine and parameterize the model based on a longer data set. Nonetheless, this study demonstrates a simple field-based experimental method useful to determine vegetation root water uptake functions.

The root distribution along the soil profile is described by using a power function model, in which the ratio of root length between layer i and layer $i + 1$ to the total root length is expressed as (Li et al. 2001),

$$RV_i = \frac{\ln[(1+e^{-bZ_i})/(1+e^{-bZ_{i+1}})] + 0.5(e^{-bZ_i} - e^{-bZ_{i+1}})}{\ln[2/(1+e^{-bl_r})] + 0.5\,(1-e^{-bl_r})} \tag{4.30}$$

$$b = \frac{24.66 RV_{10}{}^{1.59}}{l_r} \tag{4.31}$$

where l_r is root zone depth (taken to be 1 m); RV_{10} represents the proportion of roots within the upper 10 % soil layer, and is set to be 35 % according to previous studies.

Finally, by introducing Eqs. (4.30) and (4.31) into Eq. (4.22), one could get the root water uptake model for drooping sheoak.

4.4.3 Results and Discussion

To test the HDS-SPAC model performance in this site, we recalibrated the root water uptake model by using the Tree 1 data only (Eq. 4.32) and used the data from tree 2 to test the model (Table 4.3).

$$\alpha(h, PT) = \frac{1}{1 + (\frac{h}{0.44})^{0.81}} \times (-0.077PT + 1.26) \tag{4.32}$$

Comparison between estimated and observed soil water potential and between estimated and observed plant transpiration for tree 1 (water stress function was calibrated with Tree 1 data) are shown in Figs. 4.18 and 4.19, respectively.

Table 4.3 Soil water dynamic parameters during the simulation (Yang et al. 2013)

Parameter	α (m^{-1})	n	K_s (m day^{-1})	θ_s (cm^3 cm^{-3})	θ_r (cm^3 cm^{-3})
Value	1.5	1.4	0.41	0.46	0.1

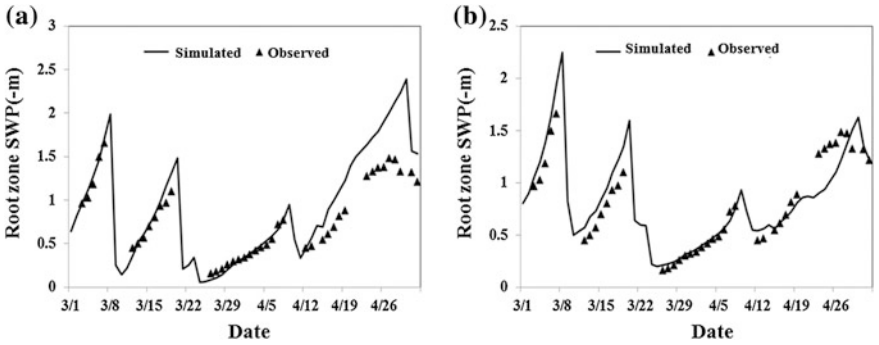

Fig. 4.18 Comparison between observed and estimate soil water potential for Tree 1. **a** Original S-shape model, **b** S-shape model after PT correction

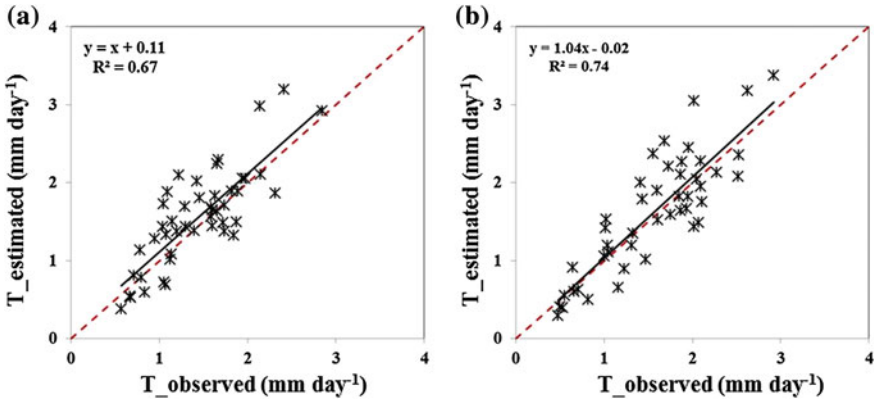

Fig. 4.19 Comparison between observed and estimate plant transpiration for Tree 1. **a** Original S-shape model, **b** S-shape model after PT correction

The results show that using the S-shape function after PT correction gave better soil water potential and plant transpiration estimates than using the original S-shape function. As a result, we only considered the corrected S-shape function in model validation on Tree 2 (Figs. 4.20 and 4.21). The results show a reasonable good agreement between estimates and observations in terms of both soil water potential and plant transpiration. The above results suggest that (1) the HDS-SPAC model can be well applied in nature forest ecosystem and (2) it is important to consider the effect of PT in modelling root water uptake.

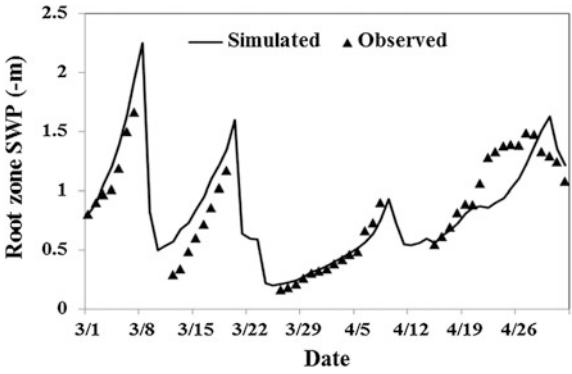

Fig. 4.20 Comparison between observed and estimate soil water potential for Tree 2

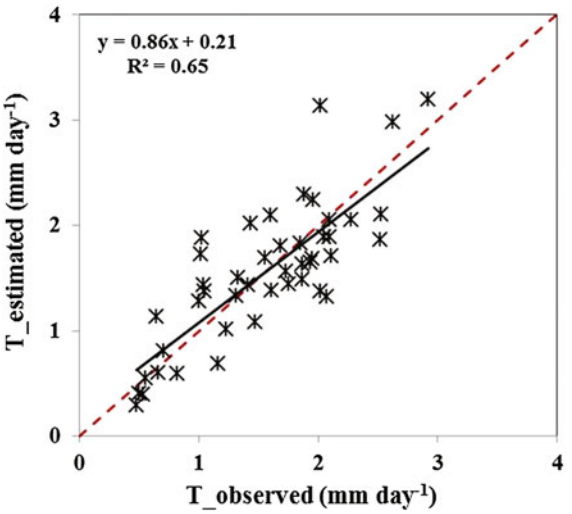

Fig. 4.21 Comparison between observed and estimate plant transpiration for Tree 2

4.5 Conclusion

In this chapter, a unidirectional soil-plant-atmosphere continuum model based on the hybrid dual-source approach for estimating actual evaporation and transpiration has been developed and applied in an agricultural ecosystem and a natural forest ecosystem, respectively. In addition, this chapter presents a new experimental method for direct water stress function testing and parameterization. The results show that:

(1) The HDS-SPAC model is able to correctly simulate soil moisture/temperature profiles and evapotranspiration, and capture effects of surface vegetation characteristics on quantifying actual evaporation and transpiration.

(2) The designed experimental method is capable in examining and parameterizing water stress functions, and the S-shape function is better than the Feddes function to fit for the data of drooping sheoak;
(3) The root water uptake water stress function is not only dependent of the soil moisture condition, but also of the atmospheric demand. After incorporating atmospheric demand into the S-shape water stress function, the performance of the HDS-SPAC model is improved.

References

Allen RG, Tasumi M, Morse A et al (2007) Satellite-based energy balance for mapping evapotranspiration with internalized calibration (METRIC)-applications. J Irrig Drain Syst 19:395–406

Allen RG, Pereira LS, Raes D, Smith M (1998) Crop evapotranspiration: Guidelines for computing crop water requirements. FAO Irrigation and Drainage Paper 56, Rome, p 300

Breshears DD, Ludwig JA (2009) Near-ground solar radiation along the grassland-forest continuum: tall-tree canopy architecture imposes only muted trends and heterogeneity. Austral Ecol 35:31–40

Celia MA, Bouloutas EF (1990) A general mass-conservative numerical solution for the unsaturated flow equation. Water Resour Res 26:1483–1489

Chung S-O, Horton R (1987) Soil heat and water flow with a partial surface mulch. Water Resour Res 23:2175–2186

Cong ZT (2003) Study on the coupling between the winter wheat growth and the water-heat transfer in soil-plant-atmosphere continuum. Dissertation for the doctoral degree, Tsinghua University, Beijing, p 112 (in Chinese)

Deardorff JW (1978) Efficient prediction of ground surface temperature and moisture with inclusion of a layer of vegetation. J Geophys Res 20:1889–1903

de Vries DA (1963) Thermal properties of soils. In: Van Wijk WR (ed) Physics of plant environment. North-Holland Publishing Company, Amsterdam

Dixon MA, Tyree MT (1984) A new stem hygrometer, corrected for temperature gradients and calibrated against the pressure bomb Plant. Cell Environ 7:693–697

Du Y, Wang J, Liu Z et al (2001) Water distribution and microclimate effects of sprinkler irrigation on spring wheat field. Chin J Appl Ecol 12:398–400

Edlefson N, Anderson A (1943) Thermodynamics of soil moisture. Hilgardia 15:31–298

Feddes R, Raats P (2004) Parameterizing the soil–water–plant root system. In: Feddes R, de Rooij G, van Dam J (eds). UR Frontis Series, Wageningen

Feddes RA, Kowalik PJ, Zaradny H (1978) Simulation of field water use and crop yield. Wiley, New York

Fujimaki H, Ando Y, Cui TB, Inoue M (2008) Parameter estimation of a root water uptake model under salinity stress. Vadose Zone J 7:31–38

Gong D, Kang S, Zhang L et al (2006) A two-dimensional model of root water uptake for single apple trees and its verification with sap flow and soil water content measurements. Agric Water Manag 83:119–129

Granier A (1987) Evaluation of transpiration in a Douglas-fir stand by means of sap flow measurements. Tree Physiol 3:309–320

Green S (2009) Measurements of sap flow by the heat-pulse method. An instruction manual for the HPV system. TranzFlo NZ Ltd, Palmerston North

Guan H, Wilson JL (2009) A hybrid dual-source model for potential evaporation and transpiration partitioning. J Hydrol 377:405–416

Guan H, Simunek J, Newman BD et al (2006) Modelling investigation of water partitioning at a semiarid ponderosa pine hillslope. Hydrol Process 24:1095–1105
Haverkamp R, Vauclin M, Vachaud G (1984) Error analysis in estimating soil water content from neutron probe measurements: 1. Local standpoint. Soil Sci 137:78–90
Hinckley TM, Lassoie JP, Running SW (1978) Temporal and spatial variations in the water status of forest trees. For Sci Monogr 20(1):a0001–z0001
Hough MN, Jones RJA (1997) The United Kingdom meteorological office rainfall and evaporation calculation system: MORECS version 2.0-an overview. Hydrol Earth Syst Sci 1:227–239
Jarvis NJ (1989) A simple empirical model of root water uptake. J Hydrol 107:57–72
Kang Y, Wang QG, Liu HJ (2005) Winter wheat canopy interception and its influence factors under sprinkler irrigation. Agric Water Manag 74:189–199
Knight JH, White I (1995) Sampling volume of TDR probes used for water content. In: Proceedings of the symposium on time domain reflectometry in environmental, infrastructure and mining applications, Statens-Planteavlsforsog
Krobel R, Sun QP, Ingwersen J et al (2010) Modelling water dynamics with DNDC and DAISY in a soil of the North China Plain: a comparative study. Environ Modell Softw 25:583–598
Kustas WP, Norman JM (1999) Evaluation of soil and vegetation heat flux predictions using a simple two-source model with radiometric temperatures for partial canopy cover. Agric For Meteorol 94:13–29
Lai CT, Katul G (2000) The dynamic role of root-water uptake in coupled potential to actual transpiration. Adv Water Resour 23:427–439
Lee DH, Abriola LM (1999) Use of the Richards equation in land surface parameterizations. J Geophys Res 104:27519–27526
Lee YH, Mahrt L (2004) Comparison of heat and moisture fluxes from a modified soil-plantatmosphere model with observations from BOREAS. J Geophys Res 109: D08103.1–D08103.9
Lei HM, Yang DW (2010) Interannual and seasonal variability in evapotranspiration and energy partitioning over an irrigated cropland in the North China Plain. Agric For Meteorol 150:581–589
Lei H, Yang D, Schymanski S et al (2008) Modeling the crop transpiration using an optimality-based approach. Sci China Ser E: Technol Sci 51:60–75
Li SG, Asanuma J, Kotani A, Davaa G, Oyunbaatar D (2007) Evapotranspiration from a Mongolian steppe under grazing and its environmental constraints. J Hydrol 333:133–143
Li KY, De Jong R, Boisvert J (2001) An exponential root-water-uptake model with water stress compensation. J Hydrol 252:189–204
Lin JD, Sun SF (1983) A study of moisture and heat transport in soil and the effect of resistance to evaporation. J Hydraul Eng 14:1–8 (in Chinese)
Liu CM, Zhang X, Zhang Y (2002) Determination of daily evaporation and evapotranspiration of winter and maize by large-scale weighting lysimeter and micro-lysimeter. Agric For Meteorol 111:109–120
Luo Y, Yu Q, Yang Z et al (2000) The evaluation of water uptakes models by using precise field observation data. J Hydraul Eng 31:73–80 (in Chinese)
Marshall D (1958) Measurement of sap flow in conifers by heat transport. Plant Physiol 33:385–396
Miao H, Chen S, Chen J et al (2009) Cultivation and grazing altered evapotranspiration and dynamics in Inner Mongolia steppes. Agric For Meteorol 149:1810–1819
Milly PCD (1982) Moisture and heat transport in hysteretic, inhomogeneous porous media: a matric heat-based formulation and a numerical model. Water Resour Res 18:489–498
Milly PCD (1984) A simulation analysis of thermal effects on evaporation from soil. Water Resour Res 20:1087–1098
Monteith JL (1965) Evaporation and environment. Symp. Soc Exp Biol 19:205–234
Mualem Y (1976) A new model for predicting the hydraulic conductivity of unsaturated porous media. Water Resour Res 12:513–522

Myers RH (1990) Classical and modern regression with application, the, 2nd edn. Duxbury/Thompson Learning, Belmont, p 488

Noilhan J, Planton S (1989) A simple parameterization of land surface processes for meteorological models. Mon Weather Rev 117:536–549

Philip HL, de Vries DA (1957) Moisture movement in porous materials under temperature gradients. Trans Am Geophys Union 38:222–232

Richter H (1997) Water relations of plants in the field: some comments on the measurement of selected parameters. J Exp Bot 48:1–7

Ritchie GA, Hinckley TM (1975) The pressure chamber as an instrument for ecological research. Adv Ecol Res 9:165–254

Sánchez JM, Kustas WP, Caselles V et al (2008) Modelling surface energy fluxes over maize using a two-source patch model and radiometric soil and canopy temperature observations. Remote Sens Environ 112:1130–1143

Shang SH, Li XC, Mao XM, Lei ZD (2004) Simulation of water dynamics and irrigation scheduling for winter wheat and maize in seasonal frost areas. Agric Water Manag 68:117–133

Šimunek J, van Genuchten MTh, Sejna M (2005) The HYDRUS-1D Software Package for Simulating the Onedimensional Movement of Water, Heat and Multiple Solutes in Variably-saturated Media, Version 3.0, HYDRUS Software Series 1. Department of Environmental Sciences, University of California, Riverside, p 240

Taconet O, Bernard R, Vidal-Madjar D (1986) Evapotranspiration over an agricultural region using a surface flux/temperature model based on NOAA-AVHRR data. J Climate Appl Meteorol 25:284–307

Taylor SA, Ashcroft GM (1972) Physical edaphology. Freeman and Co., San Francisco, pp 434–435

Tolk JA, Howell TA, Steiner JL et al (1995) Role of transpiration suppression by evaporation of intercepted water in improving irrigation efficiency. Irrig Sci 16:89–95

Tyree M, Yang S (1990) Water-storage capacity of Thuja, Tsuga and Acer stems measured by dehydration isotherms. Planta 182:420–426

van Dam JC, Feddes RA (2000) Numerical simulation of infiltration, evaporation and shallow groundwater levels with the Richards equation. J Hydrol 233:72–85

van Genuchten MT (1980) A closed-form equation for predicting the hydraulic conductivity of unsaturated soils. Soil Sci Soc Am J 44:892–898

van Genuchten MT (1987) A numerical model for water and solute movement in and below the root zone. U.S. Slainity Laboratory, USDA, ARS, Riverside

Wells CE, Eissenstadt DM (2003) Beyond the roots of young seedling: the influence of age and order on fine root physiology. J Plant Growth Regul 21:324–334

Wilson TB, Norman JM, Bland WL et al (2003) Evaluation of the importance of Lagrangian canopy turbulence formulations in a soil–plant–atmosphere model. Agric For Meteorol 115:51–69

Yang Y, Shang S, Guan H (2012) Development of a soil-plant-atmosphere continuum model (HDS-SPAC) based on hybrid dual-source approach and its verification in a wheat field. Sci China: Technol Sci 55:2671–2685

Yang Y, Guan H, Hutson J et al (2013) Examination and parameterization of the root water uptake model from stem water potential and sap flow measurements. Hydrol Process 27:2857–2863

Zhang XY (1999) Crop root and soil water use. China Meteorological Press, Beijing, p 186 (In Chinese)

Zhang YQ, Chen JM, Miller JR (2005) Determining digital hemispherical photograph exposure for leaf area index estimation. Agric For Meteorol 133:166–181

Chapter 5
A Hybrid Dual-Source Scheme and Trapezoid Framework Based Evapotranspiration Model (HTEM) Using Satellite Images

5.1 Introduction

Remote estimation of land surface evapotranspiration from satellite imagery is probably the only effective way to obtain detailed spatial and temporal ET patterns for large scales. After Brown and Rosenberg (1973) first used thermal remote sensing to retrieval surface fluxes, methods (or models) to quantify ET based on remote sensing developed rapidly (Bastiaanssen et al. 1998; Yan et al. 2012; Jiang and Islam 1999; Kustas and Norman 1997; Moran et al. 1994; Mu et al. 2011; Norman et al. 1995; Sánchez et al. 2008; Su 2002; Yang et al. 2012b). Among the various models that have been proposed, two-source models, which treat soil and vegetation as independent sources of the moisture flux, are generally considered to be an advancement of single-source models. Single-source models represent the surface as a single uniform layer and, therefore, may produce significant errors when applied to partially vegetated landscapes (Timmermans et al. 2007; Verhoef et al. 1997).

Two-source approaches require knowledge of the surface temperature of both soil and vegetation canopy, and this information is unattainable directly from satellite imagery because the land surface temperature (LST) observed by remote sensing is a single temperature over heterogeneous surfaces. The temperature difference between vegetation and soil components can be more than 20 °C (Kustas and Norman 1999). As a result, efforts have been made to decompose remotely sensed LST into component temperatures (canopy and soil). Norman et al. (1995) proposed a technique that uses the Priestly-Taylor relationship to estimate transpiration and canopy temperature. Soil temperature can then be estimated using the relationships between LST, fractional vegetation cover, and canopy temperature. Similar idea was adopted in Kustas and Norman (1999) and Sánchez et al. (2008). The difficulty in such an approach is the determination of the initial P-T coefficient. In Norman et al. (1995), the initial P-T coefficient was chosen to be 1.3; while in Kustas and Norman (1999), a value of 2 was found to be a better representative of

Y. Yang, *Evapotranspiration Over Heterogeneous Vegetated Surfaces*,
Springer Theses, DOI 10.1007/978-3-662-46173-0_5

this coefficient. Generally, the P-T coefficient is given approximately 1.26 over moist surfaces but much smaller for dry surfaces (Komatsu 2003).

Another operational way to determine component temperatures is based on the interpretation of the image (pixel) distribution in vegetation index (VI)/LST space. As reviewed by Carlson (2007), if a sufficiently large number of pixels are present and when contaminated pixels and outliers (e.g., clouds, surface water, sloping terrain and shading) are removed, the shape of the pixel envelope constitutes a meaningful triangle. Moran et al. (1994) claimed that the triangle space does not account for the effect of water stresses on canopy transpiration, and therefore replaced the triangle by using a trapezoid. In such a space, a higher VI value generally corresponds to a lower LST value for a pixel where higher evapotranspiration would occur and *vice versa*. More promisingly, isolines of surface soil wetness were found in the VI/LST space (Carlson 2007), representing constant soil water availability. Since radiometric temperature of the soil surface is mostly affected by the soil wetness and soil texture, and the latter remains relatively constant for a certain region, it is reasonable to assume that each soil wetness isoline representing the same soil surface temperature (Carlson 2007; Long and Singh 2012b; Nishida et al 2003).

Based on the trapezoidal VI/LST space and soil wetness isolines, Long and Singh (2012b) developed a two-source evapotranspiration model named TTME (Two-source Trapezoid Model for Evapotranspiration). However, one key assumption in TTME is that the aerodynamic resistances are equal over the whole domain. This assumption is also generally invoked in other triangle/trapezoid framework based ET models (Carlson and Ripley 1997; Carlson et al. 1994; Gillies et al. 1997; Jiang and Islam 1999, 2001, 2003; Jiang et al. 2009; Moran et al. 1994; Price 1990). These models infer evaporative fraction (EF, defined as the ratio of latent heat flux to available energy) without parameterizing the network of aerodynamic and surface resistances. As such, the effects of surface roughness and atmospheric stability are essentially ignored. Consequently, these models may work when surface roughness and LST are sufficiently uniform but will fail over more heterogeneous surfaces.

To overcome this weakness, it is important to combine the triangle/trapezoid framework with a resistance network. In this study, a new two-source evapotranspiration model is proposed to achieve this goal. The new model is based on the trapezoidal framework to decompose LST into component temperatures, and uses a dual-source modeling scheme to parameterize the resistance network and to estimate surface fluxes. Different from existing two-source models, which are either based on the "layer" approach (Kustas and Norman 1997; Shuttleworth and Wallace 1985) or the "patch" approach (Sánchez et al. 2008), a hybrid dual-source modeling scheme (Guan and Wilson 2009) is adopted in the new model. As discussed by Lhomme and Chehbouni (1999), both the layer approach and the patch approach are restricted to use within certain ranges of fractional vegetation cover: the layer model works better for uniform vegetated surfaces, while the patch model is more suitable for clumped vegetation. Besides, the layer model cannot tell the difference between under-canopy soil evaporation and inter-canopy soil evaporation, which may result in significant

modeling errors when being applied to surfaces with large soil moisture heterogeneity (e.g. partially irrigated cropland (Zhang et al. 2008)). The patch model assumes a full radiation loading for each component, and does not consider the attenuation of radiation by vegetation canopies. Therefore, evaporation from under-canopy soil surfaces is simply ignored in the patch model.

The hybrid scheme adopts the layer approach to partition available energy between components and uses the patch approach to calculate energy fluxes. As a result, both under- and inter-canopy soil evaporation are considered and distinguished. In Chap. 4, we coupled the hybrid scheme with a soil moisture/heat simulation component to simulate actual evaporation (E) and transpiration (T) processes over a wheat field and a natural forest ecosystem using ground based measurements. Results indicated that the hybrid model is capable in estimating actual ET and gives reasonable partitioning between E and T.

The objective of this study is to develop a new operational remote sensing ET model based on the hybrid dual-source modeling scheme and the trapezoid framework. Combining the two would achieve two goals: (1) to consider the surface aerodynamic characteristics in trapezoid model; (2) to incorporate remote sensing information into the hybrid dual-source modeling scheme. In the following sections, we will refer to it as the Hybrid dual-source scheme and Trapezoid framework based Evapotranspiration Model (HTEM).

5.2 Model Development

The HTEM consists of two modules. The first module is to partition the available energy for each component and to estimate the surface energy fluxes using a hybrid dual-source scheme. The second module is to decompose the bulk radiative land surface temperature into component temperatures based on a theoretically determined trapezoid framework.

5.2.1 Hybrid Dual-Source Scheme

The energy allocation and resistance network of the HTEM is shown in Fig. 2.1d. In the hybrid dual-source scheme, a layer approach is used to allocate the available energy for the soil and canopy component based on Beer's law:

$$A_c = R_n[1 - \exp(-k_c \mathrm{LAI})] \tag{5.1}$$

$$A_s = R_n[\exp(-k_c \mathrm{LAI})] \tag{5.2}$$

where A is the available energy per unit area (W m^{-2}), subscripts c and s represent canopy and soil components, respectively. k_c is the extinction coefficient of

radiation attenuation within the canopy, LAI is leaf area index (m^2 m^{-2}) and R_n is the net radiation (W m^{-2}), which is computed from,

$$R_n = (1 - \alpha)S_d + \varepsilon\sigma(\varepsilon_a T_a^4 - LST^4) \tag{5.3}$$

where S_d is the downwelling shortwave radiation (W m^{-2}), α is the surface albedo, σ is Stefen-Boltzmann constant (=5.67 × 10^{-8} W m^{-2} K^{-4}). T_a is air temperature and LST is the radiative land surface temperature observed by satellite remote sensing (K). ε is the emissivity of the bulk soil-canopy surface, and ε_a is the emissivity of the atmosphere, given by Brutsaert (1975),

$$\varepsilon_a = 1.24(e_a/T_a)^{1/7} \tag{5.4}$$

where e_a is vapor pressure in hPa.

Kustas and Norman (1999) reported that the exponential extinction of net radiation is only appropriate for canopy near full coverage and may produce systematic errors for sparse canopies, and proposed a physically-based algorithm for estimating the divergence of R_n in the canopy. However, this method requires detailed information on canopy and leaf configurations and needs separate evaluations of the visible and near-infrared albedos of the soil and vegetation, which may bring further uncertainties. In HTEM, a simple linear interpolation of the value of k_c between that for full vegetation cover and bare soil in terms of fractional vegetation coverage was conducted to obtain the k_c value over partially vegetated surfaces, as suggested by Zhang et al. (2008). The value of k_c for full vegetation cover is set to be 0.8 for maize, 0.7 for soybean and 0.63 for wheat following experimental studies by Lindquist et al. (2005), Sinclair and Horie (1989) and Thorne et al. (1988), respectively.

A patch approach is then used to partition available energy into the latent heat, sensible heat and ground heat fluxes. In the patch approach, energy fluxes of each component (canopy or soil) represents an average value per unit area of component under consideration, and the average values per unit ground area is weighted by the fractional coverage of each component,

$$A_c = F_r \times (LE_c + H_c) \tag{5.5}$$

$$A_s - G = (1 - F_r) \times (LE_s + H_s) \tag{5.6}$$

where G is ground heat flux, LE is the latent heat flux and H is the sensible heat flux. F_r is the fractional vegetation coverage, which is deduced from remote sensing by,

$$F_r = 1 - \left(\frac{\mathrm{NDVI}_{max} - \mathrm{NDVI}}{\mathrm{NDVI}_{max} - \mathrm{NDVI}_{min}}\right)^n \tag{5.7}$$

where NDVI_{max} is the NDVI for complete vegetation cover and NDVI_{min} is the NDVI for bare soil. The coefficient n is a function of leaf orientation distribution within the canopy, the value of which typically ranges between 0.6 and 1.25 (Li et al. 2005).

Ground heat flux (G) in HTEM is estimated from a semi-empirical equation provided by Bastiaanssen (2000),

$$G = R_n \times (LST - 273.16) \times (0.0038 + 0.0074\alpha)(1 - 0.98\mathrm{NDVI}^4) \quad (5.8)$$

For each component, the sensible heat flux is calculated by the classical Ohm's law type formulations,

$$H_c = \rho C_p \frac{T_c - T_a}{r_a^h} \quad (5.9)$$

$$H_s = \rho C_p \frac{T_s - T_a}{r_a^a + r_a^s} \quad (5.10)$$

where ρ is the air density (kg m^{-3}), C_p is the specific heat of air at constant pressure (J kg^{-1} K^{-1}). T_s and T_c are soil surface temperature and canopy temperature (K), respectively. r_a^h is the aerodynamic resistance to heat transfer between canopy and the reference height (m s^{-1}); r_a^a is the aerodynamic resistance to heat transfer between $Z_{om} + d$ (Z_{om} is the canopy roughness length for momentum transfer, and d is zero displacement height) and the reference height (m s^{-1}); r_a^s is the aerodynamic resistance to heat flow in the boundary layer immediately above the soil surface (m s^{-1}). The expressions to estimate these aerodynamic resistances can be found in the appendix of Sánchez et al. (2008).

As a result, the latent heat flux for each component is computed as a residual in Eqs. (5.5) and (5.6):

$$LE_c = \frac{A_c}{F_r} - \rho C_p \frac{T_c - T_a}{r_a^h} \quad (5.11)$$

$$LE_s = \frac{A_s - G}{1 - F_r} - \rho C_p \frac{T_s - T_a}{r_a^a + r_a^s} \quad (5.12)$$

For the whole surface, the total latent heat flux is calculated as the sum of fluxes from each component weighted by their relative area (Lhomme and Chehbouni 1999):

$$LE = F_r \times LE_c + (1 - F_r) \times LE_s \quad (5.13)$$

5.2.2 *Vegetation Index-Land Surface Temperature Trapezoidal Space*

In the hybrid dual-source scheme for evapotranspiration, soil surface temperature and canopy temperature are both required, while only the bulk surface temperature is available from remote sensing. Therefore, it is necessary to decompose the bulk

surface temperature into component temperatures, which was achieved based on a theoretically determined trapezoid framework (Long et al. 2012).

Theoretically, four critical points relating to four extreme conditions define a trapezoid (Fig. 5.1). Point A represents the driest bare soil with the highest surface temperature (T_s_max), point B represents the fully vegetated area with the highest water stresses. As a result, point A and point B constitute the warm edge of the trapezoid space, and it is further assumed that the evaporation rate on the warm edge is zero. Points C and D represent fully vegetated surface and bare soil surface without water stress, respectively. Evaporation on the cold edge CD is assumed to be equal to the potential evaporation rate.

Prior studies have indicated that there exist soil wetness isolines within the F_r/LST space (Carlson 2007; Sandholt et al. 2002). Assuming a uniform texture, the soil radiometric temperature depends solely on the soil's moisture content; based on this, it is assumed that soil sharing the same moisture content is also isothermal (Fig. 5.1). The slope of each isoline is derived by interpolating the slope of the warm edge ($\beta_w = T_c$_max $- T_s$_max) and that of the cold edge ($\beta_c = 0$), in terms of temperature difference between the pixel and cold edge (a) and the temperature difference between the pixel and warm edge (b) (Fig. 5.1). Then, the soil surface temperature can be computed from,

$$T_s = F_r \times \frac{a}{a+b}(T_s\_\max - T_c\_\max) + LST \tag{5.14}$$

$$a = LST - T_a \tag{5.15}$$

$$b = (1 - F_r)(T_s\_\max - T_c\_\max) + T_c\_\max - LST \tag{5.16}$$

Once the soil surface temperature has been determined, the canopy temperature can be estimated from (Sánchez et al. 2008):

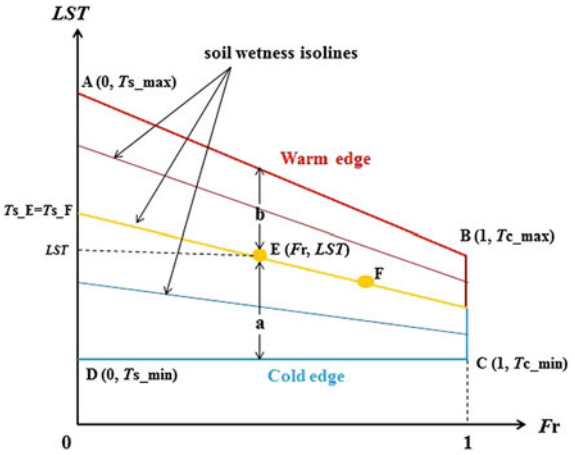

Fig. 5.1 A sketch of the trapezoidal F_r/LST space in the HTEM (Yang and Shang 2013)

$$T_c = \left\{ \frac{\varepsilon LST^4 - (1 - F_r)\varepsilon_s T_s^4}{F_r \varepsilon_c} \right\}^{1/4} \tag{5.17}$$

where ε_s and ε_c are emissivity of the soil surface and canopy surface, respectively.

To determine the shape of the trapezoid space, surface temperatures for the four extreme points should be accurately determined. In HTEM, the algorithm proposed by Long et al. (2012) is adopted to derive the theoretical boundaries of the trapezoid space for the given meteorological conditions and surface characteristics.

For the cold edge, the largest evaporation rate corresponds to the lowest sensible heat flux. As a result, spatially averaged air temperature (T_a) is taken to be the horizontal cold edge. For the two extreme points on the warm edge, their temperatures are theoretically determined through solving the surface radiation budget and energy balance equations (Long et al. 2012). As a result, temperatures for point A (T_s_max) and point B (T_c_max) are computed from [a detailed derivation can be found in Long et al. (2012)]:

$$T_s\_\text{max} = \frac{R_{s,0}}{4\varepsilon_s \sigma T_a^3 + \rho C_p / [0.75(r_a^a + r_a^s)]} + T_a \tag{5.18}$$

$$T_c\_\text{max} = \frac{R_{c,0}}{4\varepsilon_c \sigma T_a^3 + \rho C_p / r_a^c} + T_a \tag{5.19}$$

$$R_{s,0} = (1 - \alpha_s\_\text{max}) S_d + \varepsilon_s \varepsilon_a T_a^4 - \varepsilon_s \sigma T_a^4 \tag{5.20}$$

$$R_{c,0} = (1 - \alpha_c\_\text{max}) S_d + \varepsilon_c \varepsilon_a T_a^4 - \varepsilon_c \sigma T_a^4 \tag{5.21}$$

where α_s_max and α_c_max are surface albedo for the two extreme points, and can be estimated by extending the upper envelope of the F_r/albedo space intersecting with $F_r = 0$ and $F_r = 1$, respectively (Long and Singh 2012a; Zhang et al. 2005). It is noticed that the vegetation height for point B (h_c_max) is arbitrarily taken to be 1 m. However, sensitivity analysis in Sect. 5.2 suggests that estimated *LE* is not sensitive to the changes in h_c_max.

5.3 Model Validation at SMACEX (USA)

5.3.1 Site and Data

Site Description: During the period from 15 June (DOY 166) through 8 July (DOY 189), the Soil Moisture-Atmosphere Coupling Experiment (SMACEX) campaign was conducted in the central Iowa (N41.87°–N42.05°, W-93.83°–W-93.39°), U.S. (Fig. 5.2). The region can be classified as humid, with a mean annual precipitation of about 835 mm. More than 80 % of the land cover within the region was comprised of

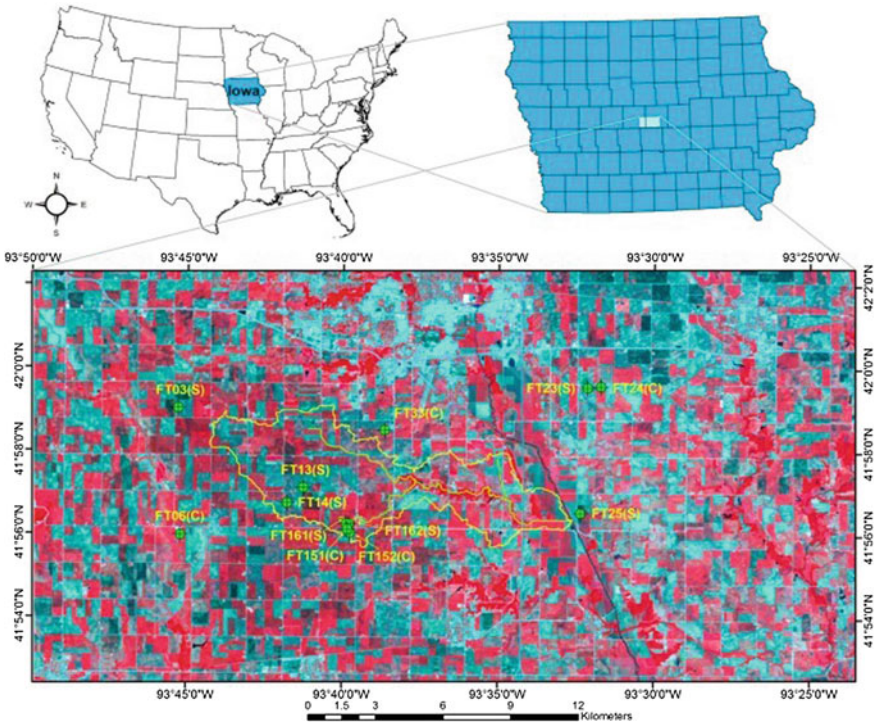

Fig. 5.2 Location of the SMACEX site with the false color composite of Landsat TM imagery acquired on June 23 (DOY 174), 2002. The *yellow line* indicates the main Walnut Creek, and the 12 flux towers are shown in numbered *green circles* nested with cross wires, with the crop type (i.e., soybean (S) or corn (C)) (Yang and Shang 2013)

rainfed corn and soybean fields. The campaign collected an extensive measurement set including metrological data from fourteen observation towers, soil and vegetation parameters and energy fluxes. Twelve of meteorological towers were equipped with eddy covariance (EC) systems, and the Bowen ratio method was employed to perform the energy closure of the EC system according to Twine et al. (2000) and Anderson et al. (2005). Anderson et al. (2005) reported that the observed energy fluxes after forcing with Bowen ratio method agreed well with aircraft counterparts for the SMACEX site; the root mean square difference between the two measurements are 10 W m^{-2} for sensible heat and 30 W m^{-2} for latent heat. This suggests that the EC measurements are reasonably representative of the actual surface fluxes at the site. Detailed descriptions of the measurement during the campaign are provided in (Kustas et al. 2005).

Remote Sensing and DEM Data: Three cloud-free Landsat TM/ETM+ scenes were taken during the SMACEX campaign period. These are available from the U.S.Geological Survey data center (http://glovis.usgs.gov/) and consist of the Landsat TM image acquired at 10:29 a.m. on DOY 174, the Landsat ETM+ image

acquired at 10:42 a.m. on DOY 182 and the Landsat ETM+ image acquired at 10:48 a.m. on DOY 189. A digital elevation map of the study area with a spatial resolution of 1 arc sec (about 30 m) was obtained from the National Elevation Dataset (http://seamless.usgs.gov/).

Variable Derivation: *LST* was derived from the infrared band (TIR, band 6) of Landsat TM/ETM+ images using a method specifically for the SMACEX site described in Li et al. (2004). Albedo was retrieved from the visible and near-infrared bands (band 1–5, 7) of the Landsat images following Allen et al. (2007). F_r was calculated using Eq. (5.7) with the coefficient n of 0.625, and $NDVI_{max}$ of 0.94 and $NDVI_{min}$ of 0 (Li et al. 2004). Leaf area index (LAI) and vegetation height (h_c) were estimated using empirical relationships for the SMACEX site given by Anderson et al. (2004),

$$\mathrm{LAI} = (2.88 \times \mathrm{NDWI} + 1.14)[1 + 0.104\exp(4.1 \times \mathrm{NDWI})] \text{ for both corn and soybean} \quad (5.22)$$

$$h_c = (1.2 \times \mathrm{NDWI} + 0.6)[1 + 0.04\exp(5.3 \times \mathrm{NDWI})] \text{ for corn} \quad (5.23)$$

$$h_c = (0.5 \times \mathrm{NDWI} + 0.26)[1 + 0.005\exp(4.5 \times \mathrm{NDWI})] \text{ for soybean} \quad (5.24)$$

where NDWI is the Normalized Difference Water Index, computed from near infrared (NIR, band 4 of TM/ETM+ images) and shortwave infrared (SWIR, band 5 of TM/ETM+ images) reflectances,

$$\mathrm{NDWI} = (\mathrm{NIR} - \mathrm{SWIR})/(\mathrm{NIR} + \mathrm{SWIR}) \quad (5.25)$$

5.3.2 Results

5.3.2.1 Validation at Flux Sites

For comparison with observations from the tower network, fluxes estimates were averaged over an estimated upwind source-area (1–2 pixels/$\sim$120 m) for each flux tower (Choi et al. 2009; Gonzalez-Dugo et al. 2009; Long and Singh 2012b). Besides, all fluxes and meteorological measurements were linearly interpolated to the time of satellite overpass using the two bounding measurements.

Comparisons between energy balance components (R_n, G, H and LE) produced by the HTEM with TM/ETM+ data and those from tower-based measurements for all 3 days (DOY 174, DOY182 and DOY 189) are shown in Fig. 5.3. Generally, all four energy components estimated from the HTEM agree reasonably well with flux tower-based measurements. Estimated R_n has a root mean square error (RMSE) of 19.1 W m^{-2} and a bias (defined as mean simulated value minus mean observed value) of 4.6 W m^{-2} (Table 5.1). The mean absolute percentage error (MAPE, defined as the ratio of mean absolute error to mean observed value) of R_n estimates for the 3 days is

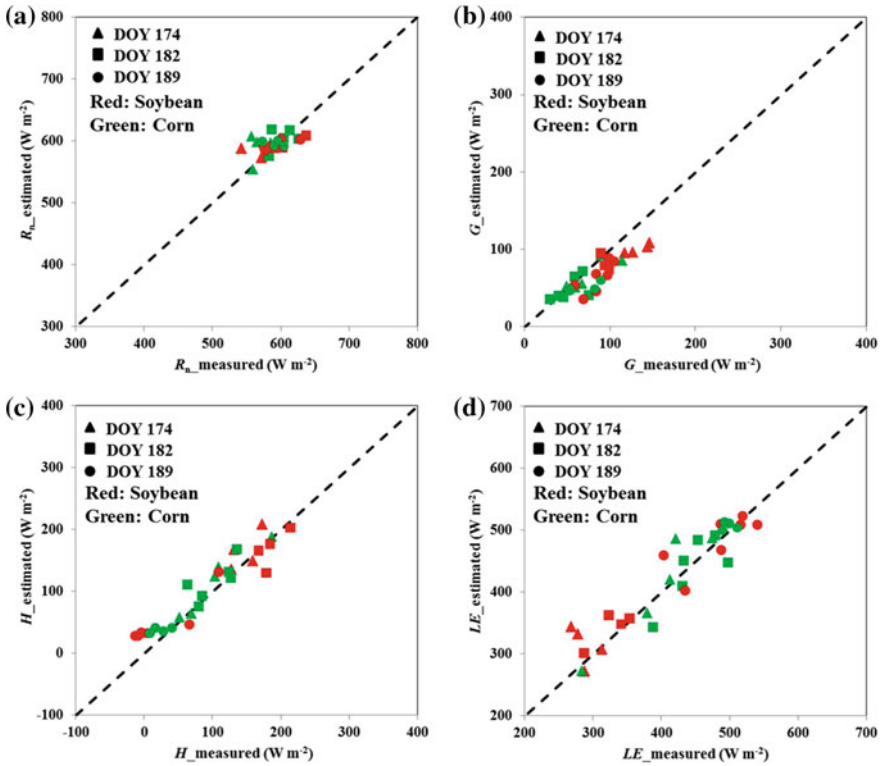

Fig. 5.3 Comparison of R_n (**a**), G (**b**), H (**c**) and LE (**d**) from HTEM using Landsat TM/ETM+ images with corresponding tower-based flux measurements at the SMACEX site on DOY 174, 182 and 189 in 2002 (Yang and Shang 2013)

2.4 %. The estimated ground heat flux (G) had an RMSE of 21.6 W m^{-2} and MAPE of 19.7 %. However, as can be seen from Fig. 5.3b, the accuracy of G estimates is systematically lower in soybean field than in the corn field. This is possibly due to the semi-empirical equation for G (Eq. 5.8), which was derived in Gediz Basin, Turkey (Bastiaanssen 2000) and may require local calibration.

The estimated sensible heat flux (H) has an RMSE of 25.1 W m^{-2} and a bias of 12.88 W m^{-2} (Table 5.1). The MAPE of estimated H for all 3 days was 100 % due to an extremely high MAPE value of 262 % on DOY 189 (Table 5.1). In DOY 189, five flux sites showed negative measured H, which indicates strong advection. However, as the lower limit of surface temperature for both canopy and soil were bounded above the air temperature in the trapezoid framework, the advection effect is not considered in the HTEM. Besides, studies have shown that advective conditions can greatly enhance measurement uncertainty of the EC system (e.g., Alfieri et al. 2011). The high MAPE on DOY 189 is exacerbated by the fact that these negative measured values were small, and even though the MAPE was high on DOY 189 the RMSE for that day was 28.1 W m^{-2}, which accounts for only

Table 5.1 A summary of the statistics of the HTEM performances at the SMACEX site

Energy component	DOY[a]	$\bar{o}$ (W m^{-2})	$\bar{s}$ (W m^{-2})	Bias (W m^{-2})	RMSE (W m^{-2})	MAPE (%)
R_n	174 (9)	573.1	586.8	13.7	26.2	3.3
	182 (10)	604.8	600.1	−4.7	16.3	2.0
	189 (11)	591	595.2	4.2	14.0	2.0
	Overall (30)	**589.7**	**594.3**	**4.6**	**19.1**	**2.4**
G	174 (9)	101.3	82.8	−18.5	24.3	17.9
	182 (10)	70.1	62.5	−7.6	15.7	16.2
	189 (11)	79.3	59.2	−20.1	23.7	24.4
	Overall (30)	**82.9**	**67.4**	**−15.5**	**21.6**	**19.7**
H	174 (9)	123.5	137.9	14.4	21.9	14.5
	182 (10)	135.9	137.6	1.7	24.5	16.1
	189 (11)	22.4	44.2	21.8	28.1	262.0
	Overall (30)	**90.6**	**103.4**	**12.8**	**25.1**	**100.0**
LE	174 (9)	348.3	366.1	17.8	39.2	9.1
	182 (10)	398.8	400.0	1.2	28.6	6.1
	189 (11)	489.3	491.8	2.5	25.1	4.1
	Overall (30)	**416.2**	**423.5**	**7.2**	**31.1**	**6.4**

$\bar{o}$ is the mean of observed values and $\bar{s}$ is the mean of HTEM simulated values (Yang and Shang 2013)

[a]Number in the bracket indicates the available number of measurement on each day

4.7 % of the total available energy. On the other 2 days, the H MAPE was better: 14.5 %. on DOY 174 and 16.1 % on DOY 182; these and the daily RMSE values are listed in Table 5.1.

LE is computed by the HTEM as the residual of the surface energy balance equation, and these estimates agree well with tower-based measurements (Fig. 5.3d). The RMSE of LE for all 3 days was 31.1 W m^{-2} and the bias was 7.2 W m^{-2}; the MAPE was 6.4 % (Table 5.1). Although a high MAPE of H is found in DOY 189, the MAPE of LE for that day is only 4.1 % since the true measured value was not close to zero. The RMSE on DOY 189 was 25.1 W m^{-2}, indicating that errors in estimated H are somehow compensated by errors in other two energy component (R_n and G). The highest RMSE of estimated LE occurred in DOY 174 with a value of 39.2 W m^{-2} because of a high RMSE for G on that day, which was further due to a relative large disagreement between estimated G and measured G in two soybean fields (the two red triangles in the very upper-right part of the data clouds in Fig. 5.3b). As a result, a negative bias of G of −18.5 W m^{-2} resulted in a positive bias of LE of 17.8 W m^{-2} on DOY 174. For DOY 182, the estimated LE showed an RMSE of 28.6 W m^{-2}, the bias and MAPD are 1.2 W m^{-2} and 6.1 %, respectively (Table 5.1).

5.3.2.2 Spatial Distribution of Estimated LE from HTEM

The spatial distribution of estimated canopy transpiration (LE_c) and soil evaporation (LE_s) on 3 days together with the corresponding NDVI maps are shown in Fig. 5.4. Generally, a higher NDVI value corresponds to higher LE_c for all 3 days, while LE_s is negatively correlated with NDVI. This phenomenon can be seen from two perspectives. On the one hand, for each day, LE_c is higher and LE_s is lower where there is a higher value of NDVI. An example of the relationships between NDVI and two component fluxes (*LE*s and *LE*c) on DOY 174 are shown in Fig. 5.5. A positive

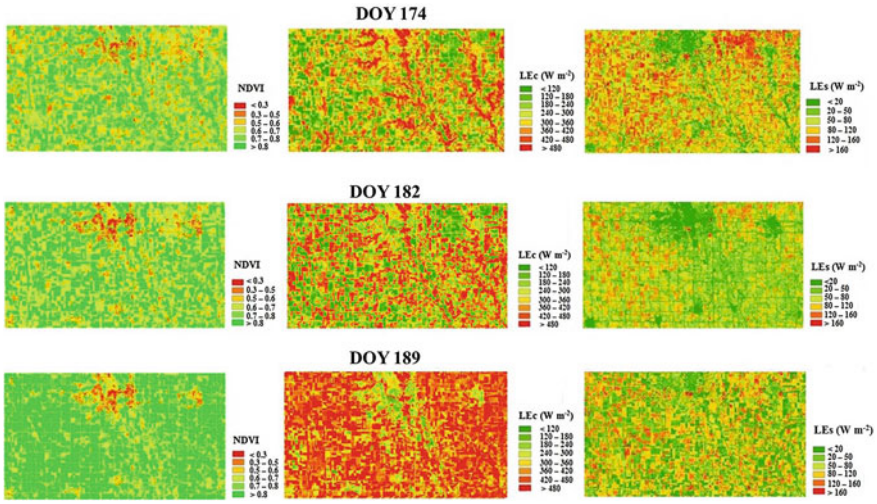

Fig. 5.4 Spatial distributions of NDVI, canopy transpiration (LE_c) and soil evaporation (LE_s) produced by the HTEM on 3 days (Yang and Shang 2013)

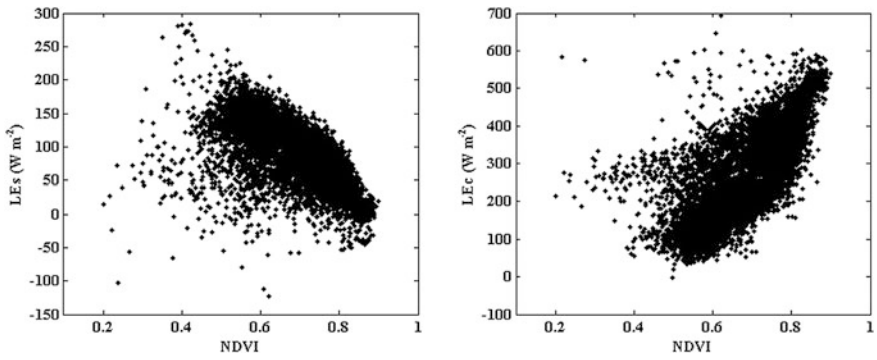

Fig. 5.5 Relationship between NDVI and LE_s(LE_c) on DOY 174 (Yang and Shang 2013)

relationship is clearly seen between NDVI and *LE*c, and a negative relationship is found between NDVI and *LE*s. On the other hand, the overall NDVI was increasing through DOY 174–189, which resulted an increasing in overall LE_c and decreasing in overall LE_s from DOY 174–189 (a relative high LE_s was observed in DOY 189 due a rainfall event 3 days before) (Fig. 5.4).

On DOY 174, when NDVI and soil moisture had the widest ranges within the study area, the estimated LE_c and LE_s showed the largest variations across the whole domain (Fig. 5.4). The coefficient of variation (CV) is 0.41 and 0.47 for LE_c and LE_s on DOY 174, respectively. On the contrary, on DOY 189, NDVI reached its maximum value for most pixels and soil moisture was relatively constant across the region due to the rainfall event in DOY 185. As a result, both LE_c and LE_s on DOY 189 showed the smallest spatial variations throughout the region among 3 days (Fig. 5.4) (CV values on these 2 days are: 0.26 for LE_c and 0.32 for LE_s on DOY 182, and 0.22 for LE_c and 0.18 for LE_s on DOY 189). These results are consistent with those reported by Choi et al. (2009), Long and Singh (2012b).

5.3.3 Comparison with Other Models

Extensive validation and intercomparison studies of remote sensing-based evapotranspiration models have been conducted using the SMACEX data (e.g., Choi et al. 2009; Li et al. 2005; Long and Singh 2012a, b). Figure 5.6 shows the comparison of statistics of the discrepancies between surface flux retrievals and flux tower measurements from published studies and the present study. The main features of each model and the remote sensing data being used in each study are summarized in Table 5.2.

As can be seen from Fig. 5.6, the performances of the HTEM model in estimating *H* and *LE* are generally better than all other models in terms of both RMSE and bias with reference to tower-based measurements. The RMSE and bias of HTEM-estimated R_n and *G* lie in the ranges of those found in other models. The comparison between HTEM and TTME could be a convincing evidence of the importance of considering the surface aerodynamic characteristics in the trapezoid model, as the major difference between the two models is whether a resistance network was incorporated in the trapezoidal F_r/LST space or not. Although the SMACEX site is relative homogeneous landscape (dominate by crops), the comparison result does show a better *H* and *LE* estimates from the HTEM than those from TTME.

As for other models, SEBAL (Surface Energy Balance Algorithm for Land) showed a comparable performance with other two-source models (i.e., TTME and TSEB), with an RMSE of *LE* about 50 W m^{-2} in both of its applications ((1) in Long and Singh (2012a), and (2) in Choi et al. (2009)), while the bias from SEBAL is on a magnitude of $\sim$10 W m^{-2} but differs in direction between the two applications; this could possibility due to a different selection of hot and cold pixels between applications. Long and Singh (2012a) modified SEBAL by introducing the

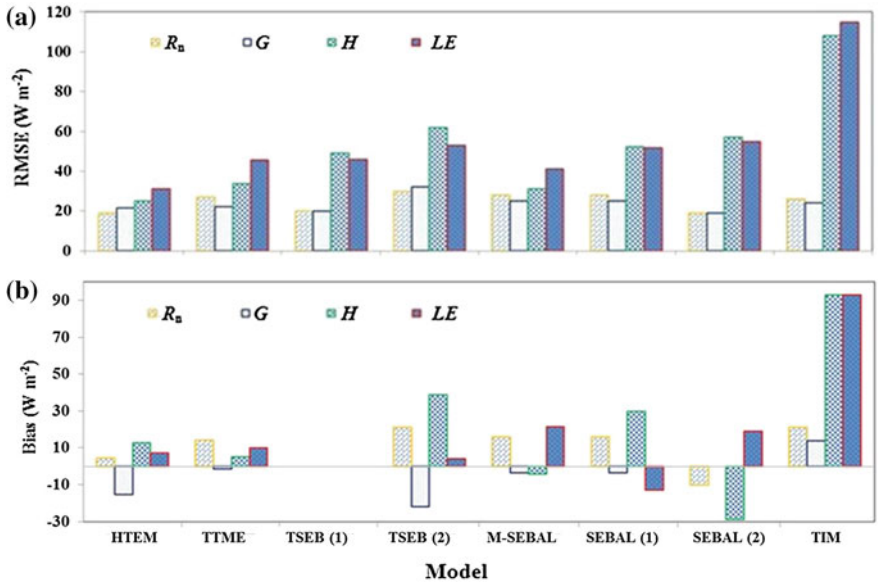

Fig. 5.6 Comparison of model performance in regarding to RMSE (**a**) and Bias (**b**) among HTEM and other models [TTME (long and Singh 2012b); TSEB(1) (Choi et al. 2009); TSEB(2) (Li et al. 2005); M-SEBAL (Long and Singh 2012a); SEBAL(1) (Choi et al. 2009); SEBAL(2) (Long and Singh 2012a); TIM (Choi, et al. 2009)] (Yang and Shang 2013)

trapezoid framework to avoid the subjectivity in selecting extreme points. The modified SEBAL model performed better than its ancestor with an RSME of 41.1 W m^{-2} and a bias of −4.4 W m^{-2} in estimated *LE*. In the two applications of TSEB model ((1) in Li et al. (2005), and (2) in Choi et al. (2009)), the initial Priestley-Taylor (P-T) coefficient was respectively set to be 1.3 and 1.26 for the whole study area, including both stressed and unstressed natural vegetation and crops. However, theoretically, the P-T coefficient should be a function of vegetation type and density, soil water status and vapor pressure deficit (Agam et al. 2010). A P-T coefficient larger than 1.26 typically represents unstressed full coverage conditions. Hence, TSEB has a tendency to overestimate LE under less soil wetness and larger drying power of air conditions (Agam et al. 2010; Choi et al. 2009; Fisher et al. 2008; Kustas and Norman 1999; Long and Singh 2012b).

5.3.4 Sensitivity Analysis

A local sensitivity analysis was conducted to examine how the uncertainties in the HTEM estimated *LE* can be apportioned to different sources of uncertainty in the model input. The sensitivity to the *i*th forcing variable or parameter is assessed by

Table 5.2 Main characteristics of models used for comparison in this study

Model	One/two source	LST decomposition	Resistance network	Satellite imagery	Closure technique	Studies
HTEM	Two	Trapezoid framework	Yes	Landsat TM/ETM+	BR	In SMACEX site
				MODIS Terra	RE	In Weishan site
TTME	Two	Trapezoid framework	No	Landsat TM/ETM+	BR	Long and Singh (2012b)
TSEB	Two	P-T approximation	Yes	Landsat TM/ETM+	BR	Choi et al. (2009)
				Landsat TM/ETM+	BR	Li et al. (2005)
M-SEBAL	One	-	Yes	Landsat TM/ETM+	BR	Long and Singh (2012a)
SEBAL	One	-	Yes	Landsat TM/ETM+	BR	Choi et al. (2009)
				Landsat TM/ETM+	BR	Long and Singh (2012a)
TIM	One	-	No	Landsat TM/ETM+	BR	Choi et al. (2009)
SEBS	One	-	Yes	MODIS Terra	RE	Yang et al. (2010)

Closure techniques include Bowen ratio (BR) and residual (RE) methods. Hyphen (-) indicates that the corresponding model do not need LST decomposition (Yang and Shang 2013)

calculating *LE* with a set of baseline parameters (LE_0) and comparing this with *LE* calculated by varying the *i*th parameter ($LE_{\pm}$); the sensitivity index is:

$$S_i = \frac{LE_{\pm} - LE_0}{LE_0} \times 100\% \tag{5.26}$$

The variation ranges and steps of each input variable are set the same as those in Long and Singh (2012b), which are 2 K for temperature variables with a step of 0.5 K and 20 % for other variables with a step of 5 %. As suggested by Long and Singh (2012b), the sensitivity analysis was conducted using the data from the SMACEX site on DOY 174, which showed wider range of soil moisture and vegetation coverage conditions. For DOY 182 and 189 in SMACEX site, the soil moisture and vegetation coverage had less variability, which resulted in conservative estimates of sensitivity.

As shown in Fig. 5.7, *LE* is most sensitive to changes in temperature variables. The estimated *LE* showed positive correlations with T_a but negative correlations with *LST* (Fig. 5.7a). An increase of 2 K in *LST* and T_a resulted in 23.2 % decrease and 15.3 % increase in estimated *LE*, while a 2 K decrease in *LST* and T_a could lead to 17.3 % increase and 21 % decrease in *LE* estimates, respectively (Table 5.3). However, compared with the TTME model, which is also based on the theoretical

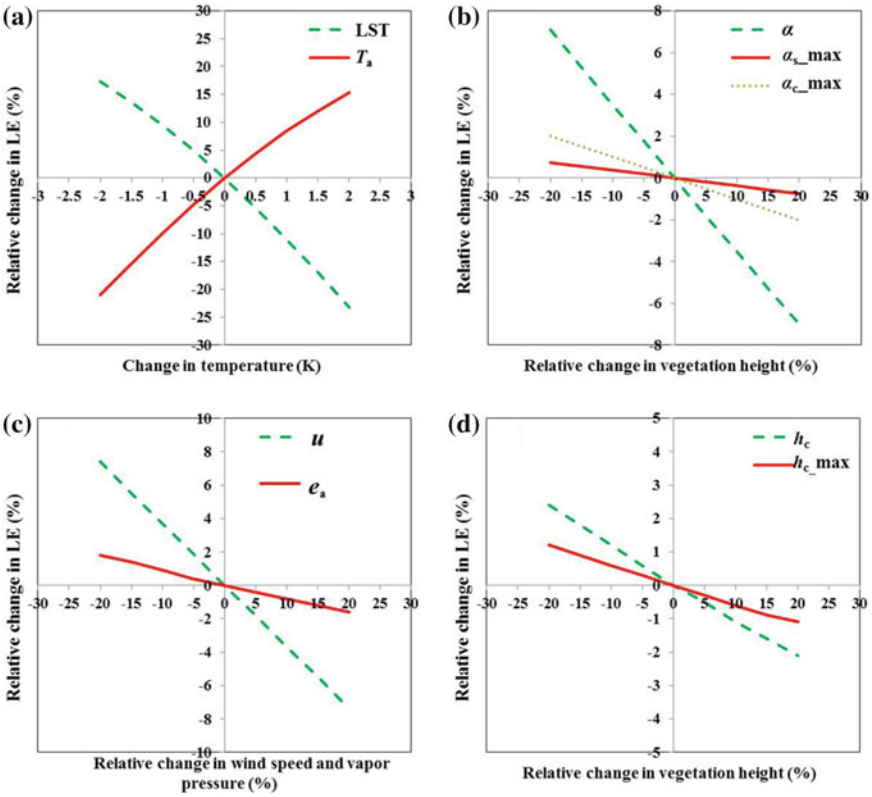

Fig. 5.7 Sensitivity analysis of HTEM to *LST* and T_a in (**a**), α, α_c_max and α_s_max in (**b**), u and e_a in (**c**), h_c and h_c _max in (**d**) (Yang and Shang 2013)

Table 5.3 Relative sensitivity of estimated LE from the HTEM to input variable at the SMACEX site on DOY 174 (Yang and Shang 2013)

Variation (%/K)	−20 (−2)	−15 (−1.5)	−10 (−1)	−5 (−0.5)	5 (0.5)	10 (1)	15 (1.5)	20 (2)
LST	17.3	13.6	9.5	5	−5.4	−11	−17	−23.2
T_a	−21	−15.4	−10	−4.8	4.3	8.5	12.1	15.3
α	7.1	5.3	3.5	1.8	−1.8	−3.5	−5.3	−7.0
α_c_max	0.73	0.54	0.38	0.19	−0.19	−0.38	−0.57	−0.75
α_s_max	2.02	1.52	1.01	0.51	−0.51	−1.02	−1.53	−2.04
u	7.4	5.5	3.7	1.9	−1.8	−3.7	−5.5	−7.4
e_a	1.8	1.4	0.9	0.4	−0.4	−0.8	−1.2	−1.6
h_c	2.4	1.8	1.2	0.6	−0.5	−1.1	−1.6	−2.1
h_c_max	1.2	0.9	0.6	0.3	−0.3	−0.6	−0.8	−1.1

trapezoid, the HTEM showed less sensitivity to temperatures. Long and Singh (2012b) reported that a 2 K increase in *LST* and T_a would respectively result in 28.6 % decrease and 27.6 % increase in estimated *LE* from the TTME model.

The surface albedo plays a fundamental role in determining the total available energy, and *LE* is sensitive to changes in albedo. A 20 % increase in α would result in a 7 % decrease in *LE*. However, the changes in albedo of two extreme surfaces (Eqs. 5.18–5.21) have insubstantial effect on the final estimation of *LE* (Table 5.3). Therefore, even if the process of determining α_c_max and α_s_max suffers certain subjectivities, it will not greatly affect the accuracy of *LE* estimates.

For other input variables, results indicate that wind speed (u), e_a and h_c are all negatively correlated with *LE* estimates. A 20 % increase in u, e_a and h_c would result in a 7.4, 1.6 and 2.1 % decrease in *LE* estimates, respectively. The reason why *LE* and u are negatively correlated is that an increase in u would lead to decreases in aerodynamic resistances and thus decrease in both T_s_max and T_a_max (Eqs. 5.18 and 5.19), which is indicative of the warm edge moving downwards and therefore result in less latent heat flux. Moreover, it is shown that the hypothesized vegetation height for the theoretical fully vegetated surface with largest water stresses (h_c_max) would not result in large uncertainty in the model.

5.4 Model Validation at Weishan (China)

5.4.1 Site and Data

Site Description: The second validation study uses data from the Weishan flux site (N36.65°, E116.05°) located in the center of the Weishan Irrigation District along the lower reaches of the Yellow River (Fig. 5.8), China. The elevation of the site is 30 m above the sea level, and it is characterized by sub-humid climate with a mean

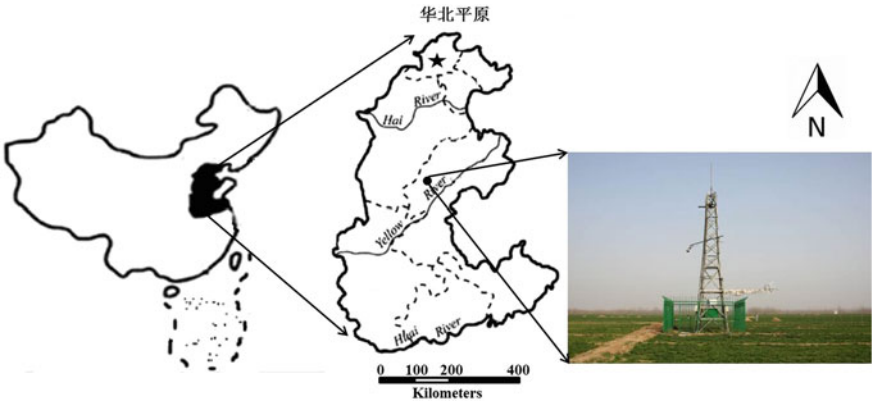

Fig. 5.8 Location of the Weishan site (Yang and Shang 2013)

annual precipitation of 532 mm (averaged from 1984 to 2007) and mean annual pan evaporation of 1,950 mm (20 cm diameter evaporation pan; 1961–2005). The annual average air temperature is 13.3 °C (1984–2007). The dominant crops at the site are winter wheat and summer maize planted in rotation; this is the main cropping system in the North China Plain. The growing season for winter wheat is from late October to early June, while summer maize is planted in mid-June and harvested in late September. However, because wheat grows very slowly or even stops during winter season due to low temperature and frozen soil, only the main growing season of winter wheat from early March to early June and summer maize from mid-June to late September was considered in this study.

During the growing seasons of 2007, sensible and latent heat fluxes were measured by a 10-m high flux tower mounted with an eddy covariance system placed 3.7 m above the ground at 30-min interval. Meteorological data, including air temperature and humidity, air pressure, downward and upward solar and long-wave radiation, precipitation and wind speed and direction were recorded at 10-min interval. Soil heat fluxes were measured at a depth of 3 cm at two sides of the tower. The uncertainty analysis of EC measurements at Weishan site can be found in Lei and Yang (2010), and the residual method was recommended by Yang et al. (2010) to force the energy closure of the EC system at this site. A detailed description of the site and the measurements can be found in Lei and Yang (2010).

Remote Sensing Data: The Moderate resolution Imaging Spectroradiometer (MODIS) data were used to force the HTEM model at the Weishan site because of its high temporal resolution (daily) and accessible spatial resolution (1 km). Good agreement between sensible heat flux measured by large aperture scintillometer (1 km) and that by EC system (100–500 m) was reported in Weishan site (Lei et al. 2011), indicating the EC data adequately represents the area within one MODIS pixel and could provide accurate observations of actual surface fluxes. Data sets titled MOD09GA, MOD09Q1 and MOD11A1 were used; these are available from the NASA data center (http://reverb.echo.nasa.gov/). The original images were re-projected into UTM projection and resampled with a spatial resolution of 1,000 m. During the study period between March 1st (DOY 60) and September 30th (DOY 273), a total number of 66 cloud free MODIS images were available, with 39 days in the growing season of winter wheat and 27 days in the growing season of summer maize.

Variable Derivation: Liang's (2001) method was used to calculate broadband surface albedo from seven channels recorded in the data set of MOD09GA. NDVI was derived from the red and near-infrared bands following Huete et al. (2002). The observed maximum NDVI during study period was 0.93 ($NDVI_{max}$) and observed NDVI for bare soil (non-growing season) was 0.12 ($NDVI_{min}$). The coefficient n was determined to be 0.7 through optimizing Eq. (5.7) based on field measurements of vegetation coverage. Because only a few measurements of LAI were available during the study period, a parametric relationship between LAI and NDVI (8-day temporal resolution and 250 m spatial resolution, MOD09Q1) was used to obtain consecutive LAI values (Lei et al. 2012), and h_c was expressed as a function of LAI based on local measurement. Before vegetation height reaches its maximum value,

$$h_c = 0.1029 \times LAI^{1.4496} \text{ for winter wheat} \tag{5.27}$$

$$h_c = 0.2755 \times LAI^{1.3911} \text{ for summer maize} \tag{5.28}$$

5.4.2 Results

5.4.2.1 Validation at Flux Site

Comparison between measured energy fluxes (R_n, G, H and LE) and estimated ones from the HTEM at Weishan site during the growing season of 2007 are shown in Fig. 5.9, and statistics of the HTEM performances are summarized in Table 5.4. The estimated R_n had an RMSE of 24.1 W m^{-2} and a bias of −1.3 W m^{-2} over both

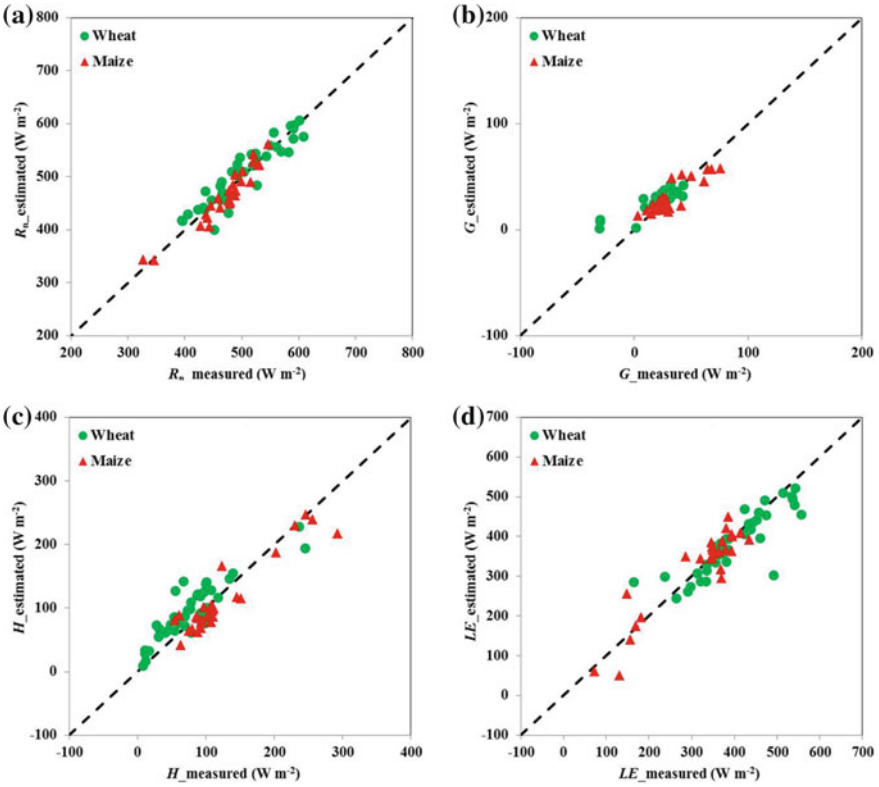

Fig. 5.9 Comparison of R_n (**a**), G (**b**), H (**c**) and LE (**d**) from HTEM using MODIS images with corresponding tower-based flux measurements at the Weishan site on during the main growing season of 2007 (Yang and Shang 2013)

Table 5.4 A summary of the statistics of the HTEM performances at Weishan site

Energy component	Crop type	$\bar{o}$ (W m^{-2})	$\bar{s}$ (W m^{-2})	Bias (W m^{-2})	RMSE (W m^{-2})	MAPE (%)
R_n	Wheat	502.5	506.3	3.8	25.7	3.7
	Maize	473.9	465.2	−8.7	21.9	3.2
	Overall	**490.8**	**489.5**	**−1.3**	**24.1**	**3.5**
G	Wheat	20.5	27.1	6.6	23.8	36.7
	Maize	31.9	29.7	−2.2	15.2	30.5
	Overall	**25.2**	**28.2**	**3**	**20.3**	**34.2**
H	Wheat	77.3	91.9	17.6	28.9	47.8
	Maize	125.3	113.9	−11.4	24.6	17.6
	Overall	96.9	102.6	5.7	27.3	35
LE	Wheat	404.7	387.3	−17.4	48.2	9.1
	Maize	316.7	321.6	4.9	39.9	14.3
	Overall	**368.7**	**358.7**	**−10**	**45**	**11.2**

$\bar{o}$ is the mean of observed values and $\bar{s}$ is the mean of HETM simulated values (Yang and Shang 2013)

growing seasons (winter wheat and summer maize). However, slightly better agreement was found during maize season than in wheat season (Table 5.4). The estimated G had an overall bias of 3 W m^{-2} (6.6 W m^{-2} for wheat season and −2.2 W m^{-2} in maize season, respectively) and an overall RMSE of 20.3 W m^{-2} (23.8 W m^{-2} in wheat season and 15.2 W m^{-2} in maize season). Similar to the SMACEX site, a local calibration of Eq. (5.11) might be beneficial to improve the accuracy of the G estimates.

The sensible heat flux had an overall RMSE of 27.3 W m^{-2} and bias of 5.7 W m^{-2}, which accounts for 5.9 % of the mean observed H. However, the sensible heat flux were systematically overestimated in the wheat growing season and underestimated in the maize growing season. This was likely a result of the semi-empirical estimates of LAI and h_c (Eqs. 5.27 and 5.28).

Despite the systematic errors in estimated H, the simulated LE showed high consistency with measurements, suggesting that errors in the estimates of available energy and the sensible heat flux were somehow canceled each other out. The overall RMSE of estimated LE for both seasons was 45 W m^{-2} and the bias was -10 W m^{-2}. The LE RMSE was lower for winter wheat than for summer maize, however the MAPE was higher for maize than for winter wheat.

In general, the HTEM performed better in estimating all four energy components during maize season than in the wheat season. The fact that only a few measurements of LAI and h_c were available during this experiment may result in inaccurate parameter estimates for Eqs. (5.27) and (5.28). A more realistic relationship between LAI and h_c may improve predictions of H and LE at this site.

5.4.2.2 Processes of Evaporation and Transpiration

The measured total *LE* and estimated canopy transpiration (LE_c) and soil evaporation (LE_s) during the study period are shown in Fig. 5.10. All three variables showed a bimodal process within one year due to the crop rotation cycle. The estimated LE_c increases with the greening of crops and decreases with crop senescence (as indicated by changes in NDVI). On the contrary, LE_s decreases during the crop greening stages and increases when senescence. This phenomenon suggests that HTEM could reasonably reflect the vegetation coverage effect on evaporation and transpiration partitioning. To further test the vegetation control on LE_c and LE_s partitioning in the HTEM, the ratio of LE_c (LE_s) to equilibrium evaporation against *LAI* (F_r) are shown in Fig. 5.11. The equilibrium evaporation is calculated from (Eichinger et al. 1996),

$$LE_{eq} = \frac{\Delta(R_n - G)}{\Delta + \gamma} \tag{5.29}$$

where Δ is the slope of relation between saturated vapor pressure and temperature, γ is the psychometric constant.

For both growing seasons of winter wheat and summer maize, the ratio of LE_c to LE_{eq} has a positive relationships with both LAI and F_r (Fig. 5.11a, b). Theoretically, this is because that a higher LAI value corresponds to a higher canopy light interception and a higher F_r value represents a larger proportion of surfaces occupied by vegetation, and therefore, as defined in the patch approach, a higher

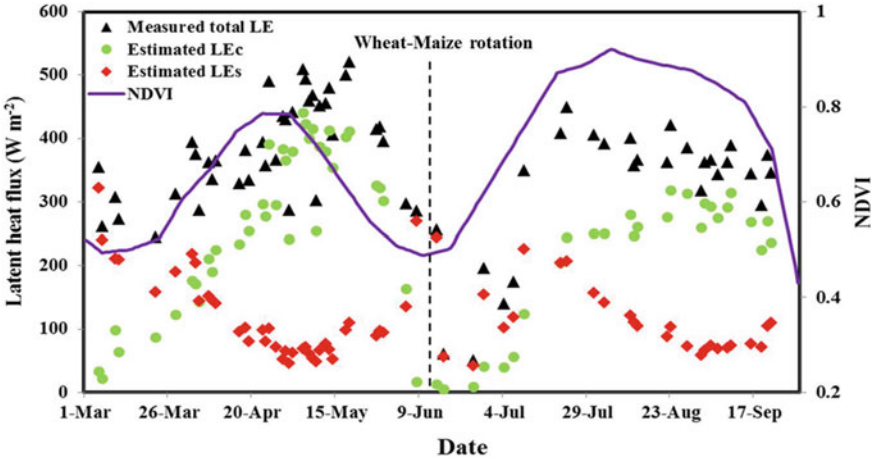

Fig. 5.10 Processes of NDVI, estimated canopy transpiration (LE_c), soil evaporation (LE_s) and measured total evapotranspiration (*LE*) during the simulation period at the Weishan site. Each value represents the corresponding latent heat flux at satellite imaging time (Yang and Shang 2013)

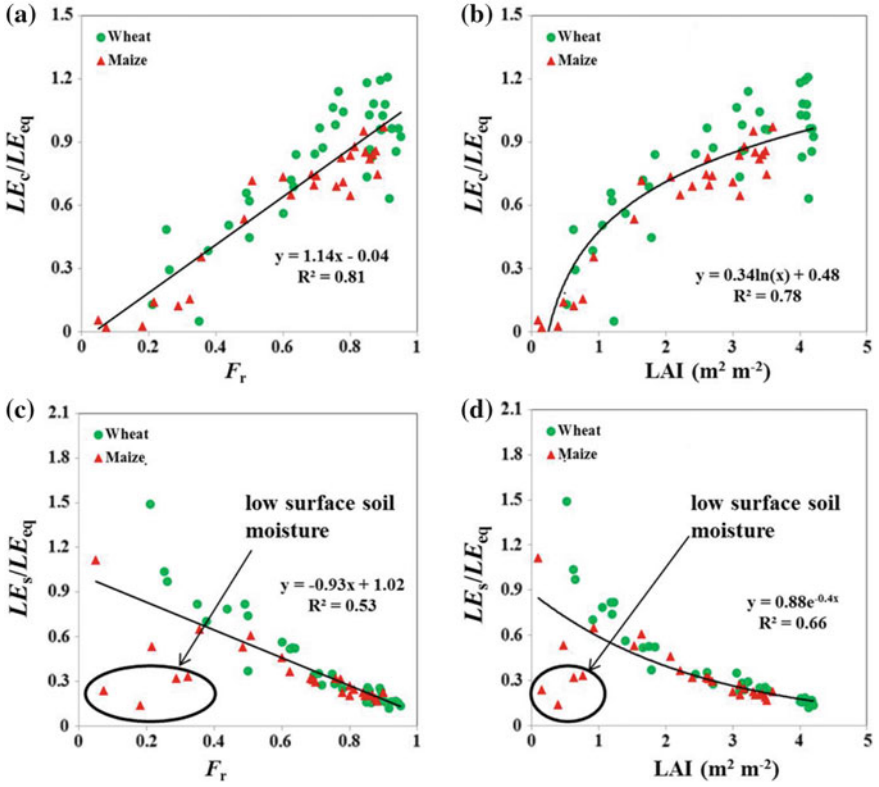

Fig. 5.11 Relationships between the ratio of estimated LE_c and LE_s to LE_{eq} against F_r (**a** and **c**) and LAI (**b** and **d**) during the simulation period at Weishan site. The *solid lines* represent best fit relationships (Yang and Shang 2013)

LE_c would occur. Not surprisingly, the ratio of LE_s to LE_{eq} is negatively correlated with LAI and F_r, as can be seen from Fig. 5.11c, d. It is noticed that in Fig. 5.11c, d, some points (within the oval) are significantly lower than the fitted lines; this was due to the fact that the surface soil moisture for these days was significantly lower than during the other days. Since the equilibrium evaporation only reflects atmospheric controls on evapotranspiration, the variation of soil moisture availability could leads to the scatter of the point clouds in Fig. 5.11.

5.4.3 Comparison with Other Models

Yang et al. (2010) estimated energy fluxes using the Surface Energy Balance System (SEBS) model based on MODIS Terra image for the main growing season of winter wheat and summer maize of 2006–2008 at the Weishan flux site, and their model performances are compared with those from HTEM (Fig. 5.12).

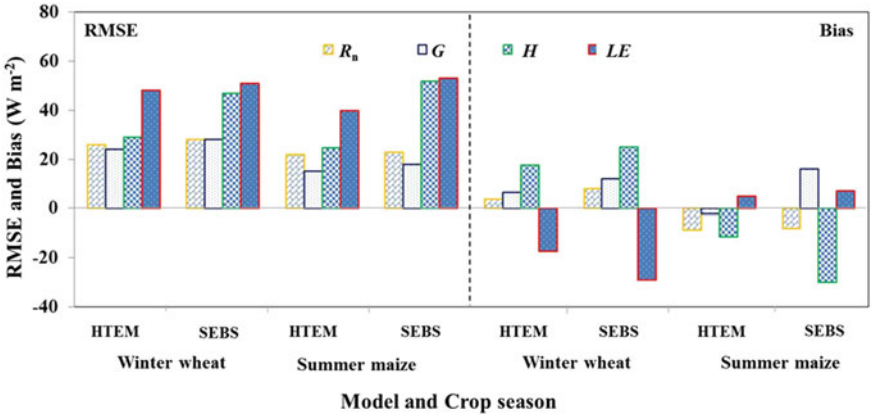

Fig. 5.12 Comparison of model performance between HTEM and SEBS (Yang et al. 2010) at the Weishan flux site (Yang and Shang 2013)

For both growing seasons of winter wheat and summer maize, the HTEM RMSE of H and LE were slightly lower than those from SEBS. The benefit of the HTEM is its hybrid dual-source scheme; the single-source scheme used by SEBS does not distinguish evaporation and transpiration, which results in great errors under low LAI and F_r conditions (i.e., the greening and senescence stages of both wheat and maize). However, both HTEM and SEBS showed systematic biases in H and LE during the wheat season. Since both R_n and G were accurately estimated during the wheat season, these systematic errors were most likely due to non-optimal vegetation parameters, determined from remote sensing-based LAI estimates.

5.5 Conclusion

In this chapter, a new remote sensing evapotranspiration model (HTEM) based on the hybrid dual-source scheme and the theoretical trapezoid framework is proposed. This model, designed to estimate energy fluxes using remotely sensed data, was inspired by Guan and Wilson (2009) who partitioned potential evaporation and potential transpiration using the hybrid dual-source scheme, and by Long et al. (2012) who theoretically determined the boundaries of the trapezoidal F_r/LST space. HTEM employs the layer approach to partition available energy and the patch approach to estimate sensible and latent fluxes separately from the soil and vegetation canopy. HTEM is different from a layer model in that it distinguishes the difference in evaporation from inter-canopy soil and from under-canopy soil, and limit convective transfer contribution to transpiration only from vegetated fractions. HTEM is also different from a patch model in that it allows soil evaporation from under-canopy soil, and the vegetation effect on both evaporation and transpiration is

somehow considered. These features suggest a high potential of the HTEM model to be used for a wide range of surfaces with different vegetation coverage patterns.

Soil wetness isolines within a theoretically determined trapezoid F_r/LST space are used in HTEM to decompose bulk radiative surface temperature into canopy temperature and soil temperature. In such way, additional assumptions such as the Priestley-Taylor approximation used in the TSEB model and the complementary relationship used in Nishida et al. (2003) are no longer needed. However, ignoring the advection effect on turbulent transport is still a limitation of the HTEM, a more realistic cold edge should be the focus of further efforts.

Performance of the HTEM was tested at both the humid SMACEX site in Iowa with Landsat TM/ETM+ data and the sub-humid Weishan site in North China Plain with MODIS Terra data. Results showed that energy fluxes from HTEM agree well with tower based measurements, and are generally better than other remote sensing evapotranspiration models applied with the same data sets. Additionally, the HTEM could provide reasonable partitioning between evaporation and transpiration. Sensitivity analysis suggests that the HTEM is mostly sensitive to temperature variables, and less sensitive to other meteorological observations and the hypothetic vegetation parameters.

References

Agam N, Kustas WP, Anderson MC, Norman JM, Colaizzi PD, Howell TA, Prueger JH, Meyers TP, Wilson TB (2010) Application of the Priestley-Taylor approach in a two-source surface energy balance model. J Hydrometeor 11:185–198

Alfieri J, Kustas WP, Prueger JH, Hipps LE, Chavez JL, French A, Evett SR (2011) Intercomparison of nine micrometeorological stations during the BEAREX08 field campaign. J Atmos Oceanic Technol 28:1390–1406

Allen RG, Tasumi M, Trezza R (2007) Satellite-based energy balance for mapping evapotranspiration with internalized calibration (METRIC)-model. J Irrig Drain E-ASCE 133:380–394

Anderson MC, Neale C, Li F, Norman JM, Kustas WP, Jayanthi H, Chavez J (2004) Upscaling ground observations of vegetation water content, canopy height, and leaf area index during SMEX02 using aircraft and Landsat imagery. Remote Sens Environ 92:447–464

Anderson MC, Norman JM, Kustas WP, Li F, Prueger JH, Mecikalski JR (2005) Effects of vegetation clumping on two-source model estimates of surface energy fluxes from an agricultural landscape during SMACEX. J Hydrometeor 6:892–909

Bastiaanssen WGM (2000) SEBAL-based sensible and latent heat fluxes in the irrigated Gediz Basin, Turkey. J Hydrol 229:87–100

Bastiaanssen WGM, Menenti M, Feddes RA, Holtslag AAM (1998) A remote sensing surface energy balance algorithm for land (SEBAL)—1 formulation. J Hydrol 213:198–212

Brown KW, Rosenberg NJ (1973) A resistance model to predict evapotranspiration and its application to a sugar beet field. Agron J 65:341–347

Brutsaert W (1975) On a derivable formula for long-wave radiation from clear skies. Water Resour Res 11:742–744

Carlson T (2007) An overview of the "Triangle Method" for estimating surface evapotranspiration and soil moisture from satellite imagery. Sensors 7:1612–1629

Carlson TN, Ripley DA (1997) On the relation between NDVI, fractional vegetation cover, and leaf area index. Remote Sens Environ 62:241–252

Carlson T, Gillies RR, Perry EM (1994) A method to make use of thermal infrared temperature and NDVI measurements to infer surface soil water content and fractional vegetation cover. Remote Sens Rev 9:161–173

Choi M, Kustas WP, Anderson MC, Allen RG, Li F, Kjaersgaard JH (2009) An intercomparison of three remote sensing-based surface energy balance algorithms over a corn and soybean production region (Iowa, U.S.) during SMACEX. Agric For Meteorol 149:2082–2097

Eichinger WE, Parlange MB, Stricker H (1996) On the concept of equilibrium evaporation and the value of the Priestley-Taylor coefficient. Water Resour Res 32:161–164

Fisher JB, Tu KP, Baldocchi DD (2008) Global estimates of the land–atmosphere water flux based on monthly AVHRR and ISLSCP-II data, validated at 16 FLUXNET sites. Remote Sens Environ 112:901–919

Gillies RR, Carlson TN, Cui J, Kustas WP, Humes KS (1997) A verification of the 'triangle' method for obtaining surface soil water content and energy fluxes from remote measurements of the Normalized Different Vegetation Index (NDVI) and surface radiant temperature. Int J Remote Sens 18:3145–3166

Gonzalez-Dugo MP, Neale C, Mateos L, Kustas WP, Prueger JH, Anderson MC, Li F (2009) A comparison of operational remote sensing-based models for estimating crop evapotranspiration. Agric For Meteorol 149:1843–1853

Guan H, Wilson JL (2009) A hybrid dual-source model for potential evaporation and transpiration partitioning. J Hydrol 377:405–416

Huete A, Didan K, Miura T, Rodriguez EP, Gao X, Ferreira LG (2002) Overview of the radiometric and biophysical performance of the MODIS vegetation indices. Remote Sens Environ 83:195–213

Jiang L, Islam S (1999) A methodology for estimation of surface evapotranspiration over large areas using remote sensing observations. Geophys Res Lett 26:2773–2776

Jiang L, Islam S (2001) Estimation of surface evaporation map over sourthern Great Plains using remote sensing data. Water Resour Res 37:329–340

Jiang L, Islam S (2003) An intercomparison of regional latent heat flux estimation using remote sensing data. Int J Remote Sens 24:2221–2236

Jiang L, Islam S, Guo W, Jutla AS, Senarath S, Ramsay BH (2009) A satellite-based daily actual evapotranspiration estimation algorithm over South Florida. Global Planet Change 67:62–77

Komatsu TS (2003) Toward a robust phenomenological expression of evaporation efficiency for unsaturated soil surfaces. J Appl Meteorol 42:1330–1334

Kustas WP, Norman JM (1997) A two-source approach for estimating turbulent fluxes using multiple angle thermal infrared observations. Water Resour Res 33:1495–1508

Kustas WP, Norman JM (1999) Evaluation of soil and vegetation heat flux predictions using a simple two-source model with radiometric temperatures for partial canopy cover. Agric For Meteorol 94:13–29

Kustas WP, Hatfield JL, Prueger JH (2005) The soil moisture-atmosphere coupling experiment (SMACEX): background, hydrometeorological conditions, and preliminary findings. J Hydrometeorol 6:791–804

Lei H, Yang D (2010) Interannual and seasonal variability in evapotranspiration and energy partitioning over an irrigated cropland in the North China Plain. Agric For Meteorol 150:581–589

Lei H, Yang D, Liu Y (2011) Comparison of the sensible heat flux measurements on different spatial scales in an irrigated cropland. J Hydraulic Eng 42:136–142 (In Chinese)

Lei H, Cai J, Yang D, Wang F (2012) Long-term variability of evapotranspiration in a large irrigated area in lower reach of Yellow River. Adv Sci Technol Water Resour 31:13–17 (in Chinese)

Lhomme JP, Chehbouni A (1999) Comments on dual-source vegetation-atmosphere transfer models. Agric For Meteorol 94:269–273

Li F, Jackson TJ, Kustas WP, Schmugge TJ, French AN, Cosh MH, Bindlish R (2004) Deriving land surface temperature from Landsat 5 and 7 during SMEX02/SMACEX. Remote Sens Environ 92:521–534

Li F, Kustas WP, Prueger JH, Neale C, Jackson TJ (2005) Utility of remote sensing-based two-source energy balance model under low- and high-vegetation cover conditions. J Hydrometeor 6:878–891

Liang S (2001) Narrowband to broadband conversions of land surface albedo I: algorithms. Remote Sens Environ 76:213–238

Lindquist JL, Arkebauer TJ, Walters DT, Cassman KG, Dobermann A (2005) Maize radiation use efficiency under optimal growth conditions. Agron J 7:72–78

Long D, Singh VP (2012a) A modified surface energy balance algorithm for land (M-SEBAL) based on a trapezoidal framework. Water Resour Res 48:W02528

Long D, Singh VP (2012b) A two-source Trapezoid Model for Evapotranspiration (TTME) from satellite imagery. Remote Sens Environ 121:370–388

Long D, Singh VP, Scanlon BR (2012) Deriving theoretical boundaries to address scale dependencies of triangle models for evapotranspiration estimation. J Geophys Res 117:D05113

Moran MS, Clarke TR, Inoue Y, Vidal A (1994) Estimating crop water deficit using the relation between surface-air temperature and spectral vegetation index. Remote Sens Environ 49:246–263

Mu Q, Zhao M, Running SW (2011) Improvements to a MODIS global terrestrial evapotranspiration algorithm. Remote Sens Environ 115:1781–1800

Nishida K, Nernani RR, Running SW (2003) An operational remote sensing algorithm of land surface evaporation. J Geophys Res 108:4270

Norman JM, Kustas WP, Humes KS (1995) Source approach for estimating soil and vegetation energy fluxes in observations of directional radiometric surface temperature. Agric For Meteorol 77:263–293

Price JC (1990) Using spatial context in satellite data to infer regional scale evapotranspiration. IEEE Trans Geosci Remote Sens 28:940–948

Sánchez JM, Kustas WP, Caselles V, Anderson MC (2008) Modelling surface energy fluxes over maize using a two-source patch model and radiometric soil and canopy temperature observations. Remote Sens Environ 112(3):1130–1143

Sandholt I, Rasmussen K, Andersen J (2002) A simple interpretation of the surface temperature/vegetation index space for assessment of surface moisture status. Remote Sens Environ 79:213–224

Shuttleworth WJ, Wallace JS (1985) Evaporation from sparse crops—an energy combination theory. Q J Roy Meteorol Soc 111:839–855

Sinclair TR, Horie T (1989) Leaf nitrogen, photosynthesis, and crop radiation use efficiency: a review. Crop Sci 29:90–98

Su Z (2002) The surface energy balance system (SEBS) for estimation of turbulent heat fluxes. Hydrol Earth Syst Sci 6:85–99

Thorne GN, Pearman I, Day W, Todd AD (1988) Estimation of radiation interception by winter wheat from measurements of leaf area. J Agric Sci Cambridge 110:101–108

Timmermans WJ, Kustas WP, Anderson MC, French AN (2007) An intercomparison of the Surface Energy Balance Algorithm for Land (SEBAL) and the Two-Source Energy Balance (TSEB) modeling schemes. Remote Sens Environ 108:369–384

Twine TE, Kustas WP, Norman JM, Cook DR, Houser PR, Meyers TP, Prueger JH, Starks PJ, Wesely ML (2000) Correcting eddy-covariance flux underestimates over a grassland. Agric For Meteorol 103:279–300

Verhoef A, De Bruin H, Van Den Hurk B (1997) Some practical notes on the parameter kB^{-1} for sparse vegetation. J Appl Meteorol 36:560–572

Yan H, Wang SQ, Billesbach D, Oechel W, Zhang JH, Meyers T, Martin TA, Matamala R, Baldocchi D, Bohrer G, Scott R (2012) Global estimation of evapotranspiration using a leaf area index-based surface energy and water balance model. Remote Sens Environ 124:581–595

Yang Y, Shang S (2013) A hybrid dual source scheme and trapezoid framework based evapotranspiration model (HTEM) using satellite images: algorithm and model test. J Geophys Res: Atmos 118:2284–2300

Yang D, Chen H, Lei H (2010) Estimation of evapotranspiration using a remote sensing model over agricultural land in the North China Plain. Int J Remote Sens 31:3783–3798

Yang Y, Shang S, Guan H (2012a) Development and field verification of a soil-plant-atmosphere continuum model (HDS-SPAC) based on the hybrid dual-source approach in the wheat land. Sci China Tech Sci 55:2671–2685

Yang Y, Shang S, Jiang L (2012b) Remote sensing temporal and spatial patterns of evapotranspiration and the response to water management in a large irrigation district of North China. Agric For Meteorol 164:112–122

Zhang RH, Sun XM, Wang WM, Xu JP, Zhu ZL, Tian J (2005) An operational two-layer remote sensing model to estimate surface flux in regional scale: physical background. Sci China Ser D 48:225–244

Zhang B, Kang S, Li F, Zhang L (2008) Comparison of three evapotranspiration models to Bowen ratio-energy balance method for a vineyard in an arid desert region of northwest China. Agric For Meteorol 148:1629–1640

Chapter 6
Remote Sensing Temporal and Spatial Patterns of Evapotranspiration and the Responses to Water Management in a Large Irrigation District of North China

6.1 Introduction

In arid and semiarid areas, agriculture relies heavily on irrigation of water diverted from rivers. However, with intensified changes of climate and land use, runoff of many rivers in arid area showed a declined trend during the past 50 years (Zhang et al. 2011). Meanwhile, increasing water needs for industrial, domestic and environmental uses, has led to water resources scarcity globally (Vörömarty et al. 2000). Consequently, traditional irrigation agriculture in these areas is now facing a big challenge, which appeals people to develop water-saving irrigation for sustainable water use.

One example of such cases is the Hetao Irrigation District in Inner Mongolia, North China. Hetao Irrigation District is the third largest irrigation district in China, with a total irrigation area of 573,300 hm^2. It is located in a typical arid region with an average annual precipitation of 130–350 mm and mean annual pan evaporation of about 2,300 mm (Yu et al. 2010). As a result, precipitation is far less than crop water requirement, and irrigation is essential for agriculture. Annual average water diversion from the Yellow River is 5.165 billion m^3 (from 1980 to 2000), which accounts for about 1/10 of annual discharge of the Yellow River (53.5 billion m^3, measured at Huayuankou station from 1956 to 2000). However, due to the impact of human activities and climate change, runoff within the Yellow River basin has declined significantly during the past 50 years (Fu et al. 2004, 2007). The global and regional projections showed that the warming trend is likely to continue in the region during 21st century (Houghton et al. 2001; Nijssen et al. 2001), which will further decrease runoff and thus exacerbate water resources shortages in the basin.

In order to tackle the water shortage issue, Chinese government started a program of irrigation districts rehabilitation for water-saving in Hetao and other large-scale irrigation districts in the Yellow River basin in 1998. The aim of the program at Hetao is to reduce water diversion from the Yellow River to 4 billion m^3 in 2015 while keeping the same agricultural production. Engineering measures have been

Y. Yang, *Evapotranspiration Over Heterogeneous Vegetated Surfaces*,
Springer Theses, DOI 10.1007/978-3-662-46173-0_6

applied since 1999, including reducing water diversions, increasing groundwater use, lining diversion channels, improving irrigation efficiency, and so on. A direct consequence of reducing water diversion from the Yellow River is the reduction in water supply within the irrigation district, which will significantly change the hydrological cycle of the region, as well as water allocation and consumption for different land use types.

Evapotranspiration (ET) is the most active process in the hydrological cycle (Oki and Kanae 2006), and is also a major component of energy and water balance in agriculture ecosystems (Burba and Verma 2005). Thus, understanding the spatial and temporal variability in ET is important for identifying the impact of meteorology, soil water and crop factors on ET, and is vital for hydrologic modeling and irrigation scheduling (Lei and Yang 2010). For Hetao Irrigation District, there is a particular need of ET studies under the changing water use strategies for better water resources management.

In regard to evapotranspiration studies, in situ measurements, such as weighting lysimeter, Bowen ratio system, sap flow meters and eddy covariance technique, are generally considered to be reliable methods for quantifying ET at a point or field scale for specific sites (Baldocchi 2003; Gonzalez-Altozano et al. 2008; Kang et al. 2003; Zhang et al. 2008). However, it is fairly difficult to apply such methods for larger scale ET quantifying. Wylie et al. (2003) has pointed out that biased estimates occurs when the individual flux measurements are extrapolated to the regional scale, as many flux sites cannot appropriately represent a larger area. Similarly, traditional ET estimation models, whose parameters depend mostly on field observations, are greatly restricted to be used at a small scale, i.e., soil-plant-atmosphere continuum models (Zeppel et al. 2008).

Fortunately, remote sensing technique, which is able to capture land surface information from larger geographic extents, provides an effective tool and methodology for retrieving the ground parameters for estimating ET at regional scale. Various models have been proposed for estimating ET with remotely sensed data over the past decades, such as TSEB model (Norman et al. 1995), SEBAL model (Bastiaanssen et al. 1998), S-SEBI model (Roerink et al. 2000), SEBS model (Su 2002), LandSAF model (Gellens-Meulenberghs et al. 2007), STSEB model (Sánchez et al. 2008), GLEAM model (Miralles et al. 2011), MODIS-ET model (Mu et al. 2011) and HTEM model proposed in Chap. 5. These models generally performed well, with the relative errors of 5–30 % in comparison with ground based flux measurements at different ecosystems around the world. Detailed discussion of remote sensing-based ET estimation models can be can be found in Gowda et al. (2008) and Li et al. (2009).

In this chapter, the HTEM model was applied to 4 counties of Hetao Irrigation District to map its evapotranspiration from 2000 to 2010. Because of soil frozen, ET during winter season is negligible compared with crop growing seasons. Thus, only crop growing periods from April to October were considered in this study. ET from different land use types were estimated and analyzed separately. The main objectives were: (1) to understand the spatial pattern of ET in the region, (2) to

understand interannual and seasonal variability of ET in the region, (3) to identify controlling factors of ET over different land use types, and (4) to evaluate the benefit of water-saving rehabilitation during the past 11 years.

6.2 Study Site and Data

6.2.1 Study Area

The Hetao Irrigation District (N40.1°–41.4° E106.1°–109.4°) is located in the western part of Inner Mongolia Autonomous Region, North China. Four counties (Linhe, Wuyuan, Dengkou and Hangjinhouqi) in the district which have the largest water diversions were selected for this study (Fig. 6.1). The area is characterized with a typical continental climate, being very cold in winter with little snowfall and

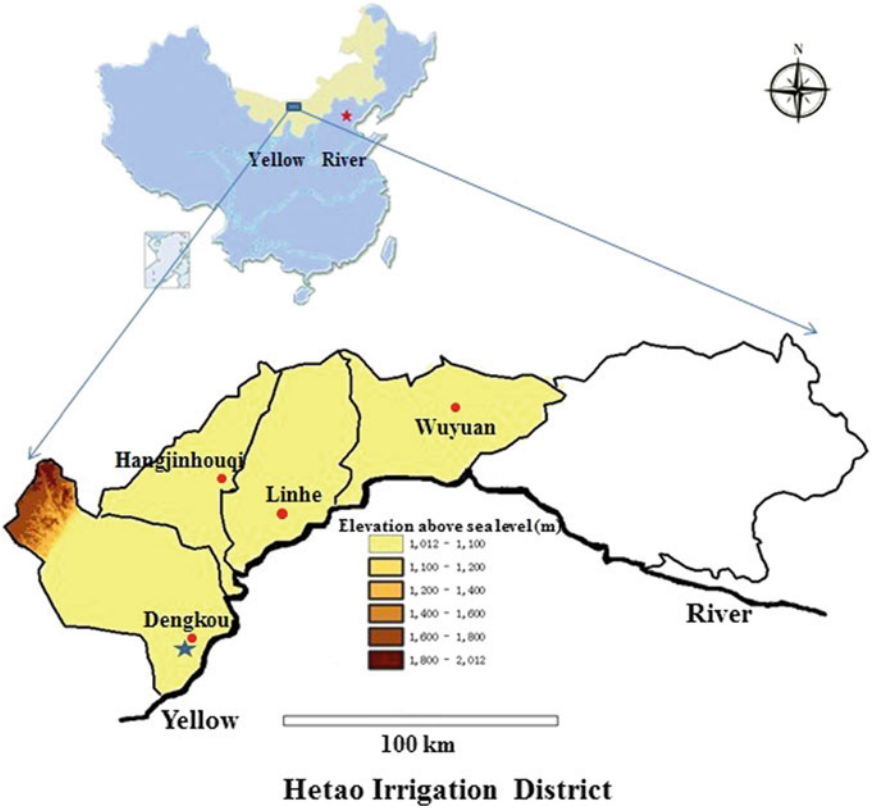

Fig. 6.1 Location of the study area (*Pentagram* indicates the location of Dengkou Agricultural Experiment Station) (Yang et al. 2012)

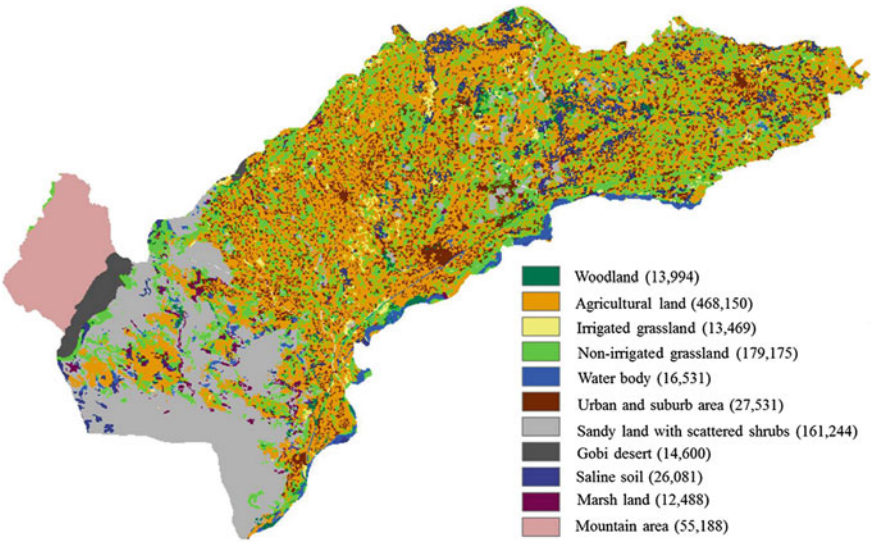

Fig. 6.2 Land use map for the study area (*Figure* within the bracket indicates the area of the land use type, hm^2) (Yang et al. 2012)

very dry in summer. Average annual temperature is about 5.6–7.4 °C. Plain occupies most part of the study area, with the elevation slightly higher in the south-west and lower in the north-east (a.s.l. 1,028–1,062 m), except for a mountain region in the north-west of Dengkou County (a.s.l. 1,059–2,012 m) (Fig. 6.1). Besides, in the central and southern part of Dengkou County, there is an extensive area of sandy land and Gobi desert (Fig. 6.2). The groundwater water table ranges between 0.8 and 2.6 m within a year, and the soil texture is silty clay loam with severe salinization (Yu et al. 2010).

Spring wheat, summer maize and sunflower are predominant crops within the irrigation district. The growing season for spring wheat is from late March to mid-July, while maize and sunflower are planted in late April and late May, and harvested in mid-October and mid-September, respectively. Because of soil frozen from November to March, the crop growing periods from April to October was considered in the following analysis.

6.2.2 Data Sources

The Moderate Resolution Imaging Spectroradiometer (MODIS) data were used for this study because of its high temporal resolution (1–2 days) and accessible spatial resolution (250–1,000 m). Data sets including MOD09GA and MOD11A1 were downloaded from NASA Data Center (https://wist.echo.nasa.gov/api). The original

images were re-projected into Universal Transverse Mercator (UTM) projection and resampled with a spatial resolution of 250 m. Images with cloud cover less than about 5 % were used in the study based on visual examination (Table 6.1). Liang's method (Liang 2001) was used to calculate broadband surface albedo from seven shortwave channels, and NDVI was derived from red and near-infrared bands following Huete et al. (2002) and Zhou et al. (2009).

Land use map (1:100,000) of the study area for the year of 2000 was provided by Environmental and Ecological Science Data Center for West China, National Natural Science Foundation of China (http://westdc.westgic.ac.cn). DEM data (SRTM) with spatial resolution of 90 m were downloaded from http://srtm.csi.cgiar.org/. Daily climate data for the study area were provided by China Meteorology Data Sharing Service System (http://cdc.cma.gov.cn/). All these data were processed to be the same with MODIS images in terms of their spatial reference and resolution.

Table 6.1 MODIS images used in this study (Yang et al. 2012)

Year	Total number	Day of year
2000	21	98, 106, 120, 124, 135, 143, 151, 160, 163, 174, 181, 192, 194, 207, 235, 242, 251, 256, 264, 266, 275
2001	30	103, 106, 110, 128, 131, 132, 135, 136, 137, 138, 148, 151, 153, 155, 158, 164, 192, 194, 203, 210, 211, 213, 221, 231, 232, 235, 236, 253, 263, 287
2002	29	95, 114, 123, 128, 113, 136, 149, 152, 157, 175, 179, 192, 195, 197, 206, 211, 214, 217, 218, 223, 227, 229, 231, 240, 260, 266, 268, 272, 281
2003	24	105, 106, 115, 120, 122, 128, 131, 143, 148, 154, 157, 166, 173, 189, 201, 206, 217, 218, 225, 235, 244, 250, 265, 274
2004	37	95, 101, 105, 107, 108, 113, 114, 115, 117, 128, 132, 133, 140, 142, 143, 146, 151, 152, 161, 172, 183, 188, 189, 197, 206, 212, 216, 217, 220, 221, 238, 242, 247, 252, 270, 277, 282
2005	22	94, 107, 114, 117, 126, 128, 134, 147, 152, 157, 165, 168, 173, 192, 205, 212, 229, 238, 244, 251, 264, 274,
2006	30	112, 120, 126, 133, 138, 142, 148, 151, 154, 161, 165, 176, 181, 186, 207, 209, 214, 215, 218, 226, 227, 228, 245, 248, 252, 254, 255, 258,259, 273
2007	29	98, 114, 115, 120, 125, 132, 133, 139, 146, 147, 152, 155, 157, 164, 178, 181, 190, 200, 214, 219, 232, 239, 246, 253, 264, 265, 266, 267, 284
2008	28	98, 104, 107, 119, 125, 139, 141, 143, 144, 149, 159, 170, 176, 177, 187, 194, 203, 207, 216, 219, 235, 239, 240, 251, 254, 255, 259, 276
2009	26	105, 106, 123, 125, 127, 142, 145, 150, 161, 165, 170, 171, 176, 182, 187, 196, 204, 206, 217, 225, 238, 243, 254, 257, 271, 282
2010	26	113, 121, 122, 126, 130, 139, 153, 155, 162, 164, 175, 186, 196, 203, 209, 217, 225, 234, 235, 238, 240, 255, 256, 266, 268, 277

Data used for regional water balance modeling, including precipitation, total water diversion from the Yellow River, total outflow and groundwater depth for each county, were monitored and provided by the Hetao Irrigation District Administration in Inner Mongolia Autonomous Region in North China (http://www.htgq.gov.cn).

6.3 Evaluation of HTEM Performance

In this study, two ways were adopted to examine the performance of HTEM model. At field scale, the output of HTEM model was compared with average ET rate of 5–7 days in the Dengkou Agricultural Experiment Station in 2009 (N40.41° E107.04°) (Dai et al. 2011). During the growing of 2009, soil moisture at different soil layers (0–20, 20–40, 40–60, 60–80, 80–100 cm) were measured using both oven drying and TRIME-IPH methods with a sampling interval of 5–7 days. Evapotranspiration between sampling days were derived by soil water balance calculation. Then, a spatial averaged ET over different sampling points was used as the representative for the whole pixel.

At regional scale, total ET for the growing season (April–October) of 2001–2009 estimated by HTEM was tested with regional water modeling,

$$ET_{\text{water\_balance}} = P + D - R - \Delta S \tag{6.1}$$

where $ET_{\text{water\_balance}}$ is the total ET calculated by water balance model; P and D are the total rainfall and total water diversion from the Yellow River, respectively; R is the total outflow, while there are no water flows into the region except the Yellow River. ΔS is the annual variation of soil moisture storage, which was estimated from the measured changes in groundwater depth,

$$\Delta S = \Delta G * A * \mu \tag{6.2}$$

where ΔG is annual change in groundwater depth, and A is total area. μ is specific yield, and was chosen as 0.046 following Chen et al. (2005).

6.4 Results and Discussion

6.4.1 Model Validation

At the field scale, the SEBAL estimated ET closely match the observed data (Dai et al. 2011) (Fig. 6.3), with the root mean square error of 0.60 mm day^{-1} and the relative error of 10.8 %. This accuracy is very similar with that of the SEBAL model applied in the same region (RMSE = 0.53 mm day^{-1}, relative error = 14.6 %) (Yang et al. 2012).

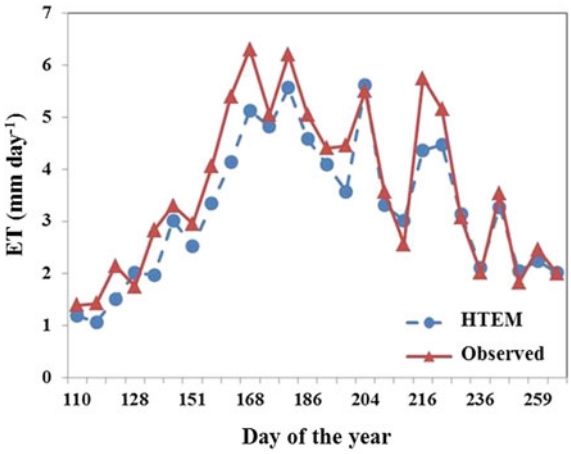

Fig. 6.3 Comparison between HTEM estimated ET and measured ET

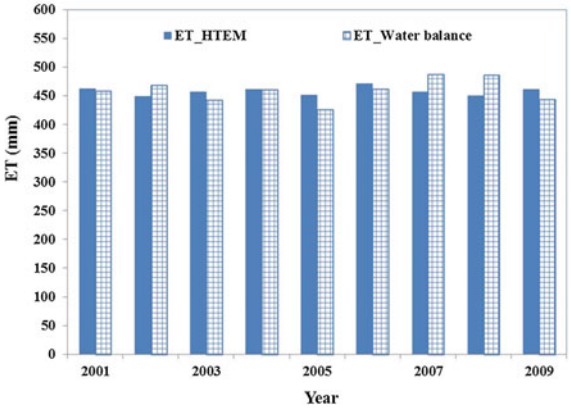

Fig. 6.4 Comparison between total growing season ET calculated by HTEM and water balance model from 2001 to 2009

At the regional scale, the growing season ET estimated by HTEM generally agrees well with the output of water balance model (Fig. 6.4). The root mean square error is 21.9 mm and the relative error is 5.6 %. This error is slightly lower that of the SEBAL model, which shows an RMSE of 26.1 mm (or 5.7 %), as reported in Yang et al. (2012).

6.4.2 Spatial ET Pattern

The major advantage of remote sensing based ET estimation methods is its ability to describe the spatial variation of ET at regional scale. The spatial pattern of growing season ET of the year 2004 for the study area is illustrated in Fig. 6.5. The reason to choose this year for illustration is that most available MODIS images were

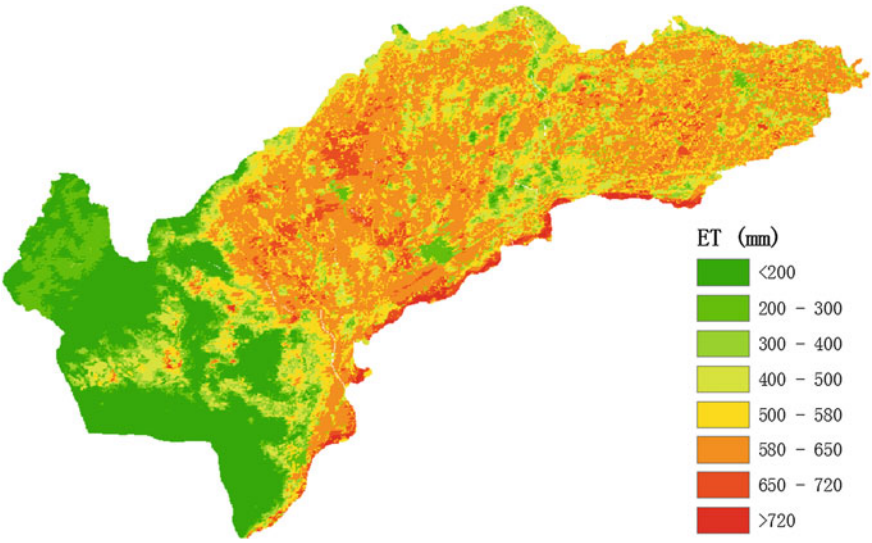

Fig. 6.5 Spatial distribution of HTEM estimated total ET for the growing season (April–October) of 2004

used in 2004 (Table 6.1), which is believed to be able to produce the most reliable model outputs (Ozdogan et al. 2010).

Overall, the growing season ET was higher in the northern and eastern parts of the study area, and obviously lower in the southwest. This is because there are wide-ranging areas of sandy land and Gobi desert in the Southwest, while agriculture land occupies most part of northern and eastern regions, as indicated in Fig. 6.2. The highest ET happens over water body of the Yellow River along the Southern edge of the region. For the three counties in the eastern part (Wuyan, Linhe and Hangjinghouqi), ET ranges from 250 to over 700 mm, with most area between 500 and 650 mm. The lower ET occurs over the city and the scattered sandy dune areas. For Dengkou in the southwest, the growing season ET was less than 300 mm in most areas, while comparatively higher over the agricultural and marsh lands in the central part of the county. In the mountain area, where the land surface is mainly covered by bare rock with sparse vegetation, ET was around 250 mm.

6.4.3 Evapotranspiration Over Agriculture Land

The annual summaries of estimated agricultural land evapotranspiration (ET_{agri}) and other hydrometeorological characteristics are listed in Table 6.2. All ET discussed below are spatial averaged values of different land use types. Agricultural land ET during the growing season from 2000 to 2010 ranged from 578 to 634 mm, with the

Table 6.2 Annual summaries of spatial averaged growing season agricultural land evapotranspiration (ET_{agri}) and other hydrometeorological characteristics, including reference evapotranspiration (ET_r), cumulative net radiation (R_n), mean air temperature (T_a), mean vapor pressure deficit (VPD), total precipitation (P) and mean wind speed for the growing period

Year	ET_{agri} (mm)	ET_r (mm)	R_n (MJ m^{-2})	T_a (°C)	VPD (kPa)	P (mm)	Wind speed (m s^{-1})
2000	598.4	916.2	2324.6	18.0	1.26	94.2	1.7
2001	595.1	903.9	2323.3	18.6	1.26	157.0	1.7
2002	579.2	880.9	2373.2	17.8	1.20	139.8	1.6
2003	588.7	927.9	2372.3	17.8	1.15	134.7	2.1
2004	599.6	948.6	2362.6	17.8	1.16	148.2	2.1
2005	597.5	955.0	2347.1	18.9	1.43	76.9	1.7
2006	618.9	964.3	2392.3	18.8	1.34	162.6	1.8
2007	594.7	919.0	2323.0	18.2	1.29	145.2	1.6
2008	578.1	904.7	2390.7	18.2	1.30	190.2	1.5
2009	612.3	958.5	2368.5	18.8	1.45	78.2	1.6
2010	633.9	978.8	2497.7	17.3	1.11	133.4	2.5
Average	599.8	932.5	2370.5	18.2	1.27	132.8	1.8
Maximum	633.9	978.8	2497.7	18.9	1.45	190.2	2.5
Minimum	578.1	880.9	2323.0	17.3	1.11	76.9	1.5

highest ET occurred in 2010 and lowest in 2002. The variation of annual ET_{agri} was in good accordance with the variation of annual reference ET. The relationship between them can be described by a linear function (Fig. 6.6), with the coefficient of determination (R^2) of 0.75. This is because that soil moisture of agricultural land is artificially controlled at a high level by irrigation systems in the region. Therefore,

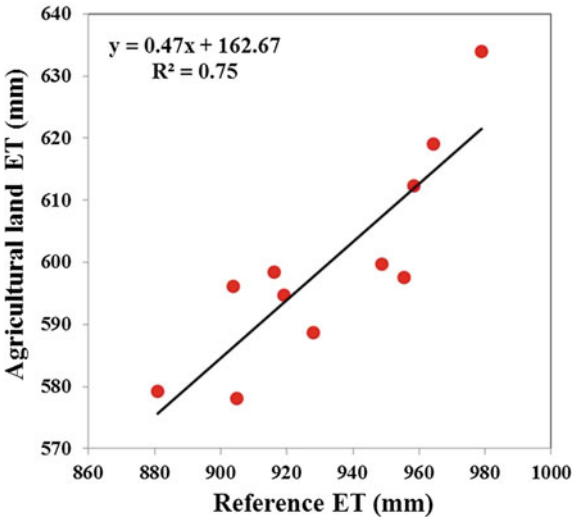

Fig. 6.6 Relationship between agricultural land evapotranspiration and reference evapotranspiration for the growing season of 2000–2010

meteorological condition becomes the major influencing factor on actual evapotranspiration. Likewise, due to irrigation, rainfall impacts little on ET_{agri} (Table 6.2).

The daily ET_{agri} over the growing season (April–October) ranged from 2.72 to 2.96 mm day^{-1}, with a mean value of 2.80 mm day^{-1}. Compared with other farmland ecosystems in North China, this value is higher than that measured in Weishan Irrigation District of North China Plain (2.24 mm day^{-1}, winter wheat and summer maize, Lei and Yang 2010), while lower than those measured in Luancheng of North China Plain (3.9 mm day^{-1}, winter wheat and summer maize, Liu et al. 2002) and estimated in Songnen Plain of Northeast China (3.9 mm day^{-1} averaged from May to September, maize and spring wheat, Zeng et al. 2010.).

The monthly ET over agricultural land during the past 11 years is illustrated in Fig. 6.7. The seasonal variation of ET_{argi} within a year was a unimodal curve, with the peak value occurring in June in most years. This is very different from the trend found in North China Plain, where ET_{agri} showed a bimodal process within a year (Lei and Yang 2010; Liu et al. 2002). In North China Plain, multiple cropping of winter wheat and summer maize in a year results in low ET in late growing period of winter wheat and early growing period of summer maize. However, cropping pattern in Hetao area is single cropping of spring wheat, summer maize and sunflower. ET over agricultural lands does not decrease too much during the harvest of spring wheat, while still maintains at a high level in response to the rapid growth of summer maize and sunflowers.

Monthly agricultural land ET was plotted against reference ET to investigate the meteorological control on seasonal variability in ET_{agri} (Fig. 6.8). On a monthly basis, reference ET explained 77 % of seasonal variability in ET_{agri} during the whole growing seasons. However, as the crop growing stage may also be an important controlling factor of ET_{agri} (Allen et al. 1998), the whole growing period was divided into three sub-periods based on the criteria that months within each

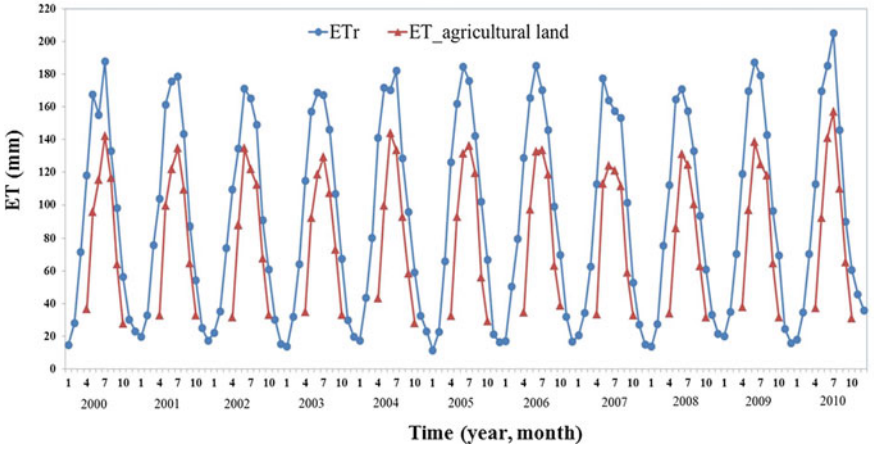

Fig. 6.7 Spatial averaged monthly agriculture land ET and reference ET (ET_r) in the study area from 2000 to 2010

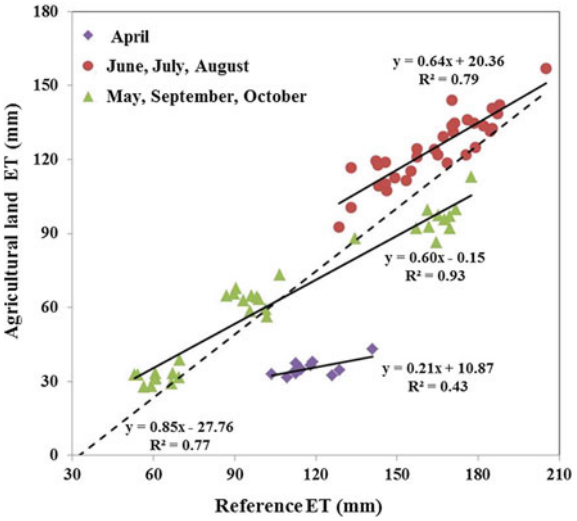

Fig. 6.8 Relationship between monthly agriculture land ET and reference ET. The *dashed line* fits to the whole data set, and *solid lines* fit to each subset of data

sub-period have similar regional crop coefficients (K_{c_agri}, defined as the ratio of spatial averaged monthly ET_{agri} to reference ET). As shown in Fig. 6.8, during the sowing season of spring wheat in April, the regional crop coefficient had its lowest value of about 0.3. Since the time of soil thawing may be different over years which may result in different sowing time and thus variability in regional crop coefficient, only 43 % of variability in April ET_{agri} was explained by reference ET. In June, July and August, the regional crop coefficient had its highest value of around 0.76, and the variation of monthly reference ET explained 79 % of the variability of monthly ET_{agri} in this stage. During May, September and October, most crops enter its developing or senescence stage, the regional crop coefficient is higher than that of April but lower than those in June, July and August. Interestingly, the variability of monthly ET_{agri} in this sub-period is best correlated with that of reference ET with a coefficient of determination of 0.93.

6.4.4 Evapotranspiration Over Other Land Use Type

Annual summaries of evapotranspiration over different land use types are listed in Table 6.3. Water body had the largest ET with the mean value of 632 mm, while Gobi desert had the minimum ET of 90 mm. Following water body, irrigated grassland had the second largest mean ET of 553 mm. Marsh land, woodland and non-irrigated grassland had similar annual ET with the mean value of about 460 mm. Beside, ET over urban and suburb, mountain region and sandy land were 393, 200 and 136 mm, respectively. Notably, average annual ET over mountain areas was slightly higher than annual precipitation. This is due to the underestimation of precipitation over mountain regions, as all measured rainfall data were collected in the plain area.

Table 6.3 Annual summaries of spatial averaged evapotranspiration (mm) over different land use types for the growing period (April–October) of 2000–2010

Year	ET_{Wood}	ET_{IGra}	ET_{NIGra}	ET_{Wat}	ET_{Urb}	ET_{Sand}	ET_{Gobi}	ET_{Mount}	ET_{Mar}	ET_{Sal}
2000	452	541	474	635	385	121	80	187	459	431
2001	447	535	472	615	379	141	107	213	468	398
2002	439	541	453	596	402	130	97	221	446	380
2003	460	557	461	630	403	139	100	204	449	382
2004	484	551	453	638	356	140	93	203	473	390
2005	473	551	449	636	398	121	62	147	487	370
2006	481	565	450	644	406	137	99	213	491	421
2007	465	543	430	630	408	148	105	203	445	436
2008	460	550	429	611	386	158	103	224	452	439
2009	486	573	445	656	390	122	48	137	473	471
2010	478	579	457	663	411	134	92	221	490	476
Average	466	553	452	632	393	136	90	200	467	418
Maximum	486	579	474	657	419	158	107	223	491	476
Minimum	439	535	429	596	345	121	48	137	445	370

The land use types include woodland (ET_{Wood}), grassland with irrigation (ET_{IGra}) and without irrigation (ET_{NIGra}), water body (ET_{Wat}), urban and suburb area (ET_{Urb}), sandy land with scattered shrubs (ET_{Sand}), Gobi desert (ET_{Gobi}), mountain area (ET_{Mount}), marsh land (ET_{Mar}) and saline soil (ET_{Sal})

To further understand the controlling factors of ET in the region, ET over each land use type are plotted against total reference ET and cumulative rainfall in Figs. 6.9 and 6.10, respectively. As shown in Fig. 6.9, the variations of ET over water body, marsh land, woodland and irrigated grassland were largely controlled by reference ET on annual basis, with the determination coefficients of 0.87, 0.82, 0.75 and 0.69, respectively. The high dependence of woodland ET on reference ET is likely because of shallow groundwater, from which trees can uptake water with small stresses. While for irrigated grassland, irrigations were applied to maintain its growth for stockbreeding. In such cases, plants may transpire at its potential rate defined by atmospheric demand. On the contrary, the variations of annual ET over sandy land and Gobi desert were mainly explained by the variation of annual rainfall (Fig. 6.10). This is because that water was the main limitation on surface ET in these areas. However, without other water sources, rainfall became the dominant factor that controls the evapotranspiration processes. Notably, compared with the linear relationship for sandy land, the responses of ET over Gobi desert to rainfall were more like logistic, indicating that the increase rate of ET is going down with the increase of precipitation in these regions. When the total rainfall amount excesses a critical value, the extra precipitation will be taken away with surface runoff because of small water holding capacity. Annual ET and rainfall over mountain area showed similar relationship with that between ET_{Gobi} and rainfall. However, because rainfall in the mountain areas were possibly underestimated as discussed earlier, the relationship between ET_{Mount} and rainfall is not shown in Fig. 6.10.

Compared with land use types listed above, the annual variation of ET from non-irrigated grassland (ET_{NIGra}) and saline soil (ET_{Sal}) were much more complex (Table 6.3), as they did not depend either on reference ET or precipitation. ET_{Sal} firstly showed a gradual decrease from 431 mm in 2000 to 380 mm in 2002, and then

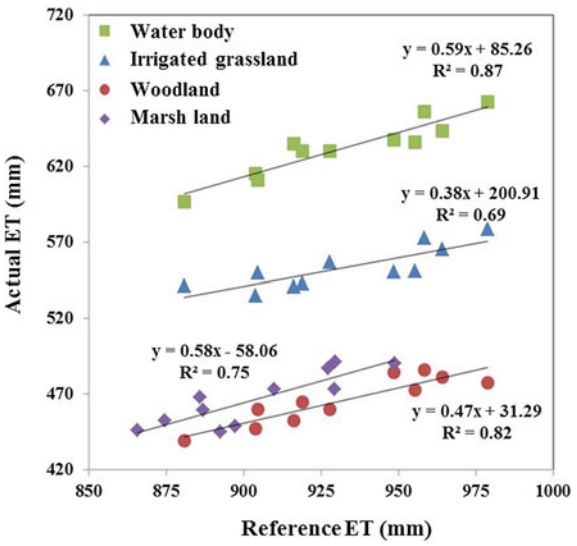

Fig. 6.9 Relationships of annual evapotranspiration over different land use types against reference evapotranspiration (ET_r)

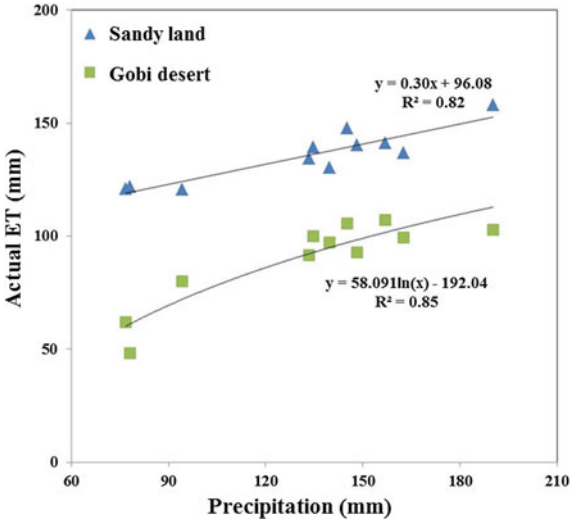

Fig. 6.10 Relationships of annual evapotranspiration over different land use type against rainfall

kept at 370–390 mm until 2005. After 2005, it went up year by year to 476 mm in 2010 (Table 6.3). This may be related to the following reasons. Firstly, as mentioned earlier, the study area has been experiencing rehabilitation for water-saving since 1999. The reduction in irrigation and the increase in groundwater exploration have led to a rapid decrease in groundwater level during the first several years (Fig. 6.11), which may have resulted in insufficient water supply for saline fields, and thus decreased ET_{Sal}. Secondly, the soil salinity has likely reduced after the decrease of groundwater table (Yu et al. 2010). This may have resulted in an increasing evapotranspiration after 2005, due to less salinity stress (Lamsal et al. 1999).

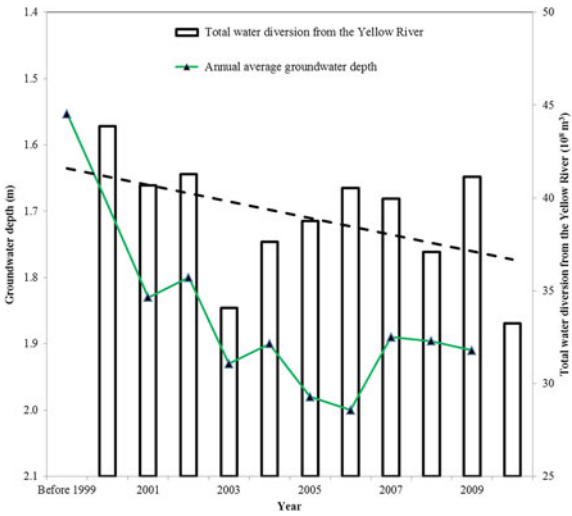

Fig. 6.11 Variations of annual average groundwater depth and total water diversion from the Yellow River. The *dashed line* indicates the variation trend of total water diversion. (Groundwater depth data for 2000 and 2010 are missing) (Yang et al. 2012)

Thirdly, a small part of saline land may have been reclaimed to agricultural land with the progress of irrigation district rehabilitation and with the decrease in soil salinization as indicated in Gao et al. (2008). However, because the most recent land use classification was made in 2000, the possible changes in saline soil area are not considered in the study.

The interannual variation of regional crop coefficient of the non-irrigated grassland (K_{c_NIGra}) is shown in Fig. 6.12. Generally, K_{c_NIGra} decreased significantly during the study period, with an average annual decline of 0.6 %. The decline of K_{c_NIGra} reflects the increase of water stresses on evapotranspiration. Further analysis of K_{c_NIGra} trend shows that K_{c_NIGra} decreased greater from 2000 to 2005, and almost remain the same after 2005. This is in good agreement with the annual variation of ET_{Sal} before 2005, which could have been caused by a decline in groundwater table (Fig. 6.11). Figure 6.13 shows a close relationship between K_{c_NIGra} and the

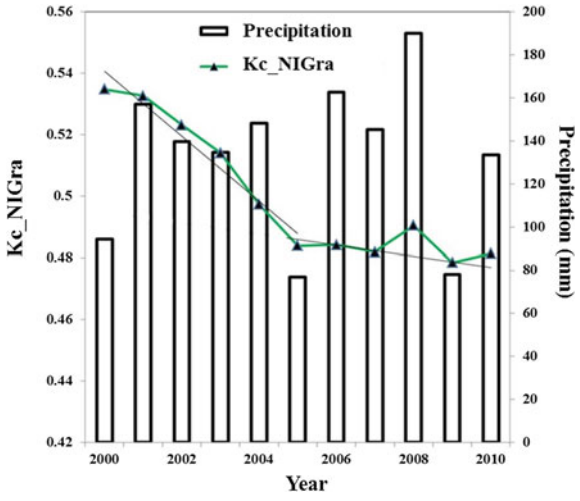

Fig. 6.12 Variations of annual crop coefficient (K_{c_NIGra}) of non-irrigated grassland and annual rainfall

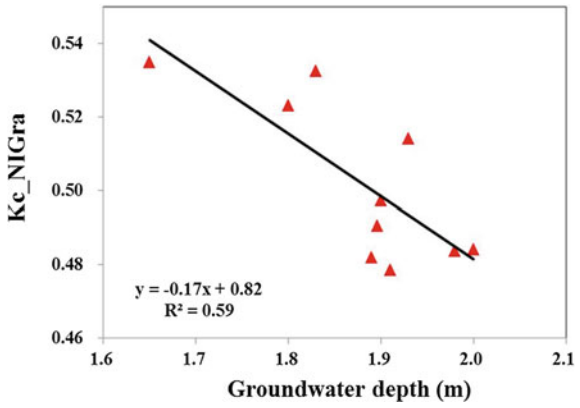

Fig. 6.13 Relationship between annual crop coefficient (K_{c_NIGra}) of non-irrigated grassland and groundwater depth

groundwater table, which could further support that the decreased in K_{c_NIGra} was mainly caused by the decline of groundwater. Different from trees, the grass root is shallow and less developed. Therefore, it is harder for grass root to access deeper groundwater, and the decline of groundwater may exert a greater impact on grassland evapotranspiration. Besides, because of root water storage capacity, the variation in total rainfall may also influence K_{c_NIGra}, as shown in Fig. 6.12.

6.4.5 *Evaluation of the Benefit of Water-Saving Rehabilitation*

ET maps over recent years provide an effective tool to evaluate the benefit of water-saving rehabilitation, as evapotranspiration is the largest term of water consumption in the study area (Du et al. 2011). As mentioned above, changing water use strategies can strongly affect regional hydrological cycle and thus water use patterns for different land use types. Figure 6.14 shows the variation in the ratio of ET_{agri} to ET_{all} on annual basis, where ET_{all} is the sum of ET over woodland, grassland, marsh land, urban and suburb, and agricultural land. Because of strong dependence on rainfall, ET from sandy land, Gobi desert and mountain area are excluded in this analysis. In addition, as part of saline fields may have been changed into agricultural lands which were not considered in this study, the ET over saline soil was not include in this analysis either.

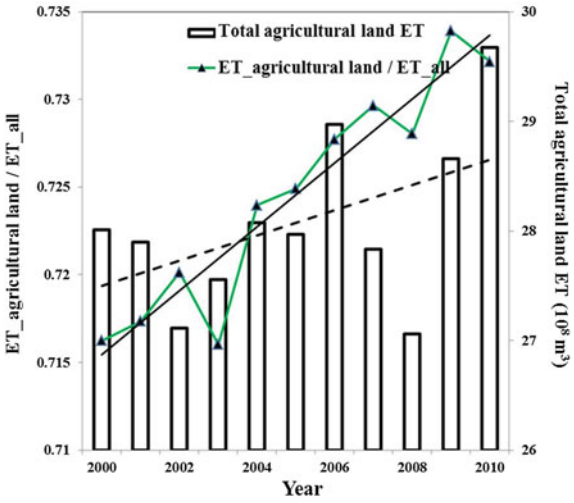

Fig. 6.14 Variations of the ratio of annual agricultural land ET to regional ET and total volume of water evaporated over agricultural land. The *solid line* indicates the variation trend of ET_{agri}/ET_{all}, and the *dashed line* indicates the variation trend of total volume of water evaporated over agricultural land

It is encouraging to see that the ratio of ET_{agri} to ET_{all} shows an ascending trend over recent years (Fig. 6.14). This indicates that the proportion of agricultural land water consumption in total water consumption has been increasing. Besides, decreased water diversion from the Yellow River (Fig. 6.11) did not result in decreased evapotranspiration in the agricultural land (Table 6.2 and Fig. 6.14), while ET_{agri} was reported to be positively correlated with agricultural yields when ET_{agri} is less than a certain value (Lei et al. 2010; Sun et al. 2006). This suggests that the rehabilitation program in Hetao Irrigation District has not affected much on its agricultural production. Inversely, the decline of groundwater level caused by reduced recharge and intensified exploitation for agricultural water use have resulted in a significant decrease in water use by non-irrigated grassland, which was found to be the largest contribution of water saving. In addition, groundwater level fall may benefit the management of saline soil, as groundwater rising during the spring and summer is the main cause of secondary salinization in the study area (Yu et al. 2010).

6.5 Conclusions

Growing season evapotranspiration from 2000 to 2010 in Hetao Irrigation District was mapped using the HTEM model fed with MODIS data. The performance of HTEM model was tested with in situ measurement at field scale and water balance modeling at regional scale, respectively. The results indicate that:

(1) The HTEM model can be well applied in Hetao area, with the RMSE of 0.6 mm day^{-1} at field scale on 5–7 days basis and 21.9 mm at regional scale on annual basis.
(2) The annual agricultural land ET ranged from 578 to 634 mm, which accounts for about 62 % of total ET in the region. Both the interannual variability in annual ET and the seasonal variability in monthly ET can be primarily explained by the variations of reference ET.
(3) The interannual variabilities in ET over water body, irrigated grassland, marsh land and woodland were strongly correlated with the variations of reference ET, while those over sandy land and Gobi desert mainly depended on the variation of annual precipitation.
(4) Agricultural land ET did not decrease with the reduction in total water diversion from the Yellow River following the progress of irrigation district rehabilitation project. On the contrary, non-irrigate grassland was found to be the largest contribution of water-saving due to groundwater level falling. These results indicate a positive effect of the rehabilitation project, and would be helpful in future water management for the area. Besides this positive effect, however, we have to notice that the continuous decrease of water supply would result in the drop of groundwater level and consequently the degradation of non-irrigated grassland, which may further cause other ecological issues.

References

Allen RG, Pereira LS, Raes D, Smith M (1998) Crop evapotranspiration: guidelines for computing crop water requirements. FAO Irrigation and Drainage Paper 56, Rome

Baldocchi DD (2003) Assessing the eddy covariance technique for evaluating carbon dioxide exchange rates of ecosystems: past, present and future. Glob Change Biol 9:479–492

Bastiaanssen WGM, Menenti M, Feddes RA, Holtslag A (1998) A remote sensing surface energy balance algorithm for land (SEBAL)—1 formulation. J Hydrol 213:198–212

Burba GG, Verma SB (2005) Seasonal and interannual variability in evapotranspiration of native tallgrass prairie and cultivated wheat ecosystems. Agric For Meteorol 135(1–4):190–201

Chen YX, Qu ZY, Shi HB, Wei ZM, Li YL (2005) Finite element method forecast for groundwater movement after water-saving rehabilitation in large-sized irrigation district, case study of an experimental area in the Hetao Plain of Yellow River. China Rural Water Hydropower 2:10–12 (In Chinese)

Dai JX, Shi HB, Tian DL, Xia YH, Li MH (2011) Determination of crop coefficients of main grain and oil crops in inner Mongolia Hetao irrigated area. J Irrig Drain 30:23–27 (in Chinese)

Du LJ, Liu Y, Lei B (2011) Analysis on water cycle factors of Jiefangzha irrigation area in Hetao irrigation district in Inner Mongolia based on runoff-evaporation hydrological model for arid Plain Oasis. J China Inst Water Resour Hydropower Res 9:168–175 (in Chinese)

Fu G, Chen S, Liu C, Shepard D (2004) Hydro-climatic trends of the Yellow River basin for the last 50 years. Clim Change 65:149–178

Fu G, Charles SP, Viney NR, Chen SL, Wu JQ (2007) Impacts of climate variability on stream-flow in the Yellow River. Hydrol Process 21:3431–3439

Gao HY, Wu JW, Duan XL, Xu SL, Chen AP, Jiang WY, Liu H (2008) The impact of water-tabel on the ecological environment of Hetao irrigation area. J Arid Land Resour Environ 22:5 (in Chinese)

Gellens-Meulenberghs F, Arboleda A, Ghilain N (2007) Towards a continuous monitoring of evapotranspiration based on MSG data. In: Accepted contribution to the proceedings of the symposium on remote sensing for environmental monitoring and change detection. IAHS series. IUGG, Perugia, Italy, p 7

Gonzalez-Altozano P, Pavel EW, Oncins JA, Doltra J, Cohen M, Paco T, Massai R, Castel JR (2008) Comparative assessment of five methods of determining sap flow in peach trees. Agric Water Manag 95:503–515

Gowda PH, Chavez JL, Colaizzi PD, Evette SR, Howell TA, Tolk JA (2008) ET mapping for agricultural water management: present status and challenges. Irrig Sci 26:223–237

Houghton JT, Ding Y, Griggs DJ, Noguer M, van der Linden PJ, Dai X, Maskell K, Johnson CA (2001) Climate change 2001: the scientific basis: contribution of working grope I to the third assessment report of the intergovernmental panel on climate change. Cambridge University Press, Cambridge

Huete A, Didan K, Miura T, Rodriguez EP, Gao X, Ferreira LG (2002) Overview of the radiometric and biophysical performance of the MODIS vegetation indices. Remote Sens Environ 83:195–213

Kang SZ, Gu BJ, Du TS, Zhang JH (2003) Crop coefficient and ratio of transpiration to evapotranspiration of winter wheat and maize in a semi-humid region. Agric Water Manag 59:239–254

Lamsal K, Pandyal GN, Saeed M (1999) Model for assessing impact of salinity on soil water availability and crop yield. Agric Water Manag 41:57–70

Lei H, Yang D (2010) Interannual and seasonal variability in evapotranspiration and energy partitioning over an irrigated cropland in the North China Plain. Agric For Meteorol 150:581–589

Lei H, Yang D, Lokupitiya E, Shen Y (2010) Coupling land surface and crop growth models for predicting evapotranspiration and carbon exchange in wheat-maize rotation croplands. Biogeosciences 7:3363–3375

Li Z, Tang R, Wan Z, Bi Y, Zhou C, Tang B, Yan G, Zhang X (2009) A review of current methodologies for regional evapotranspiration estimation from remotely sensed data. Sensors 9:3801–3853

Liang SL (2001) Narrowband to broadband conversions of land surface albedo I algorithms. Remote Sens Environ 76:213–238

Liu C, Zhang X, Zhang Y (2002) Determination of daily evaporation and evapotranspiration of winter wheat and maize by large-scale weighing lysimeter and micro-lysimeter. Agric For Meteorol 111:109–120

Miralles DG, Holmes T, De Jeu R, Gash JH, Meesters A, Dolman AJ (2011) Global land-surface evaporation estimated from satellite-based observations. Hydrol Earth Syst Sci 15:453–469

Mu Q, Zhao M, Running SW (2011) Improvements to a MODIS global terrestrial evapotranspiration algorithm. Remote Sens Environ 115:1781–1800

Nijssen B, O'Donnell G, Hamlet A, Lettenmaier D (2001) Hydrologic sensitivity of global rivers to climate change. Clim Change 50:143–175

Norman J, Kustas W, Humes K (1995) A two-source approach for estimating soil and vegetation energy fluxes in observations of directional radiometric surface temperature. Agric For Meteorol 77:263–293

Oki T, Kanae S (2006) Global hydrological cycles and world water resources. Science 313:1068–1072

Ozdogan M, Yang Y, Allez G, Cervantes C (2010) Remote sensing of irrigated agriculture: opportunities and challenges. Remote Sens 2:2274–2304

Roerink GJ, Su Z, Menenti M (2000) S-SEBI: a simple remote sensing algorithm to estimate the surface energy balance. Phys Chem Earth (B) 25:145–157

Sánchez JM, Kustas WP, Caselles V, Anderson MC (2008) Modelling surface energy fluxes over maize using a two-source patch model and radiometric soil and canopy temperature observations. Remote Sens Environ 112:1130–1143

Su Z (2002) The surface energy balance system (SEBS) for estimation of turbulent heat fluxes. Hydrol Earth System Sci 6:85–99

Sun HY, Liu CM, Zhang XY, Shen YJ, Zhang YQ (2006) Effects of irrigation on water balance, yield and WUE of winter wheat in the North China Plain. Agric Water Manag 85:211–218

Vörömarty CJ, Green P, Salisbury J, Lammers RB (2000) Global water resources: vulnerability from climate change and population growth. Science 289:284–288

Wylie BK, Johnson DA, Laca E, Saliendra NZ, Gilmanov TG, Reed BC, Tieszen LL, Worstell B (2003) Calibration of remotely sensed, coarse resolution NDVI to CO_2 fluxes in a sagebrush-steppe ecosystem. Remote Sens Environ 85:243–255

Yang Y, Shang SH, Jiang L (2012) Remote sensing temporal and spatial patterns of evapotranspiration and the responses to water management in a large irrigation district of North China. Agric For Meteorol 164:112–122

Yu R, Liu T, Xu Y, Zhu C, Zhang Q, Qu Z, Liu X, Li C (2010) Analysis of salinization dynamics by remote sensing in Hetao irrigation district of North China. Agric Water Manag 97:1952–1960

Zeng LH, Song KS, Zhang B, Wang ZM, Liu DW, Du J (2010) Spatial mapping of actual evapotranspiration and water deficit with MODIS products in the Songnen Plain, northeast China. In: IEEE international geoscience and remote sensing symposium (IGARSS), 2010, pp 879–882

Zeppel M, Macinnis-Ng C, Palmer A, Taylor D, Whitley R, Fuentes S, Yunusa I, Williams M, Emaus D (2008) An analysis of the sensitivity of sap flow to soil and plant variables assessed for an Australian woodland using a soil-plant-atmosphere model. Funct Plant Biol 35:509–520

Zhang B, Kang SZ, Li FS, Zhang L (2008) Comparison of three evapotranspiration models to Bowen ratio-energy balance method for a vineyard in an arid desert region of northwest China. Agric For Meteorol 148:1629–1640

Zhang Q, Singh VP, Sun P, Chen X, Zhang Z, Li J (2011) Precipitation and streamflow changes in China: changing patterns, causes and implications. J Hydrol 410:204–216

Zhou X, Guan H, Xie H, Wilson JL (2009) Analysis and optimization of NDVI definitions and areal fraction models in remote sensing of vegetation. Int J Remote Sens 30:721–751

Chapter 7
A Novel Method for Estimating Terrestrial Evapotranspiration by Exploiting the Linkage Between Water and Carbon Cycles

7.1 Introduction

As stated in Chap. 5, among many methods of ET quantification, satellite remote sensing has been shown to be one of the most promising ways of mapping ET over larger areas (e.g., Bastiaanssen et al. 1998; Norman et al. 1995). Numerous models with varying structure and complexities have been developed to derive ET from remotely sensed variables (e.g., land surface temperature, LST, and vegetation index, VI) in combination with concurrent meteorological measurements (e.g., near surface air temperature and vapor pressure) (e.g., Bastiaanssen et al. 1998; Long and Singh 2012; Lu and Zhuang 2010; Norman et al. 1995; Su 2002; Yang and Shang 2013). With increasing spatial and temporal resolutions of satellite images, meteorological inputs at sufficient temporal and spatial scales corresponding to those of satellite images are required but infrequently available. For example, the Moderate Resolution Imaging Spectroradiometer (MODIS) Global Terrestrial Evapotranspiration Product (MOD16) adopts Global Modeling and Assimilation Office meteorological data at 1° latitude × 1.25° longitude resolution, and uses the version 4 0.05-degree Climate Modeling Grid albedo as a major model input (Mu et al. 2011). This is much too coarse with respect to 1 km × 1 km MODIS pixel and the mismatch in spatial resolution among the three input data sets is a key limitation of MOD16, especially for regions with strong climatic gradients.

Although it would be possible to improve the spatial resolution of meteorological fields, it is worthwhile exploring methods to estimate ET only from remotely sensed information. This would substantially reduce the input effort and therefore increase the robustness of satellite-based ET models. The idea lies in use of some variables which are highly correlated with ET and have the potential to be estimated based entirely on remote sensing.

ET consists of two components, evaporation (E) from the soil and transpiration (T) from the vegetation canopy. Because photosynthesis and transpiration are both biologically regulated by plant stomata and T generally dominates ET over vegetated

Y. Yang, *Evapotranspiration Over Heterogeneous Vegetated Surfaces*,
Springer Theses, DOI 10.1007/978-3-662-46173-0_7

surfaces, gross primary production (GPP) is considered valuable to infer ET over large areas only using satellite data (Beer et al. 2009; Zhang et al. 2009). Existing studies have shown that use of remote sensing data solely can provide reasonable GPP estimates across a wide range of vegetation types (Rahman et al. 2005; Sims et al. 2008; Peng et al. 2013). Moreover, the ratio of GPP to ET, known as the ecosystem water use efficiency (WUE), was found to be fairly constant over time for certain ecosystems (Beer et al. 2007, 2009; Law et al. 2002). Therefore, once the among-site variability of WUE is well assessed, ET can be estimated from remotely sensed GPP. The objective of this chapter is to develop a method to estimate ET using remotely sensed GPP. ET estimates from the developed method were evaluated with eddy covariance measurements within the Ameriflux network.

7.2 Site, Data and Methods

7.2.1 Flux Site Data

Data from 20 sites within the Ameriflux network (http://public.ornl.gov/) were used to develop and evaluate the new method (Table 7.1). These sites represent a wide diversity of bioclimate across North America. For each site, daily values of GPP and ET accumulated from half-hourly measurements of net ecosystem exchange and latent heat by eddy covariance systems were used. Data quantity control was described in publications listed in Table 7.1. Daily data were further summed up to obtain monthly GPP and ET values. Months with data-gap longer than 3 days were discarded from this analysis. In addition to flux data, biological and ancillary data, such as leaf area index and soil texture, were also acquired.

7.2.2 Remote Sensing Data

To estimate GPP, two MODIS land surface products were used in this study (from the Oak Ridge National Laboratory's Distributed Active Archive Center (http://www.modis.ornl.gov/modis/), including Enhanced Vegetation Index (EVI) and LST. EVI was obtained from the 16-day Terra MODIS vegetation index product (MOD13Q1, 250 m) and LST was acquired from the 8-day LST and Emissivity product (MOD11A2, 1,000 m). The LST data were averaged with two consecutive periods of the data in order to conform to the 16-day MODIS EVI data. Only EVI data with aerosol values listed as "low" and the "usefulness" values greater than 8 (on a scale of 0–10) and LST data marked as cloud free were used. Following Sims et al. (2006), all data were extracted from 3 km × 3 km area centered on the flux tower.

Table 7.1 Descriptions of the flux sites in this study, including Site identifier (Site ID), Plant Functional Type (PFT), Latitude (Lat, °N), Longitude (Lon, °W), data period, observed Water Use Efficiency (WUE), coefficient of determination between observed monthly GPP and monthly ET (R^2) and reference (Yang et al. 2013)

Site ID	PFT	Lat	Lon	Data period	WUE	R^2	References
US_Ha1	DBF	42.54	−72.17	2001–2005	3.40	0.97	Urbanski et al. (2007)
US_WCr	DBF	45.81	−90.08	2001–2006	3.67	0.93	Cook et al. (2008)
US_MMS	DBF	39.32	−86.41	2001–2006	2.31	0.90	Dragoni et al. (2007)
US_Bar	DBF	44.07	−71.29	2004–2006	3.66	0.89	Jenkins et al. (2007)
US_MOz	DBF	38.74	−92.20	2004–2007	2.29	0.95	Gu et al. (2007)
US_Me2	ENF	44.45	−121.55	2002, 2004–2007	3.14	0.80	Irvine et al. (2007)
CA_NS1	ENF	55.88	−98.48	2002–2005	2.12	0.87	Goulden et al. (2006)
CA_NS2	ENF	55.91	−98.53	2002–2005	1.91	0.93	Goulden et al. (2006)
CA_NS3	ENF	55.91	−98.38	2001–2005	2.19	0.87	Goulden et al. (2006)
CA_NS4	ENF	55.91	−98.38	2002–2004	2.00	0.86	Goulden et al. (2006)
CA_NS5	ENF	55.86	−98.49	2001–2005	2.93	0.94	Goulden et al. (2006)
US_Wrc	ENF	45.82	−129.95	2001–2006	3.21	0.72	Paw et al. (2004)
US_Syv	MF	46.24	−89.35	2001–2005	3.39	0.95	Desai et al. (2005)
US_LPH	MF	42.54	−72.19	2002–2005	2.77	0.95	Hadley et al. (2008)
US_Ho1	MF	45.20	−68.74	2001–2004	4.27	0.93	Hollinger et al. (2004)
US_NC1	MF	35.81	−76.71	2005–2006	1.73	0.93	Noormets et al. (2010)
US_Fuf	Savanna	35.09	−111.76	2005–2007	1.69	0.86	Dore et al. (2008)
CA_NS6	Shrub	55.92	−98.96	2001–2005	1.47	0.85	Goulden et al. (2006)
CA_NS7	Shrub	56.64	−99.95	2005–2005	1.14	0.84	Goulden et al. (2006)
US_Var	Grass	38.41	−120.95	2001–2007	2.4	0.88	Ma et al. (2007)

7.2.3 Ecosystem Water Use Efficiency

The coefficient of determination (R^2) between monthly GPP and ET for the 20 sites ranges from 0.72 to 0.97 (Table 7.1), demonstrating that WUE of the ecosystem remains generally invariant at monthly scale. Then, WUE for each site was calculated from,

$$\mathrm{WUE} = \sum_n \mathrm{GPP} \left(\sum_n \mathrm{ET} \right)^{-1} \tag{7.1}$$

where n is the number of months with available data.

Ecosystem WUE varies by a factor of ~3 among sites (Fig. 7.1), which is mainly attributed to environmental gradients. Following Beer et al. (2009), we regressed WUE to two stable environment properties ($R^2 = 0.82$, $p < 0.001$, $n = 20$),

$$\mathrm{WUE} = a_1 \theta_F + a_2 (1 - e^{k_c \mathrm{LAI}_{max}}) \tag{7.2}$$

where a_1 and a_2 are regression coefficients (Table 7.2), θ_F is volumetric soil water content at field capacity and LAI_{max} is the maximum leaf area index during the data period. In this study, θ_F was estimated to be the water content retained in the soil at −0.02 MPa of suction pressure, which is midway of most reported θ_F values (−0.01 to −0.033 MPa) (Haise et al. 1954; Lei et al. 1988). The VG-M model (Van Genuchten 1980) was adopted to describe the soil water retention curve, and the parameters of the VG-M model for each site were estimated from measured soil texture and bulk density using the method given by Schaap et al (1998). The exponential function of LAI_{max} in Eq. (7.2) corresponds to the fraction of absorbed sunlight in the photosynthetic active radiation (PAR) domain. k_c is the extinction coefficient of radiation attenuation and is set to be 0.6.

The leave-one-out cross validation is performed to test Eq. (7.2) (Fig. 7.1). The estimated WUE agrees fairly well with observed ones ($R^2 = 0.80$, $p < 0.001$, $n = 20$). These estimated WUE values were later used to invert ET in combination with remotely sensed GPP.

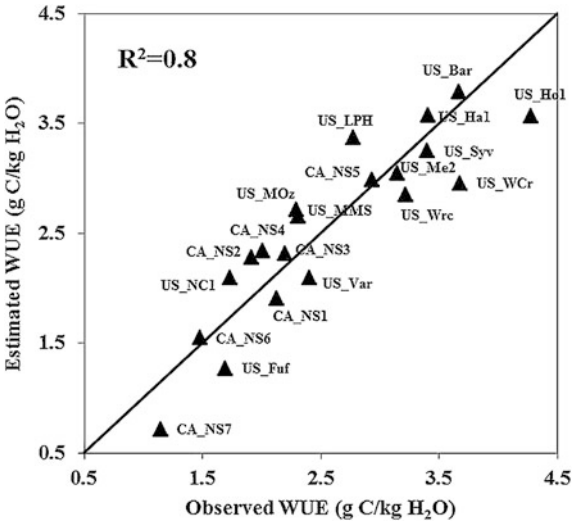

Fig. 7.1 Validation of bivariate regression WUE = f (θ_F, LAI_{max}) by leaving one out each time. Coefficient of determination between estimated and observed WUE, 1:1 line and site ID are shown (Yang et al. 2013)

Table 7.2 Value of coefficients a_1 and a_2 and estimated WUE for each site (Yang et al. 2013)

Site	a_1	a_2	Simulated WUE
US_Ha1	−5.652	4.938	3.58
US_WCr	−5.428	4.805	2.96
US_MMS	−5.534	4.905	2.66
US_Bar	−5.649	4.934	3.79
US_MOz	−5.574	4.923	2.72
US_Me2	−5.513	4.872	3.05
CA_NS1	−5.679	4.925	1.91
CA_NS2	−5.398	4.858	2.28
CA_NS3	−5.5	4.881	2.32
CA_NS4	−5.431	4.868	2.34
CA_NS5	−5.557	4.897	2.99
US_Wrc	−5.55	4.869	2.85
US_Syv	−5.483	4.858	3.25
US_LPH	−5.832	5.026	3.37
US_Ho1	−5.095	4.686	3.69
US_NC1	−5.396	4.857	2.1
US_Fuf	−5.812	4.965	1.27
CA_NS6	−5.493	4.874	1.55
CA_NS7	−5.81	4.97	0.72
US_Var	−5.576	4.885	2.1
All	−5.547	4.89	–

7.2.4 ET Estimation

As ecosystem WUE remains fairly invariant at the monthly scale, monthly ET can be calculated by dividing monthly GPP with WUE (i.e., ET = GPP/WUE). However, to be consistent with the temporal scale of the MODIS data, we calculated ET at a 16-day interval here by assuming that the 16-day WUE is also relatively constant. It is assumed that short-term (e.g., days and sub-days) fluctuations in WUE can be effectively eliminated at the 16-day timescale.

We chose the Temperature-Greenness (TG) model proposed by Sims et al. (2008) to estimate 16-day GPP. It was successfully applied to estimate 16-day GPP for evergreen and deciduous forests in North America (Sims et al. 2008). The TG model estimates GPP using a combination of MODIS LST and EVI products at the 16-day interval as:

$$\mathrm{GPP} = m\_\mathrm{TG} \times \mathrm{R\_EVI} \times \mathrm{R\_LST} \tag{7.3}$$

$$\mathrm{R\_EVI} = \mathrm{EVI} - 0.1 \tag{7.4}$$

$$\mathrm{R\_LST} = \min\left[\left(\frac{\mathrm{LST}}{30}\right), (2.5 - 0.05 \times \mathrm{LST})\right] \tag{7.5}$$

where *m*_TG is the coefficient, which can be estimated as a function of annual mean nighttime LST (Sims et al. 2008). Equation (7.4) indicates a zero GPP when EVI is smaller than 0.1, and Eq. (7.5) indicates the value of R_LST changes linearly between one when LST is 30 °C and zero when LST is 0 or 50 °C.

7.3 Results and Discussion

Overall, the proposed approach estimated 16-day ET reasonably well with reference to tower-based measurements (R^2 = 0.84, $p < 0.001$, n = 1,290). The root mean square error (RMSE) ranges from 0.16 to 0.72 mm/day and the mean relative error (MRE) are found between 0.6 and 38.6 % (Table 7.3). The bias in ET estimation results mostly from errors in modeled WUE from Eq. (7.2). For example, at US_WCr, Eq. (7.2) underestimates WUE by 19.3 %, which results in a 15.8 % overestimation of ET. The residual bias may be explained by error in *m*_TG estimates.

Larger scatters of the relationship between observed and estimated ET are found at the US_Me2 (R^2 = 0.64, p = 0.001, n = 57) and US_Fuf sites (R^2 = 0.68, $p < 0.001$, $n = 44$), which could be ascribed to the weaker relationship between GPP and ET (Table 7.3) and lower accuracy of the TG model in estimating GPP (Table 7.3). Because of the strong correlation between GPP and ET, the accuracy of ET estimates depends highly on that of GPP estimates. For the remaining sites, R^2 between observed and estimated GPP by the TG model ranges from 0.74 to 0.96, and R^2 between observed and estimated ET are all larger than 0.75 ($p < 0.001$). Besides the TG model, other remote sensing-based GPP models could also be used, e.g., the chlorophyll content model (Gitelson et al. 2006; Peng et al. 2013). Wu et al. (2011) evaluated the chlorophyll content model over 15 North American flux sites and reported that the model could provide good estimates of monthly GPP for both deciduous forest sites and non-forest sites with moderate results for evergreen forest sites.

Despite the overall good performance, the proposed method tends to underestimate ET at the lower end in all sites except for the grassland site (Fig. 7.2). This is mainly due to the underestimation of soil evaporation (E) during non-growing seasons. Theoretically, GPP should be a better indicator of plant transpiration (T) than total ET (Beer et al. 2009). However, T usually dominates ET, and the partitioning between E and T changes proportionally (depends mostly on surface vegetation conditions) during growing seasons, which may still result in a good GPP-ET relationship. Nevertheless, GPP and T declines towards zeros during non-growing season, while E may still occur if temperature and water conditions permit. Although the non-growing season is mainly defined by either low temperature or

Table 7.3 Summary of statistics of model performance at each site

Site ID	GPP_TG model		ET_This study			ET_MOD16		
	RMSE	R^2	RMSE	MRE	R^2	RMSE	MRE	R^2
US_Ha1	2.16	0.85	0.43	4.4	0.86	-	-	-
US_WCr	1.46	0.94	0.41	15.8	0.92	0.76	36.1	0.85
US_MMS	1.49	0.91	0.45	2.7	0.89	0.81	23.2	0.82
US_Bar	0.76	0.96	0.32	0.6	0.89	1.03	78.5	0.83
US_MOz	1.87	0.74	0.72	10.1	0.76	1.04	3.6	0.76
US_Me2	1.21	0.76	0.48	5.1	0.64	0.79	8.5	0.29
CA_NS1	1.17	0.85	0.22	1.1	0.95	0.51	7.1	0.70
CA_NS2	0.63	0.90	0.35	11.4	0.93	0.43	5.3	0.75
CA_NS3	1.05	0.85	0.33	4.1	0.87	0.51	20.3	0.73
CA_NS4	0.41	0.94	0.16	11.9	0.91	0.58	71.1	0.76
CA_NS5	0.75	0.92	0.24	12.2	0.92	0.65	32.8	0.71
US_Wrc	1.97	0.77	0.47	3.7	0.75	1.28	43.5	0.41
US_Syv	1.32	0.89	0.43	2.6	0.88	1.37	69.7	0.78
US_LPH	1.58	0.87	0.58	17.4	0.87	1.13	61.5	0.76
US_Ho1	1.29	0.90	0.40	18.1	0.90	-	-	-
US_NC1	1.59	0.80	0.56	14.1	0.88	-	-	-
US_Fuf	0.91	0.56	0.44	6.1	0.68	1.00	49.2	0.42
CA_NS6	1.09	0.82	0.31	8.9	0.85	0.48	17.0	0.72
CA_NS7	0.77	0.79	0.59	21.3	0.84	0.44	28.8	0.69
US_Var	1.58	0.87	0.49	38.6	0.83	-	-	-

RMSE is the root mean square error (g C/m^2 /day for GPP and mm/day for ET), MRE is the mean relative error (%). Statistics of MOD16 are given in Mu et al. (2011). Hyphen (-) denotes null value (Yang et al. 2013)

low soil moisture in natural ecosystems which implies only small E values, cautions should be paid when applying the method to cropland ecosystems where plant phenology and soil moisture conditions are profoundly impacted by human activities, e.g., irrigation.

It is more encouraging to see that nearly all statistics at all sites for the proposed method show better performance than the MOD16 product (Table 7.3). In addition to MODIS 1-km land surface products, MOD16 uses other coarse resolution meteorological inputs and is essentially an interpolated and 'pseudo-continuous' product, i.e., not truly per pixel (Rahman et al. 2005). Performance of the MODIS ET algorithm could be largely improved when in situ meteorological measurements are used (Mu et al. 2011). Another limitation in MOD16 is that the effects of soil moisture restriction on evaporation are generally reflected by meteorological forcing based on the complementary relationship, resulting in slower response of variations in energy and heat fluxes than the thermal infrared remote sensing-based ET models (Long and Singh 2010). If estimating integrated ET over longer timescales (e.g., half a month) is the main focus of studies and the MODIS ET algorithm

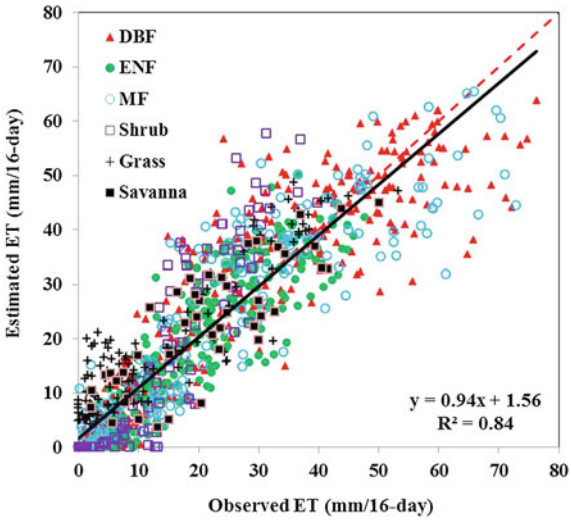

Fig. 7.2 Comparison between observed and estimated 16-day ET at 20 Ameriflux sites. The *dashed line* is the 1:1 line and the *solid line* indicates the best fit linear relationship (Yang et al. 2013)

underperforms in most cases, reliable estimates of ET based purely on satellite remote sensing demonstrated in this study should have greater robustness.

In addition to the advantages in fewer inputs, the developed method circumvents up-scaling instantaneous ET estimates at satellite overpass time to daily values or longer timescales and therefore reduces possible uncertainties in extrapolating ET under clear sky days over days without quality satellite images (Ryu et al. 2012). MODIS 16-day EVI and 8-day LST data are used in the TG model to estimate GPP and subsequently ET. These multi-day composite products are more routinely available than daily MODIS data (e.g., MODIS swath LST). Effects of cloud on ET estimation has been largely reduced because the composite 8-day LST product is mainly used to capture low temperature (e.g., non-growing season) and drought information over a half-month period in the TG model, and these information do not change substantially between clear and cloudy days. This is an advantage over those models that incorporate instantaneous remotely sensed LST.

However, there are also some limitations in the study: (1) only 20 sites were used to develop the method, which may be not sufficient to come to a robust relationship to map WUE at regional scale; (2) all sites used are located on continental North America, with most regions subject to temperate or boreal climate. To make the method an option for global ET estimation, more efforts will be needed to parameterize and validate the model over different bio-climates around the world; (3) validation of the developed method was performed only at tower scales. Validation of large-scale ET estimates from this approach can also be performed using water balance closure (e.g., Yang et al. 2012) and it is our ongoing work.

7.4 Conclusion

This chapter developed a method to estimate terrestrial ecosystem ET from remote sensing by exploiting the linkage between water and carbon cycles. The major strength of this method is that it does not require meteorological input as used by other satellite-based ET models. This method is easy to apply, requiring only routinely available EVI and LST data at longer timescales (e.g., 16 days in MODIS products) to calculate GPP, as well as remotely sensed leaf area index and regional soil texture dataset to estimate WUE. ET estimates from the proposed method compares reasonably well with flux-tower measurements at all validation sites. Comparison with the MOD16 ET product shows that the developed method generally outperforms the MOD16 algorithm. Additional efforts will be made to improve the method under lower evaporation conditions (e.g., non-growing season).

References

Bastiaanssen WGM, Menenti M, Feddes R, Holtslag A (1998) A remote sensing surface energy balance algorithm for land (SEBAL)—1 formulation. J Hydrol 213:198–212

Beer C, Reichstein M, Ciais P, Farquhar GD, Papale D (2007) Mean annual GPP of Europe derived from its water balance. Geophys Res Lett 34:L05401

Beer C et al (2009) Temporal and among-site variability of inherent water use efficiency at the ecosystem level. Glob Biogeochem Cycle 23:GB2018

Cook BD et al (2008) Using light-use and production efficiency models to predict photosynthesis and net carbon exchange during forest canopy disturbance. Ecosystems 11:26–44

Desai AR, Bolstad PV, Cook BD, Davis KJ, Carey EV (2005) Comparing net ecosystem exchange of carbon dioxide between an old-growth and mature forest in the upper Midwest, USA. Agric For Meteorol 128:33–55

Dore S, Kolb TE, Montes-Helu M, Sullivan BW, Winslow WD, Hart SC, Kaye JP, Koch GW, Hungate BA (2008) Long-term impact of a stand-replacing fire on ecosystem CO_2 exchange of a ponderosa pine forest. Glob Change Biol 14:1801–1820

Dragoni D, Schmid HP, Grimmond CSB, Loescher HW (2007) Uncertainty of annual net ecosystem productivity estimated using eddy covariance flux measurements. J Geophys Res 112:D17102

Goulden ML et al (2006) An Eddy covariance Mesonet to measure the effect of forest age on land-atmosphere exchange. Glob Change Biol 12:2146–2162

Gitelson AA et al (2006) Relationship between gross primary production and chlorophyll content in crops: implication for the synoptic monitoring of vegetation productivity. J Geophys Res 111:D08S11

Gu L, Meyers T, Pallard S, Yang B, Heuer M, Hosman KP, Liu Q, Riggs JS, Sluss D, Wullschleger SD (2007) Influences of biomass heat and biochemical energy storages on the land surface fluxes and diurnal temperature range. J Geophys Res 112:D02107

Hadley JL, Kuzeja PS, Daley MJ, Phillips NG, Mulcahy T, Singh S (2008) Water use and carbon exchange of red oak- and eastern hemlock-dominated forests in the northeastern USA: implication for ecosystem-level effects of hemlock woolly adelgid. Tree Physiol 28:615–627

Haise HR, Haas HJ, Jensen LR (1954) Soil moisture studies of some Great Plains soil: II Field capacity as related to 1/3-atmosphere percentage, and "minimum point" related to 15- and 26-atmosphere percentages. Soil Sci Soc Am J 19:20–25

Hollinger DY, Aber J, Dail B, Davidson EA, Goltz SM, Hughes H, Leclerc MY, Lee JT, Richardson AD, Rodrigues C, Scott N, Achuatavarier D, Walsh J (2004) Spatial and temporal variability in forest–atmosphere CO_2 exchange. Glob Change Biol 10:1689–1706

Irvine J, Law BE, Hibbard KA (2007) Post fire carbon pools and fluxes in semiarid ponderosa pine in Central Oregon. Glob Change Biol 13:1748–1760

Jenkins JP, Richardson AD, Braswell BH, Ollinger SV, Hollinger DY, Smith ML (2007) Refining light-use efficiency calculations for a deciduous forest canopy using simultaneous tower-based carbon flux and radiometric measurements. Agric For Meteorol 143:64–79

Law BE et al (2002) Environmental controls over carbon dioxide and water vapor exchange of terrestrial ecosystem. Agric For Meteorol 113:97–120

Lei ZD, Yang SX, Xie SC (1988) Soil water dynamics. Tsinghua University Press, Beijing

Long D, Singh VP (2010) Integration of the GG model with SEBAL to produce time series of evapotranspiration of high spatial resolution at watershed scales. J Geophys Res 115

Long D, Singh VP (2012) A two-source trapezoid model for evapotranspiration (TTME) from satellite imagery. Remote Sens Environ 121:370–388

Lu X, Zhuang Q (2010) Evaluating evapotranspiration and water-use efficiency of terrestrial ecosystems in the conterminous United States using MODIS and Ameriflux data. Remote Sens Environ 114:1924–1939

Ma SY, Baldocchi DD, Xu LK, Hehn T (2007) Inter-annual variability in carbon dioxide exchange of an oak/grass savanna and open grassland in California. Agric For Meteorol 147:157–171

Mu QZ, Zhao MS, Zhang SW (2011) Improvements to a MODIS global terrestrial evapotranspiration algorithm. Remote Sens Environ 115:1782–1800

Noormets A, Gavazzi MJ, McNulty SG, Domec J, Sun G, King JS, Chen J (2010) Response of carbon fluxes to drought in a coastal plain loblolly pine forests. Glob Change Biol 16:272–287

Norman JM, Kustas WP, Humes KS (1995) A two-source approach for estimating soil and vegetation energy fluxes in observations of directional radiometric surface-temperature. Agric For Meteorol 77:263–293

Peng Y, Gitelson AA, Sakamoto T (2013) Remote sensing of gross primary productivity in crops using MODIS 250 m data. Remote Sens Environ 128:186–196

Paw UKT, Falk M, Suchanek TH, Ustin SL, Chen J, Park YS, Winner W, Sean T, Theodore H, Roger S, Thomas K, Pyles R, Schroeder M, Mastista A (2004) Carbon dioxide exchange between an old-growth forest and the atmosphere. Ecosystems 7:513–524

Rahman AF, Sims DA, Cordova VD, El-Masri BZ (2005) Potential of MODIS EVI and surface temperature for directly estimating per-pixel ecosystem C fluxes. Geophys Res Lett 32:L19404

Ryu Y et al (2012) On the temporal upscaling of evapotranspiration from instantaneous remote sensing measurements to 8-day mean daily-sums. Agric For Meteorol 152:212–222

Schaap MG, Leij FJ, van Genuchten MT (1998) Neural network analysis for hierarchical prediction of soil hydraulic properties. Soil Sci Soc Am J 62:847–855

Sims DA et al (2006) On the use of MODIS EVI to assess gross primary productivity of North American ecosystems. J Geophys Res 111:G04015

Sims DA et al (2008) A new model of gross primary productivity for North American ecosystems based solely on the enhanced vegetation index and land surface temperature from MODIS. Remote Sens Environ 112:1633–1646

Su Z (2002) The surface energy balance system (SEBS) for estimation of turbulent heat fluxes. Hydrol Earth Syst Sci 6:85–99

Urbanski S et al (2007) Factors controlling CO_2 exchange on timescales from hourly to decadal at Harvard forest. J Geophys Res 112:G02020

Van Genuchten MT (1980) A closed-form equation for predicting the hydraulic conductivity of unsaturated soils. Soil Sci Soc Am J 44:892–898

Wu C, Chen JM, Huang N (2011) Predicting gross primary production from the enhanced vegetation index and photosynthetically active radiation: evaluation and calibration. Remote Sens Environ 115:3424–3435

Yang YT, Shang SH (2013) A hybrid dual source scheme and trapezoid framework based evapotranspiration model (HTEM) using satellite images: algorithm and model test. J Geophys Res 118:2284–2300

Yang YT, Shang SH, Jiang L (2012) Remote sensing temporal and spatial patterns of evapotranspiration and the response to water management in a large irrigation district of North China. Agric For Meteorol 164:112–122

Yang YT, Long D, Shang S (2013) Remote estimation of terrestrial evapotranspiration without using meteorological data. Geophys Res Lett 40:3026–3030

Zhang J et al (2009) Satellite-based estimation of evapotranspiration of an old-growth temperate mixed forest. Agric For Meteorol 149:976–984

Chapter 8
Conclusions, Limitations and Recommendation for Future Research

8.1 Conclusions

Land surface evapotranspiration (ET) is one of the most active factors with the terrestrial hydrological cycle, which also provides an important lower boundary condition for understanding the climate system. Focused on vegetated surfaces, particularly partially and non-uniformly vegetated surfaces, this dissertation comprehensively compared and evaluated different ET models (i.e., the P-M model, two-layer model, two-patch model and the hybrid model) in estimating potential ET and actual ET (Chaps. 2 and 3). With this, a hybrid dual source scheme-based soil-vegetation-atmosphere continuum model was developed in Chap. 4. In order to obtain ET information at the regional scale, a hybrid dual source scheme and vegetation index-land surface temperature trapezoidal framework based remote sensing ET model (i.e., HTEM) was proposed in Chap. 5. This model was then applied in a larger irrigation district of North China to assess the impact of water-saving rehabilitation project on local water resources in Chap. 6. Furthermore, to circumvent difficulties in detail description of water and heat transfer over surfaces with complex vegetation cover and to avoid uncertainties associated with meteorological inputs at large scales, a new theory of ET estimation by exploiting the linkage between water and carbon cycles was proposed in Chap. 7. Conclusions and main findings of each chapter are given below.

Chapter 2 provides a detailed comparison of the performances among three dual source ET models, including the S–W model, the T-P model and the TVET model, in estimating and partitioning potential evaporation and potential transpiration under different hypothetical vegetation distribution conditions. Results showed that both the patch and hybrid model performed reasonably well in estimating potential ET under homogeneous vegetation distribution conditions. However, the S–W model tended to overestimate potential ET, as it generally gave higher potential evaporation estimates. The overestimation in potential ET by the S–W model was increased with the increase of F_c and the decrease of LAI. In contrast, the T-P

Y. Yang, *Evapotranspiration Over Heterogeneous Vegetated Surfaces*,
Springer Theses, DOI 10.1007/978-3-662-46173-0_8

model had a tendency to underestimate potential evaporation, especially with high F_c and low LAI. For heterogeneous vegetation distribution conditions, potential ET estimated from the S–W model was generally higher than that given by the T-P and TVET model, particularly with low F_c. Potential evaporation (potential transpiration) from the S–W model increases (decreases) with the increase of LAI. However, both variables from the S–W model did not change with changes of F_c. In contrast, potential transpiration estimated from the T-P and TVET model was increased with the increase of both LAI and *F*c. Potential evaporation from the T-P model was increased with the increase of F_c, but kept relative constant under various LAI conditions, while potential evaporation from the TVET model was increased with the decrease of both F_c and LAI. The above results suggest that the S–W model may give reasonable potential transpiration estimates over homogeneous vegetated surfaces, while the T-P model is more suitable for surfaces with lower fractional and clumped vegetation cover. By contrast, the TVET model performs better than both the S–W model and the T-P model, which can be used to estimate potential evaporation and potential transpiration partitioning for a wide range of surfaces with different vegetation distribution patterns.

Chapter 3 develops a hybrid dual source model (i.e., the H-D model) and applied it in four different ecosystems to estimate actual ET processes. Outputs of the H-D model were tested against eddy covariance measurements and compared with three other ET models. The results indicate that (1) the H-D model could generate accurate ET estimates in different ecosystems, with mean absolute errors ranging from 16.3 to 38.6 W/m^2, modified coefficient of efficiency ranging from 0.56 to 0.79, and modified index of agreement ranging from 0.48 to 0.87; (2) the H-D model generally gives better ET estimates and E and T partitioning than the three other models, suggesting that the H-D model appear to be more suited for ET estimation over surfaces with different vegetation patterns; (3) the P-M model significantly underestimates ET in the savannas ecosystem, but generally performs well in other three ecosystems; (4) the S–W model tends to overestimate plant transpiration when LAI is low, and the T-P model tends to overestimate plant transpiration under low LAI but high *F*r conditions.

Chapter 4 develops a unidirectional soil-plant-atmosphere continuum model (i.e., HDS-SPAC) by coupling the hybrid dual source scheme and a soil water/heat dynamic model. The developed model was applied in an agricultural ecosystem and a natural forest ecosystem, respectively. In addition, this chapter presents a new experimental method for direct water stress function testing and parameterization. The results show that (1) the HDS-SPAC model is able to correctly simulate soil moisture/temperature profiles and ET, and capture effects of surface vegetation characteristics on quantifying actual evaporation and transpiration; (2) the designed experimental method is capable in examining and parameterizing water stress functions, and the S-shape function is better than the Feddes function to fit for the data of drooping sheoak; (3) the root water uptake water stress function is not only dependent of the soil moisture condition, but also of the atmospheric demand. After incorporating atmospheric demand into the S-shape water stress function, the performance of the HDS-SPAC model is improved.

Chapter 5 proposes a new remote sensing evapotranspiration model (HTEM) based on the hybrid dual-source scheme and the theoretical trapezoid framework. Soil wetness isolines within a theoretically determined trapezoid F_r/LST space are used in HTEM to decompose bulk radiative surface temperature into canopy temperature and soil temperature. Performance of the HTEM was tested at both the humid SMACEX site in Iowa with Landsat TM/ETM+ data and the sub-humid Weishan site in North China Plain with MODIS Terra data. Results showed that energy fluxes from HTEM agree well with tower based measurements, and are generally better than other remote sensing evapotranspiration models applied with the same data sets. Additionally, the HTEM could provide reasonable partitioning between evaporation and transpiration. Sensitivity analysis suggests that the HTEM is mostly sensitive to temperature variables, and less sensitive to other meteorological observations and the hypothetic vegetation parameters.

Chapter 6 maps the growing season ET from 2000 to 2010 in Hetao Irrigation District was mapped using the HTEM model fed with MODIS data. The performance of HTEM model was tested with in situ measurement at field scale and water balance modeling at regional scale, respectively. Results show that (1) the HTEM model can be well applied in Hetao area, with the RMSE of 0.6 mm day^{-1} at field scale on 5–7 days basis and 21.9 mm at regional scale on annual basis; (2) the annual agricultural land ET ranged from 578 to 634 mm, which accounts for about 62 % of total ET in the region. Both the interannual variability in annual ET and the seasonal variability in monthly ET can be primarily explained by the variations of reference ET; (3) the interannual variabilities in ET over water body, irrigated grassland, marsh land and woodland were strongly correlated with the variations of reference ET, while those over sandy land and Gobi desert mainly depended on the variation of annual precipitation; (4) Agricultural land ET did not decrease with the reduction in total water diversion from the Yellow River following the progress of irrigation district rehabilitation project. On the contrary, non-irrigate grassland was found to be the largest contribution of water-saving due to groundwater level falling. These results indicate a positive effect of the rehabilitation project, and would be helpful in future water management for the area. Besides this positive effect, however, caution has to be paid that the continuous decrease of water supply would result in the drop of groundwater level and consequently the degradation of non-irrigated grassland, which may further cause other ecological issues.

Chapter 7 proposes a method to estimate terrestrial ecosystem ET from remote sensing by exploiting the linkage between water and carbon cycles. The major strength of this method is that it does not require meteorological input as used by other satellite-based ET models. This method is easy to apply, requiring only routinely available EVI and LST data at longer timescales (e.g., 16 days in MODIS products) to calculate GPP, as well as remotely sensed leaf area index and regional soil texture dataset to estimate WUE. ET estimates from the proposed method compares reasonably well with flux-tower measurements at all validation sites. Comparison with the MOD16 ET product shows that the developed method generally outperforms the MOD16 ET algorithm.

8.2 Limitations of Current Research and Recommendations for Future Research

With the experience and insight gained from the studies, the following perspectives are considered as limitations of the current study and recommended for future research:

(1) Further validation of the hybrid dual source approach. Model comparison in Chap. 2 was conducted in a relatively dry climate, and that in Chap. 3 was limited in four types of ecosystem at the point level. Further efforts are needed to test the applicability of the hybrid dual source approach over areas across a wider range of climate types and vegetation types.

(2) Effect of terrain on ET processes. Despite vegetation, terrain factors, such as slope size and direction, would also exert non-negligible impacts on ET processes by directly controlling radiation transfer. Diverse in surface radiation loading results in variations in water and heat conditions, leading to heterogeneity in vegetation distribution. As a result, considering the terrain effect on ET processes deserves more attentions as we continuous on ET modelling.

(3) Further complement of the HDS-SPAC model. SPAC model contains detailed descriptions of water and heat (also carbon) transfer within the SPAC system. In comparison to previous SPAC models, the HDS-SPAC model focuses on the improvements of above-surface water/heat transfer and sub-surface root water uptake. However, for other sub-processes, such as radiation transfer within the canopy and rainfall interception, HDS-SPAC adopts relatively simple methods to describe them. Furthermore, surface runoff and groundwater recharge, which represent another two critical hydrological components, are ignored in HDS-SPAC. Further improvement on the HDS-SPAC model requires a more comprehensive and detail description on different sub-processes within the SPAC system.

(4) Improvement on the HTEM model. Air temperature is taken to be the lower boundary of the trapezoid space in HTEM. However, such treatment does not allow considering the effect of advection by the model. For desert oasis and period short after rainfall or irrigation, the land surface often experiences a strong horizontal energy movement. Thus, deriving a more realistic cold edge of the trapezoid space is one of the key focuses in the improvement of the HTEM model, especially for model application in relatively dry environments.

(5) Further exploring new methods for ET estimation over vegetated surfaces. In this dissertation, we discussed the potential of ET estimation without using meteorological data by exploiting the relationship between water and carbon cycles. However, theoretically, GPP resulted from green vegetation photosynthesis is only related to vegetation transpiration (T). The non-biological

water consumption component, soil evaporation (E), does not contribute to photosynthesis. This raises a more important question: whether the relationship between GPP and T can be more stable than that between GPP and ET? A more stable relationship between carbon and water cycles would greatly benefits our understanding of the coupled water and carbon cycle and improves our ability to quantify them.